



Centro Brasileiro de Pesquisas Físicas

Coordenação de Educação
Coordenação de Física Teórica

Guilherme Vieira de Abreu e Silva

Mesoscopic current fluctuations in superconductor-topological insulator Josephson junctions

Rio de Janeiro - RJ

January 15, 2024

Guilherme Vieira de Abreu e Silva

**Mesoscopic current fluctuations in
superconductor-topological insulator Josephson
junctions**

Tese apresentada ao curso de Pós-Graduação em Física do Centro Brasileiro de Pesquisas Físicas, como requisito para a obtenção do título de Doutor em Física.

Orientador:

Tobias Micklitz

January 15, 2024

"MESOSCOPIC CURRENT FLUCTUATIONS IN
SUPERCONDUCTOR-TOPOLOGICAL INSULATOR JOSEPHSON
JUNCTIONS"

GUILHERME VIEIRA DE ABREU E SILVA

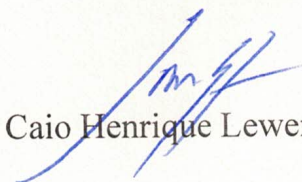
Tese de Doutorado em Física apresentada no
Centro Brasileiro de Pesquisas Físicas do
Ministério da Ciência Tecnologia e Inovação.
Fazendo parte da banca examinadora os seguintes
professores:



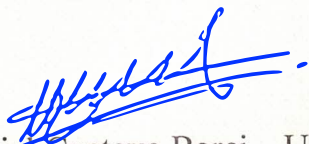
Tobias Micklitz - Orientador/CBPF



Thereza Cristina de Lacerda Paiva – UFRJ



Caio Henrique Lewenkopf – UFF



Daniel Gustavo Barci – UERJ



Leandro Romão Fernandes Lima – UFRRJ

Rio de Janeiro, 06 de dezembro de 2023.

Agradecimentos

Agradeço inicialmente aos meus familiares, primeiramente aos meus pais, Angelica e Luiz, meus primeiros e principais apoiadores na carreira. Que investiram o máximo possível na minha educação, mesmo quando não podiam. E seguem até hoje sendo minha grande base de apoio para chegar mais longe. O esforço deles, e de seus pais, garantiram hoje eu estar à beira do máximo título acadêmico. Agradeço também à minha irmã, Luiza, e demais familiares pelo apoio em diversas frentes, incluindo o apoio financeiro dado por meus avós em diversos momentos, desde a escola até minha primeira ida ao exterior durante o doutorado.

Agradeço em especial à Clarissa Neutzling, minha namorada, que tornou possível eu reencontrar beleza no trabalho e carreira que seguimos. A quem me ajuda a ter direção, clareza e calma para superar as frustrações em tempos tão complicados. Assim como também ter esperança em superar desafios na vida que planejamos construir juntos. Espero estar à altura em reciprocidade de todo o apoio que recebo. Te amo.

Agradeço à toda a comunidade do CBPF ao longo de todos esses anos como aluno, em diversas etapas. Ao meu orientador Tobias Micklitz por toda a experiência profissional repassada e a confiança em me dar a liberdade de explorar ideias e mudanças. Agradeço à Marcus Marinho pelo trabalho em conjunto que tivemos, assim como todos os outros alunos do nosso grupo. À Sônia Ferreira e Denise Coutinho por terem sido minhas grandes apoiadoras na carreira didática, com as oportunidades trazidas pelo Físico por uma tarde, Semana Nacional de Ciência e Tecnologia, Reunião Anual da SBPC. Além dos apoios dos professores responsáveis, Roberto Sarthour, Flávio Garcia e André Massafferri, adicionando ainda as experiências com o Físico para todos e PROFCEM. Esses trabalhos me fizeram um profissional mais completo, preocupado não apenas em trabalhar com a física mas divulgar ela e o CBPF, instituição que muito me identifico. Agradecimento adicional à ótima experiência proporcionada pela EAFExp, que me expandiu os olhos para a física experimental e ao Python Summer Camp, que me introduziu ao trabalho computacional na física. Por fim agradeço ao professor Georg Schwiete pelo tempo em trabalho conjunto na Universidade do Alabama e neste trabalho.

Agradeço ainda a todas as pessoas que diretamente estiveram relacionadas comigo na vida, sejam os amigos do Kung Fu, sejam os do Voluntariado do PARNIT, demais funcionários do CBPF em seu grande apoio na minha estada.

Por fim agradeço à CAPES por financiar meu doutorado, assim como pela Universidade do Alabama pelo meu tempo de estada mantido por ela. Por fim, agradecimentos ao CBPF pela infraestrutura utilizada durante todo esse processo de formação.

*“Nothing is too wonderful to be true, if
it be consistent with the laws of
nature.”*

Michael Faraday

Contents

Resumo	xi
Abstract	xiii
1 Introduction	1
2 Superconductivity and Josephson Effect	8
2.1 Superconductivity Principles	8
2.2 Andreev Reflection	13
2.3 Josephson Junctions	14
2.4 From BCS to BdG	17
3 Topological Insulators	19
4 STIS Junction	26
4.1 Building an Action	28
4.2 Replica Trick and Sample space	30
4.3 Disorder Average	32
4.4 Saddle Point Equation	34
4.5 Gradient Expansion	36
4.6 Usadel Equation	37
4.7 Rotation of the Q-field	40
4.8 Density of States	40
4.9 Introducing fluctuations around the saddle point	43
4.9.1 Eigenvalues	46
4.10 Average current and sample-to-sample fluctuations at zero magnetic field	48
4.10.1 Average current	48

Long dwell time: $E_t \ll \Delta$	49
Short dwell time: $E_t \gg \Delta$	49
Arbitrary dwell time	50
4.10.2 Sample-to-sample fluctuations	50
Long dwell time: $E_t \ll \Delta$	52
Short dwell time: $E_t \gg \Delta$	54
Arbitrary dwell time	55
4.11 Average current and sample-to-sample fluctuations at finite magnetic field .	56
4.11.1 Average current	57
4.11.2 Sample-to-sample fluctuations	59
Quantum dot limit: $E_{\text{Th}}^\perp \gg E_t$	60
Quasi-one-dimensional limit: $E_{\text{Th}}^\perp \ll E_t$	62
5 Summary	64
6 Perspectives	66
A Gradient Expansion	78
A.1 First order term	78
A.2 Second order term	79
B Quantum Hall Effect Code	82

List of Figures

- 1.1 The image shows two wires with length L . The wire can be decomposed in N regions, here represented in blue, that are coherent along the wire, with coherence length $l_{\phi_i} < L$. The observables, like resistance, in each region has a characteristic fluctuation pattern. The total resistance is the sum of the resistances of the regions. The fluctuation patterns average out and the resistance becomes self-averaging. When the coherence length grows, these coherent areas "merge" becoming larger and larger, until $l_{\phi} > L$. Then all the system is in phase. Fluctuations now have macroscopic implications. Note also that the temperature reduces the coherence length, $l_{\phi_1} < l_{\phi_2}$ as T grows. 2
- 1.2 UCF on stadium geometry used for dynamical billiard study [12]. There are two metal leads at the bottom (left image), where a electrical current enters in one lead, enters the stadium and leaves in another. The geometry makes it a non integrable system, leaving to relevant fluctuations on conductance, similar to a disordered system. Images generated from Kwant package, with code in reference [13]. 4
- 1.3 The image illustrates the Kitaev chain. The top image represents a $1D$ wire, where each "domino" is an electron. Each electron has two dots, these are Majoranas, ten in total. The middle chain shows the paired Majoranas represented by the red shade. The bottom one represents another possibility of rearrangement, where we have paired Majoranas, but from different electrons. This state is tuned by external parameters and creates at the edges two non-local Majoranas, represented in blue. The parameters responsible for the tuning are the chemical potential, μ , the superconducting pairing Δ and the hopping parameter for the majoranas τ 5

1.4	Model of a STIS junction. The green component is a TI thin film. Yellow represent the two superconductors. In blue we have a the tunnelling interface, for computational reasons. The red part is a lead that connects to external electrical current. This is a model developed using Kwant [13] to perform simulations of Josephson currents on STIS.	6
2.1	The resistivity of three different superconductors measured at the Escola Avançada de Física Experimental (EAFExp) in 2019. It is clear that below a certain critical temperature, the resistivity drops to zero. Two of the superconductors, <i>Pb</i> and <i>V₃Si</i> , are Type I superconductors, which means that there is an instant drop in resistivity as the temperature decreases. The third superconductor, <i>YBa₂Cu₃O_{6.38}</i> , is a Type II superconductor. It exhibits a decrease in resistivity at 89K before dropping to zero at another critical temperature, which is the temperature at which it enters a mixed state, where magnetic field vortices are present. In a mixed state, some parts of the material remain in a superconducting state, while others do not [23].	9
2.2	The magnetization of three different superconductors was measured at the Escola Avançada de Física Experimental (EAFExp) in 2019 using a Quantum Design PPMS Dynacool. The results show that below the critical temperature of each superconductor, the material becomes magnetized in response to an applied external magnetic field. Additionally, it can be observed that there is a critical field at which the Meissner effect is broken. The Meissner effect is a phenomenon in which a superconductor exhibits diamagnetic behavior in response to an external magnetic field. This is due to surface superconducting currents that create an opposing magnetic field that cancels out the applied magnetic field, shielding the bulk of the material. However, if the applied magnetic field is too strong, superconductivity is destroyed, this the surface currents are disrupted and the Meissner effect is broken [24]. The measurement for <i>YBa₂Cu₃O_{6.38}</i> varies temperature for given magnetic fields. The 2K measurement behaves differently for <i>V₃Si</i> due to defects in the sample [25].	10

2.3	An incoming electron and its reflected hole giving rise to a Cooper pair entering the condensate after Andreev reflection. Image Credits [33].	14
2.4	The image displays various weak link configurations, with gray representing superconductors and red representing other materials such as insulators or metals. From left to right and top to bottom, we see a sandwich junction, which is later identified as a Josephson junction; a top view of a Dayem bridge with a shorter funnel on the coherence length scale [35]; a superposition of films, where the supercurrent is affected by the cover; a longitudinal cross-section of a junction with variable thickness; and a grain-boundary junction, which is also a Dayem bridge, with the superconductor connected to a different material. Today, there are an infinite number of nano configurations for weak links. A good example of their practical use is the Superconducting Quantum Interference Device (SQUID). A review by Likharev [36] covers several configurations.	15

3.1	<p>QHE: Here u stands for unity of magnetic field, since the code is not using realistic parameters to perform calculations. A top view of a 2D conducting surface, Figure (a), reveals an interesting phenomenon when a magnetic field is applied perpendicular to the current flow. In this scenario, the current concentrates along the edges of the surface leaving the bulk as an insulator. This occurrence can be attributed to the influence of the magnetic field, which exerts a Lorentz force on the electrons, causing them to follow circular orbits. As a result, a continuous current flow is not generated; instead, near the edges, the circular electron orbits can reflect and lead to skipping orbits. Consequently, current is observed along the edges of the surface. These localized states as known as Landau levels. Although the current keeps concentrating at the edge, for some values of magnetic flux, the current is spread again due to presence of disorder, as illustrated in Figure (b). As the magnetic field strength increases the electron orbits become smaller and more localized, due to the increasing spacing of Landau levels, Figure (c). In the absence of disorder, the quantized steps corresponding to Landau levels are well-defined. The presence of disorder introduces scattering, which adds some noise to the states, although the levels keep well defined, with perfectly quantized Hall plateaus, Figure (d). Graphics generated with an adapted model in Kwant [13], the code is available in Appendix B.</p>	22
3.2	<p>a) Kitaev model, a chain of electrons, where each electron accommodates two Majorana modes that can interact to each other. This interaction occurs between Majoranas belonging to the same electron and Majoranas belonging to adjacent electrons, as depicted in the second and third lines. In these examples, the red bars represent the bidings. b) Band structure showing the persistence of edge zero modes of Majorana fermions.</p>	24

4.1	A model of the STIS junction, already illustrated in the Introduction. The green component is a TI thin film. Yellow bases represent the two superconductors. In blue we have a tunnelling interface, for computational reasons. The red part is a lead that connects to external electrical current. For our system, each color part addresses a Hamiltonian sector in (4.1). Integrating over the superconductor degrees of freedom we derive an effective theory for the TI-surface that accounts for the coupling to the superconductors. This figure is the plot of a model developed using Kwant [13], to perform simulations of Josephson currents on STIS.	27
4.2	(a) Density of states $\nu(\epsilon)$ for the vanishing magnetic field normalized to the density of states $\nu = \nu(\mu)$ in the absence of superconducting leads for different values of $e_t = E_t/\Delta = 0.1, 1, 10$. Panels (b) and (c) show density of states of the microbridge at a finite magnetic field as a function of frequency ϵ for different values of $\gamma = E_t/E_\Phi = (0.1/0.01, 0.1/0.1, 0.1/0.25)$ and fixed phase $\phi = 0$, where $e_\Phi = E_\Phi/\Delta$	41
4.3	The average current $I(\phi)$ at zero magnetic field as a function of the dwell energy $e_t = E_t/\Delta$ for various values of $t = T/\Delta$ and $\phi = \pi/2$ on the left hand side, and as a function of ϕ for various t and $e_t = 0.01$, on the right hand side.	50
4.4	On the right hand side, the variance of the Josephson current as a function of the phase difference ϕ in the quantum dot geometry. Solid lines represent the zero temperature limit, whereas dashed lines denote the finite temperature limit. On the left hand side, we display \mathcal{K}_0 as a function of $e_t = E_t/\Delta$ for various fixed phases, $\phi = \pi/6, \pi/3, \phi/2, 2\pi/3$	52
4.5	On the right hand side, the variance of the Josephson current as a function of the phase difference ϕ in the quasi-one-dimensional geometry. On the left hand side, we display \mathcal{K}_1 as a function of $e_t = E_t/\Delta$ for various fixed phases, $\phi = \pi/6, \pi/3, \phi/2, 2\pi/3$	53
4.6	The ratio between the current fluctuations and the average current as a function of e_t in the absence of a magnetic field and at zero temperature. On the left hand side, we show this ratio for the quantum dot geometry, on the right hand side for the quasi-one-dimensional case.	54

4.7	Left panel: J_Φ at zero temperature as a function of ϕ and for various values of $\gamma = E_t/E_\Phi$. Right panel: J_Φ as a function of temperature $t = T/\Delta$ for various values of γ , cf. (4.109). Here the dwell energy is chosen as $e_t = E_t/\Delta = 1/100$ and the phase difference as $\phi = \pi/2$. Bottom panel: The average current at zero temperature for various values of $\gamma = E_t/E_\Phi$, where we fixed $e_t = E_t/\Delta = 1/1000$. The solid lines represent the exact numerical solution and dash-dotted lines the analytical approximation.	57
4.8	Left panel: $\mathcal{K}_{0,\Phi}$ (quantum dot) as a function of phase angle ϕ for various values of $\gamma = E_t/E_\Phi$. Right panel: $\mathcal{K}_{1,\Phi}$ (quasi-one-dimensional geometry) as a function of phase difference ϕ for various values of $\gamma = E_t/E_\Phi$. The dashed lines indicate the parameter region for which the semiclassical approximation becomes uncontrolled. In all figures we fixed $e_t = E_t/\Delta = 1/100$ and varied E_Φ	59
4.9	Current fluctuations in the strong magnetic field limit as a function of phase for various values $\gamma = E_t/E_\Phi$ (we here fixed $e_t = E_t/\Delta = 1/1000$ and varied E_Φ). Solid lines and markers denote the analytical result employing the approximate solution of the mean field equation and the result building on the numerical solution of the mean field equation, respectively. Left panel: quantum dot geometry. Right panel: quasi-one-dimensional geometry.	62
4.10	Relative size of current fluctuations $\sqrt{\text{var}I_\Phi}/I_\Phi$ in the strong magnetic field limit as a function of $\gamma = E_t/E_\Phi$ and various values of ϕ . Left panel: quantum dot geometry. Right panel: quasi-one-dimensional geometry.	63
6.1	An image extracted from [89] illustrates the recognition process. The neural network is supplied with UCF data, generated using Kwant [13], for a metal connected to leads and exposed to an orthogonal magnetic field to the current propagation. Additionally, an image depicting the density of states of this metal, including randomly inserted defects in the lattice, is also provided as input. Utilizing a convolutional neural network, the study managed to reproduce defect information on density of states as output solely from UCF data. This advancement introduces the potential of a novel tool for exploring material structures, akin to how diffraction techniques have been employed over the past decades.	67

6.2 An image extracted from [91] serves as an example of how a DGCNN can gain comprehension using probes (in red) to discern the body, turbines, and wings of a airplane in a 3D point cloud context. The process involves assessing the distance between the red dots and all other points within the object. At each stage, the network associate distances semantically between the points, that is, the points belonging to the wing are nearer from each other than any point of the body, or the turbines. As a point in the left turbine is nearer to any point in the right turbine than any point the left wing, which it is attached. In a lattice there are several characteristics that could bring a semantic difference. 69

Resumo

Investigamos flutuações mesoscópicas na supercorrente de uma junção Josephson, que compreende uma microponte isolante topológica posicionada entre dois supercondutores convencionais que induzem um gap no espectro de estados de superfície. Além disso, consideramos um campo magnético que penetra na área de junção, levando ao desemparelhamento e ao preenchimento de gaps. A magnitude e o comportamento funcional das flutuações da corrente Josephson são determinados através de meios analíticos. Do ponto de vista técnico, as flutuações mesoscópicas, sobrepostas à representação do campo médio, são elucidadas através de uma abordagem de teoria de campos. Especificamente, essas flutuações são descritas usando o modelo σ não linear em réplica dentro da classe D da classificação de simetria estendida.

Palavras-chave: Topological Insulator, Superconductivity, Josephson Junction.

Abstract

We investigate mesoscopic fluctuations in the supercurrent of a Josephson junction, which comprises a topological insulator micro-bridge positioned between two conventional superconductors that induce a gap in the spectrum of surface states. Additionally, we account for a magnetic field that penetrates the junction area, leading to depairing and gap filling. The comprehensive magnitude and functional behavior of the Josephson current fluctuations are determined through analytical means. From a technical standpoint, the mesoscopic fluctuations, superimposed on the mean-field representation, are elucidated using a field theory approach. Specifically, these fluctuations are described using a replica nonlinear σ -model within the class-D of the extended symmetry classification.

Keywords: Topological Insulator, Superconductivity, Josephson Junction.

Chapter 1

Introduction

Mesoscopic systems - are ones characterized by the fact that, although such systems contains a large number of degrees of freedom, quantum effects take place and are relevant to statistical calculations [1]. In these systems the dephasing length of quasiparticles – the length scale on which quantum propagation remains phase coherent – is larger than the system size. This implies that electrons, for example, preserve their wave function phase when passing through the entire medium.

In statistical mechanics one usually recovers average ensemble values by taking the thermodynamic limit, that is, taking the system volume and number of particles to infinite, while maintaining its ratio constant. The thermodynamic limit can be understood as the system grows larger than all relevant length scales, specifically larger than the phase coherence length, l_ϕ . Inside a system different regions behave as they are statistically independent of each other. A system of size L can be seen as a collection of various regions, each region with size l_ϕ . Expectation values of a local observable has fluctuations in each region, but in the thermodynamic limit fluctuations of all regions average out and observables are described by their average values. However, in cases where the coherence length is larger than the system size, one may expect that fluctuations above the average values remain important, for there is no cancellation of fluctuations, i.e. observables will not be self-averaging. One can understand that the different regions grows so large that they become one with the system, $l_\phi > L$. Those are mesoscopic systems. A good analogy is to think about the classical experiment of synchronization of metronomes fixed in a moving base. They start with their own phase until they are all phase coherent. At first there is just white noise, but their fixed position makes each metronome (or each

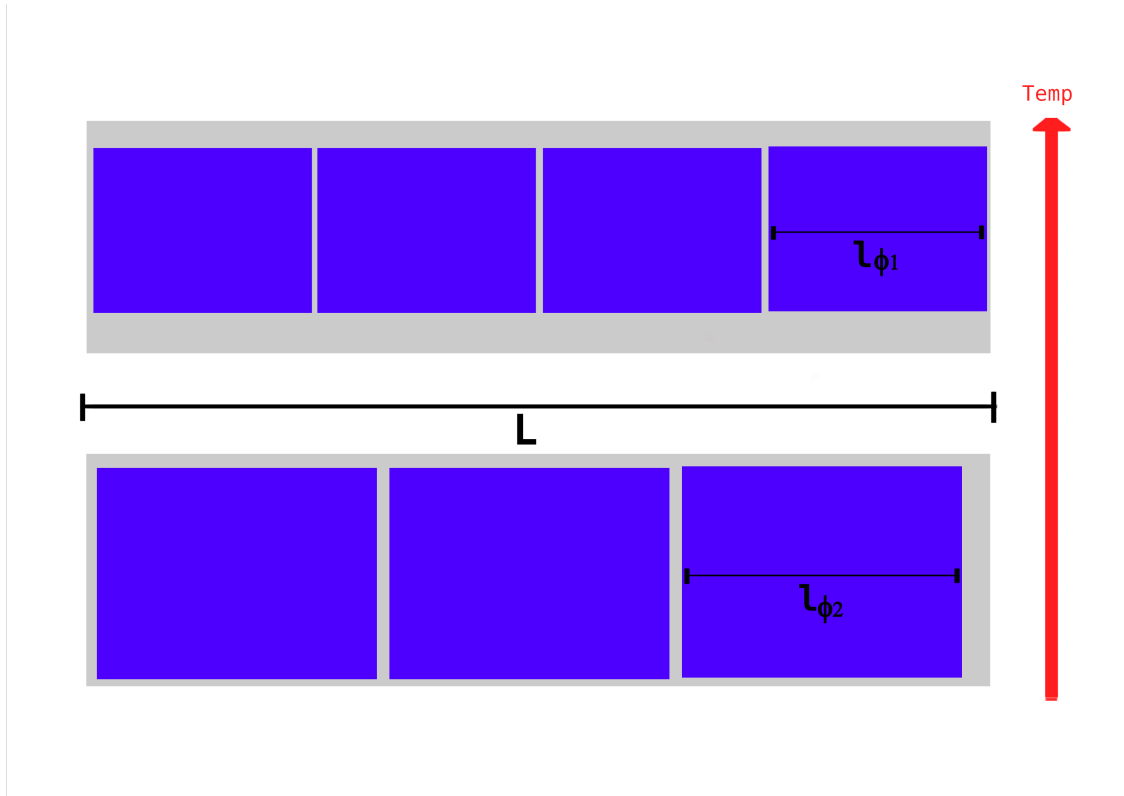


Figure 1.1: The image shows two wires with length L . The wire can be decomposed in N regions, here represented in blue, that are coherent along the wire, with coherence length $l_{\phi_i} < L$. The observables, like resistance, in each region has a characteristic fluctuation pattern. The total resistance is the sum of the resistances of the regions. The fluctuation patterns average out and the resistance becomes self-averaging. When the coherence length grows, these coherent areas "merge" becoming larger and larger, until $l_{\phi} > L$. Then all the system is in phase. Fluctuations now have macroscopic implications. Note also that the temperature reduces the coherence length, $l_{\phi_1} < l_{\phi_2}$ as T grows.

region) to reach the other metronomes (the other regions) at some distance and become phase coherent, and then this distance becomes larger than the whole system, since the table is oscillating. We have also to consider, of course, a temperature dependence for this coherence preservation. Higher temperatures make regions with smaller coherence lengths: The larger the temperature the larger is the phase space for inelastic scattering process, thus l_i , the inelastic scattering length, is smaller and there is more scattering to break coherence, since l_{ϕ} and l_i usually are of the same order. Thus, ideally, for $T \rightarrow 0$ we would have all systems becoming mesoscopic.

Universal Fluctuations - Mesoscopic systems present a variety of unusual quantum phenomena, such as localization and characteristic sample-to-sample fluctuation. A powerful idea is that many of these phenomena can have some universal characteristics, that is, they do not depend on the microscopic details of each sample [2]. One of such univer-

sal phenomena is Universal Conductance Fluctuations, sample-to-sample fluctuations of electric conductance [3, 4, 5, 6, 7, 8]. A small change on an external parameter in a single sample, e.g. magnetic field, has a similar effect on the interference pattern as a change in impurity configuration. It was shown [9, 6] that at low temperatures the variance of conductance is universal, proportional to $(e^2/\hbar)^2$, where that proportionality coefficient depends only on the symmetries and dimensionality of the system. For a wire geometry, for example, the variance is found to be

$$\text{var}G = \frac{2}{15\beta}G_0^2, \quad G_0 = \frac{2e^2}{h}, \quad \beta = 1, 2, 4, \quad (1.1)$$

where the values of parameter β correspond to standard Dyson symmetry classes of the orthogonal (time-reversal and spin rotational symmetry), unitary (no time-reversal symmetry), and symplectic (as in orthogonal but broken spin rotational symmetry) ensembles, respectively [10]. In contrast to the sample average conductance, $\langle G \rangle \sim G_0(Nl/L)$, universality of fluctuations are manifested by the fact that there is no dependence on the disorder mean free path l , the number of transverse modes N , and the system size L provided $l \ll L \ll Nl$ (the second inequality insures that the wire length is shorter than the localization length). As expected from previous considerations, universality is also robust against interaction effects provided that the system size is smaller than the dephasing length, $L < l_\phi(T)$, although interactions determine the typical scale of $l_\phi(T)$ and its temperature dependence [11].

Furthermore, mesoscopic fluctuations can be fingerprints of the material. In a mesoscopic disordered conductor (at low temperatures) the phase of the electron wave functions can be modulated by magnetic fields, causing fluctuations as a function of this external magnetic field. The simplest case is configured by the Aharonov-Bohm oscillations [4, 14, 15, 16], for an electron in a ring, where it can have constructive or destructive interference, depending on the phase multiplicity of π . In mesoscopic conductors such effects are much more complicated because of impurity displacement along the material, thus complicating the magnetic field dependence of the conductance. Its patterns are known to encode information on the material composition, such as impurity positions. Such impurity configuration is unique for each material, or each type of material. Again, the same analogy can be used from the previous metronomes case, where a magnetic field would be someone shaking the table from the outside, the oscillating patterns are unique for each position

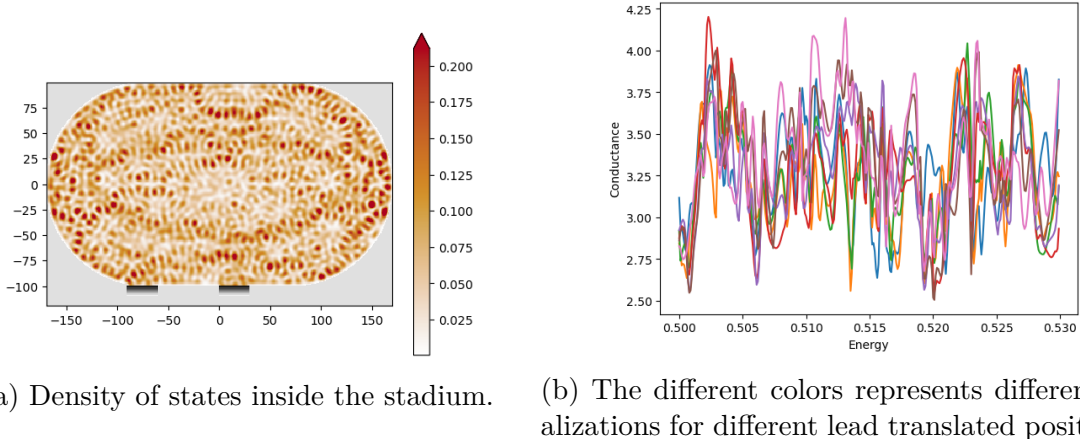


Figure 1.2: UCF on stadium geometry used for dynamical billiard study [12]. There are two metal leads at the bottom (left image), where an electrical current enters in one lead, enters the stadium and leaves in another. The geometry makes it a non-integrable system, leading to relevant fluctuations on conductance, similar to a disordered system. Images generated from Kwant package, with code in reference [13].

configuration of the metronomes in the table, and its phase. This phenomenon is called magneto-fingerprint and is unique for the lattice and its impurity configuration, thus, it gives microscopic details about impurity dependence. The same way the emission spectra of atoms can be used to identify element densities on stars and its previous stages.

Topological Insulators - From the perspective of fundamental physics and applications, topological insulators (TI) are a recent topic of interest. TI are materials with an insulating bulk and a topologically protected metallic surface (3D) or edges (1D, 2D). When put in proximity to the latter, superconductors (SC) can induce superconductivity on these metallic surface (edge) states upon the proximity effect. This feature is hard to produce experimentally, due to the interplay of spin-orbit coupling and induced superconductivity. STIS composite systems have raised a lot of interest, for they can host Majorana fermions, thus, it is a good candidate to perform quantum computation with Majorana fermions as q-bits for quantum processors [18, 19].

Formally, two Majorana fermions γ_1, γ_2 can be defined from an electron as,

$$\begin{aligned}
 c^\dagger &= \frac{1}{2}(\gamma_1 + i\gamma_2), \\
 c &= \frac{1}{2}(\gamma_1 - i\gamma_2), \\
 [\gamma_i, \gamma_j]_+ &= 2\delta_{ij}, \quad \gamma_i = \gamma_i^*,
 \end{aligned} \tag{1.2}$$

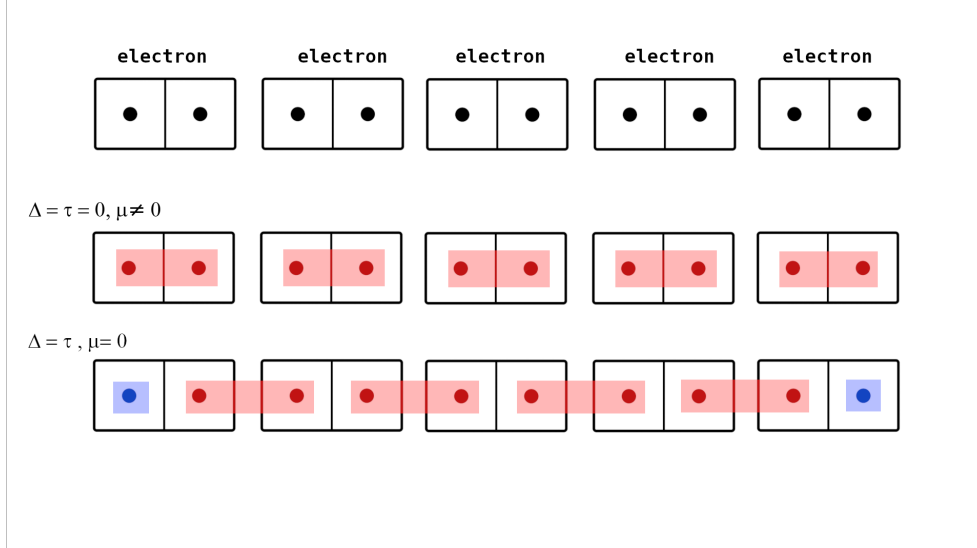


Figure 1.3: The image illustrates the Kitaev chain. The top image represents a $1D$ wire, where each "domino" is an electron. Each electron has two dots, these are Majoranas, ten in total. The middle chain shows the paired Majoranas represented by the red shade. The bottom one represents another possibility of rearrangement, where we have paired Majoranas, but from different electrons. This state is tuned by external parameters and creates at the edges two non-local Majoranas, represented in blue. The parameters responsible for the tuning are the chemical potential, μ , the superconducting pairing Δ and the hopping parameter for the majoranas τ .

where c^\dagger and c are the electron creation and annihilation operators. γ_i are the Majorana modes relative to the electrons that are created and annihilated. Since Majoranas are their own antiparticles, (1.2), they do not conserve charge. Up to now there has been no fundamental particle identified as a Majorana fermion. However, Majorana fermion may emerge as quasiparticles in condensed matter systems. Majorana fermions conserve fermion parity, that is whether the number of fermions is even or odd, and this is the reason a SC is a good medium to host them, where charge is not conserved, only electron parity. The simplest example to illustrate the emergence of Majoranas in a superconductor is the Kitaev chain [17]. An electron chain with p-wave pairing Δ and binding factor τ between electrons, each electron can be expressed in term of two Majorana modes. The Kitaev model tells us that we can manipulate Majoranas in regimes defined by energy parameters (Δ, τ, μ) , as can be seen in Figure 1.3. The Majorana pairing can be changed, such that on each edge of this chain we have an isolated Majorana that could be used to perform quantum computation operations.

In this work we are going to study mesoscopic Josephson Junctions that are composed of two SCs and a TI. The SCs are positioned on top of the metallic surface of the TI,

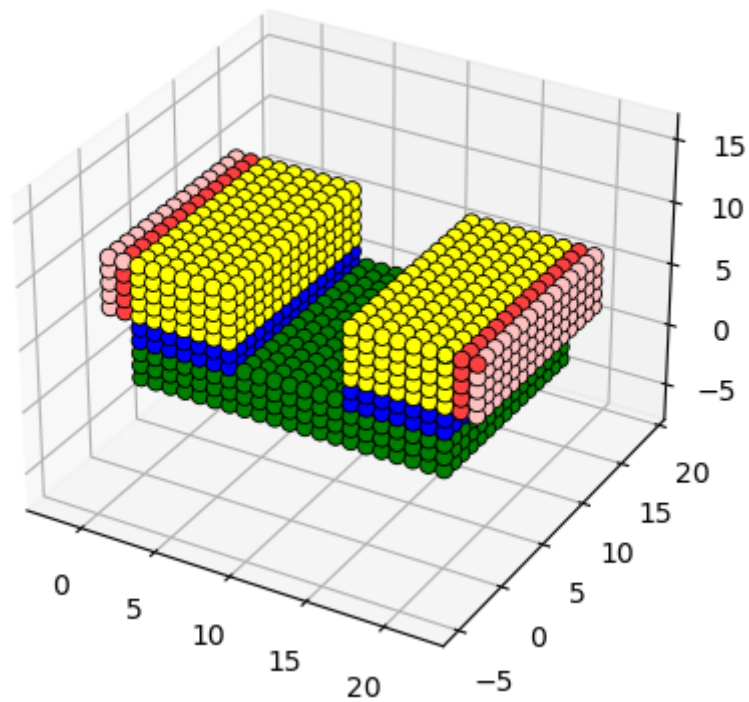


Figure 1.4: Model of a STIS junction. The green component is a TI thin film. Yellow represent the two superconductors. In blue we have a the tunnelling interface, for computational reasons. The red part is a lead that connects to external electrical current. This is a model developed using Kwant [13] to perform simulations of Josephson currents on STIS.

in order to induce superconductivity on it. When submitted to a magnetic flux, which modulates the relative phase of the superconductors, a supercurrent passes through the system. These STIS junctions have been investigated theoretically and experimentally, however we are not aware of a systematic study of mesoscopic fluctuations. This motivates us to study STIS (Superconductor-Topological Insulator-Superconductor) junctions focusing on the sample to sample mesoscopic fluctuations of the Josephson current and its magnetic field dependence, and systematically study the different parameter regimes and geometries. Furthermore, mesoscopic current fluctuations are a good tool to help in the development of these (topological) superconductors. It can give hints of impurity dependence and point out better suited materials to construct such objects with good stability [20].

Chapter 2

Superconductivity and Josephson Effect

We here review the relevant concepts of superconductivity to proceed with further calculations in the STIS junction. We follow a historic and technical approach on what characterizes and creates the superconductivity.

2.1 Superconductivity Principles

Superconductivity is a phenomenon in which a material can transport electrical charge without resistance and is characterized by a transition temperature below which the material exhibits this behavior. Heike Onnes first observed this effect in 1911 at the Leiden Laboratory, following his liquefaction of helium gas at the same laboratory in 1908 [22]. The Meissner effect is another defining characteristic of superconductivity, in which the superconductor expels an external magnetic field due to surface supercurrents [23, 24]. Both features are better illustrated with experimental data in Figures 2.1 and 2.2, respectively.

The first phenomenological explanation for superconductivity came with the London equations [26], at that time called "supraconductors":

$$\frac{\partial \mathbf{j}_s}{\partial t} = \frac{n_s e^2}{m} (\mathbf{E} + \nabla \phi), \quad (2.1)$$

$$\nabla \times \mathbf{j}_s = -\frac{n_s e^2}{m} \mathbf{B}. \quad (2.2)$$

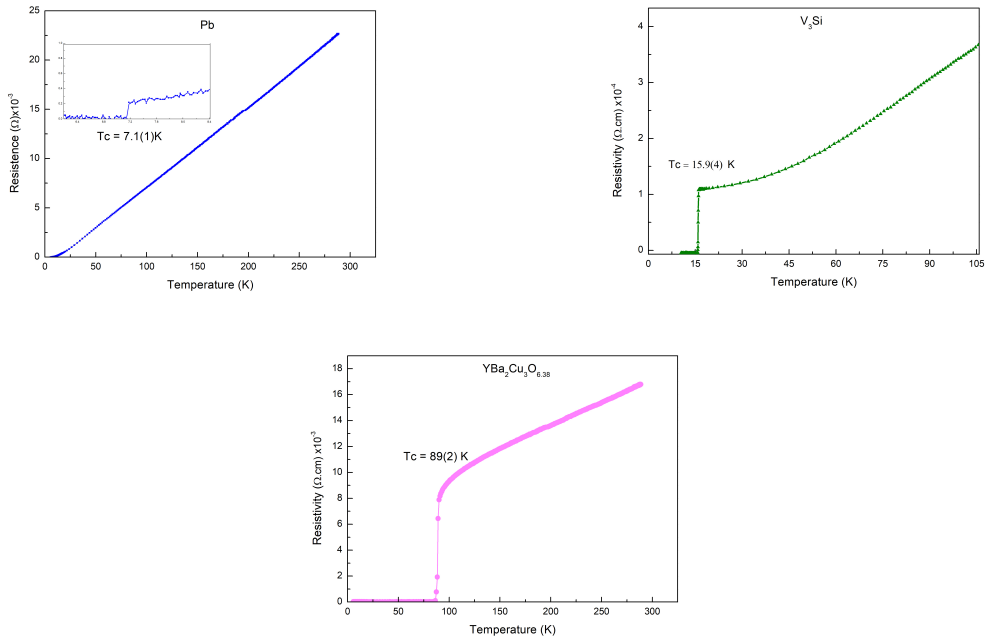


Figure 2.1: The resistivity of three different superconductors measured at the Escola Avançada de Física Experimental (EAFExp) in 2019. It is clear that below a certain critical temperature, the resistivity drops to zero. Two of the superconductors, Pb and V_3Si , are Type I superconductors, which means that there is an instant drop in resistivity as the temperature decreases. The third superconductor, $YBa_2Cu_3O_{6.38}$, is a Type II superconductor. It exhibits a decrease in resistivity at $89K$ before dropping to zero at another critical temperature, which is the temperature at which it enters a mixed state, where magnetic field vortices are present. In a mixed state, some parts of the material remain in a superconducting state, while others do not [23].

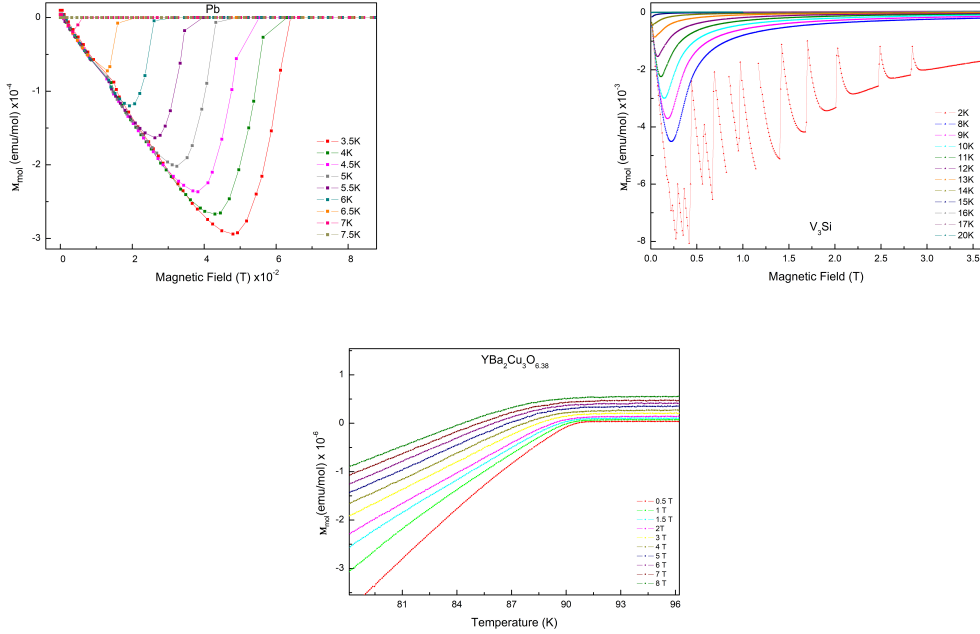


Figure 2.2: The magnetization of three different superconductors was measured at the Escola Avançada de Física Experimental (EAFExp) in 2019 using a Quantum Design PPMS Dynacool. The results show that below the critical temperature of each superconductor, the material becomes magnetized in response to an applied external magnetic field. Additionally, it can be observed that there is a critical field at which the Meissner effect is broken. The Meissner effect is a phenomenon in which a superconductor exhibits diamagnetic behavior in response to an external magnetic field. This is due to surface superconducting currents that create an opposing magnetic field that cancels out the applied magnetic field, shielding the bulk of the material. However, if the applied magnetic field is too strong, superconductivity is destroyed, this the surface currents are disrupted and the Meissner effect is broken [24]. The measurement for $YBa_2Cu_3O_{6.38}$ varies temperature for given magnetic fields. The 2K measurement behaves differently for V_3Si due to defects in the sample [25].

Material	Al	Cd	Hg	In	Nb	Pb	Sn	Ti	$YBa_2Cu_3O_7$
$\lambda(0)/A_0$	500	1300	380-450	640	470	390	510	920	1700

A set of equations for the charge carrier for the supercurrent density \mathbf{j}_s and the number density of supercurrent carries, at the time thought to be electrons. The symbols e and m denote the electric charge and mass, respectively, which were initially believed to correspond to the electron's charge and mass. The density number of the carriers is represented by n_s . The first equation relates to the supercurrent, given a particular external electric field \mathbf{E} in the leads that generates current through the SC and electric potential ϕ , while the second equation describes the Meissner effect in response to a magnetic field \mathbf{B} . The second London equation can be solved to determine the magnetic field within a superconductor for an applied magnetic field B_0 . Specifically, it shows that the field inside the superconductor follows an exponential decay law, $B = B_0 e^{-x/\lambda}$, where λ is the magnetic penetration depth and x the distance from the sample surface. This depth defines the length scale over which an applied magnetic field can penetrate a superconductor. It varies according to material characteristics as can be seen from the table above [27].

The next successful phenomenological theory to describe superconductors was the one known as Ginzburg-Landau [28], which considers quantum mechanics effects on the formation of the superconducting state. The theory is based on Landau's theory of phase transition, which suggests that superconductivity can be viewed as a second-order phase transition. A transition of this nature is characterized by a gradual change in the state of an object, while its symmetry changes discontinuously at a specific temperature. In the ferromagnetic transition all the magnetic momenta becomes oriented, while in superconducting transition there is a change in resistivity, from finite to zero. This theory is characterized by an order parameter, which is used to expand the free energy in a polynomial

$$F = F_n + \alpha|\psi|^2 + \beta|\psi|^4, \quad (2.3)$$

with F_n the free energy in the normal state and α and β phenomenological parameters. In the case of superconductors, the order parameter is represented by the wave function of the superconducting electrons. This assumption may seem counterintuitive, as the wave function ψ is an unobservable variable. However, this suggests that the wave function is

an emergent phenomenon resulting from the coherence of all the particles. The work of Ginzburg and Landau was recognized with the 2003 Nobel Prize in Physics [29].

To include coupling of the order parameter to electromagnetic fields we start from the Gibbs free energy

$$G = G_n + \int \left[\alpha |\psi|^2 + \beta |\psi|^4 + \frac{1}{4m} \left| -i\hbar \nabla \psi - \frac{2e}{c} \mathbf{A} \psi \right|^2 + \frac{(\nabla \times \mathbf{A})^2}{8\pi} - \frac{(\nabla \times \mathbf{A}) B_0}{4\pi} \right], \quad (2.4)$$

where G_n is the free energy of the normal state of the SC, B_0 is an external magnetic field, respectively, and the squared module term is the kinetic energy. Solving the variational problems $\delta_{\psi^*} G = 0$ and $\delta_{\mathbf{A}} G = 0$ it is possible to obtain the following equations:

$$\xi^2 \left(i\nabla + \frac{2\pi}{\phi_0} \mathbf{A} \right)^2 \psi - \psi + \psi |\psi|^2 = 0, \quad (2.5)$$

$$\nabla \times \nabla \times \mathbf{A} = \frac{|\psi|^2}{\lambda^2} \left(\frac{\phi_0}{2\pi} \nabla \theta - \mathbf{A} \right), \quad \phi_0 = \frac{\pi \hbar c}{e}. \quad (2.6)$$

Here, the wave function ψ is expressed as $\psi = |\psi| e^{i\theta}$, where θ is the phase associated with the wave function. ϕ_0 represents the magnetic flux quanta, while ξ is the superconducting coherence length, which characterizes the extent of the wave function influence outside the superconductor, as $|\psi| \propto \psi_0 e^{-x/\xi}$, where x is the distance from the superconductor surface. The coherence length characterizes the Proximity Effect, which is the ability of a superconducting wave function to extend beyond the physical boundaries of a material, inducing superconductivity in a nearby material.

Subsequently, the microscopic theory of superconductivity emerged, which offered an explanation based on the behavior of the charge carriers in the material, rather than on phenomenological approaches. The BCS theory [30] states that the charge carriers responsible for superconductivity are not individual electrons, but rather Cooper pairs [31], boson quasiparticles formed by paired electrons. This theory was named after J. Bardeen, L. Cooper, and J. Schrieffer, recognized with the 1972 Nobel Prize in Physics [32].

The BCS formalism provides a theoretical framework that accounts for the attractive interaction, mediated by phonons, between electrons in the vicinity of the Fermi surface.

The BCS Hamiltonian consists of two terms: a kinetic term and an additional term related to the effective interaction between electrons, upon "integrating out" phonons. Specifically, the effective Hamiltonian is given by

$$\hat{H} = \sum_{\mathbf{k}\sigma} \epsilon_{\mathbf{k}} c_{\mathbf{k}\uparrow}^\dagger c_{-\mathbf{k}\downarrow} - \frac{g}{V} \sum_{\mathbf{k}, \mathbf{k}'} c_{\mathbf{k}\uparrow}^\dagger c_{-\mathbf{k}\downarrow}^\dagger c_{-\mathbf{k}\downarrow} c_{\mathbf{k}\uparrow}. \quad (2.7)$$

Here, the interaction constant g represents the attractive interaction with energies of the order of the Debye energy between electrons near the Fermi surface. This Hamiltonian characterizes s-wave superconductors, spin-singlet with $S = 0$, $L = 0$ Cooper pairs, in which the paired electrons have no relative angular momentum. The presence of the volume normalization factor V is necessary to ensure that the interaction energy is extensive, meaning that it grows linearly with volume. The Cooper pair formation arises from lattice vibrations, phonons, with large wave numbers $q \sim k_F$. These phonons mediate the interaction between electrons. To understand the nature of this phenomenon, we need to consider two time scales. The first is the time scale of the electron propagating between sites in the lattice with a given spacing l , which can be translated approximately as E_F^{-1} . The second is the relaxation lattice time, which is determined by the Debye frequency ω_D , where $\omega_D \gg E_F^{-1}$. Once an electron passes through the lattice, the lattice is deformed and needs time to relax to its equilibrium position and a second following electron can take advantage of the deformed lattice for a time $\sim 1/\omega_D$. This is the reason why the superconducting interaction effects occurs at a specific energy scale around the Debye frequency for electrons near the Fermi surface. The Cooper pairs form a condensate below a critical temperature T_c , which is responsible for the superfluid current carried by these bosons with a charge of $2e$. For higher-temperature superconductors, spin fluctuations may play a significant role in the pair formation.

2.2 Andreev Reflection

Electrons typically serve as the primary charge carriers in normal metals, whereas in superconductors, charge is carried by Cooper pairs, which consist of two electrons. When considering an interface (NS) between a normal metal and a superconductor, it is observed that current flows between the interfaces, despite the distinct nature of the charge carriers. To provide a theoretical explanation for this phenomenon, the concept of Andreev

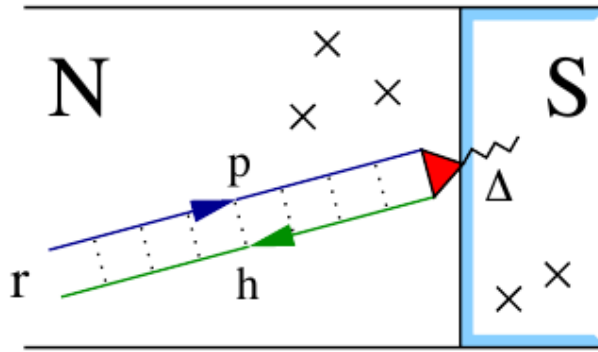


Figure 2.3: An incoming electron and its reflected hole giving rise to a Cooper pair entering the condensate after Andreev reflection. Image Credits [33].

reflection has been developed. As a quasielectron from the normal metal approaches the interface, it undergoes reflection and transforms into a quasihole with inverted velocity, spin, charge and phase. Meanwhile, in the superconductor, a Cooper pair is formed.

In the normal (N) region, an incoming electron propagates diffusively due to impurities. The NS interface refers to the region where the superconducting wave function extends into N, up to the coherence length, where it reaches its maximum value within the superconductor. At this point, the electron starts experiencing the influence of superconductivity. Upon passing through the NS interface, a hole is retro-reflected in this process. However, an interesting scenario arises when this reflected hole diffuses along the same path as the incoming electron, possessing opposite energy and spin. Consequently, the disordered averaged quantity $\langle c_{\uparrow}^{\dagger}(\mathbf{r}, 0)c_{\downarrow}^{\dagger}(\mathbf{r}, t) \rangle$ becomes non-zero. Unlike cases with generic reflected paths that vanish upon disorder averaging, the phases of these oppositely propagating particles cancel out due to their opposite paths, leading to non-vanishing results. This robustness of the Cooper pair correlations $\langle c_{\uparrow}^{\dagger}(\mathbf{r}, 0)c_{\downarrow}^{\dagger}(\mathbf{r}, t) \rangle$ attributes superconducting correlations in the normal metal induced by the nearby superconductivity and characterizes the proximity effect. Since the incoming electron and the reflected hole possess opposite energies, energy conservation dictates that the resulting energy is transferred to the condensate along with the Cooper pair.

2.3 Josephson Junctions

The proximity effect makes it possible to induce a superconducting gap in systems that are located close to a superconductor. This opens up new possibilities for material config-

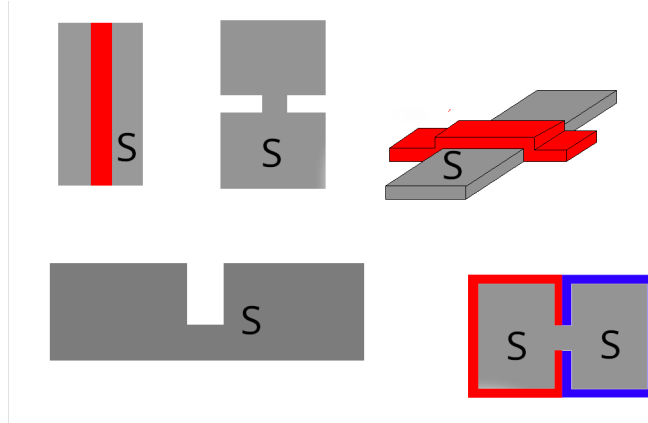


Figure 2.4: The image displays various weak link configurations, with gray representing superconductors and red representing other materials such as insulators or metals. From left to right and top to bottom, we see a sandwich junction, which is later identified as a Josephson junction; a top view of a Dayem bridge with a shorter funnel on the coherence length scale [35]; a superposition of films, where the supercurrent is affected by the cover; a longitudinal cross-section of a junction with variable thickness; and a grain-boundary junction, which is also a Dayem bridge, with the superconductor connected to a different material. Today, there are an infinite number of nano configurations for weak links. A good example of their practical use is the Superconducting Quantum Interference Device (SQUID). A review by Likharev [36] covers several configurations.

urations, including weak links between superconducting leads. Such configurations utilize the properties of weak superconductivity and interference between wave functions with different phases associated. When two identical superconductors are under the same conditions, they exhibit the same properties such as critical temperatures, coherence, and penetration lengths. Although their wavefunctions must have the same amplitude, their phases may naturally differ. This phase difference creates new phenomena when the two superconductors interact weakly.

There exists an infinite number of configurations that result in producing weak links of superconductivity. These configurations can include a strangled neck along a superconductor, a sandwich where a different material is placed between the superconductors, or a superposition of other materials. All of these configurations operate on dimensions that are of the order of the coherence length, which enables the proximity effect to modify the states near the Fermi surface.

STIS Junctions are systems that consist of a superconductor – topological insulator – superconductor structure, sometimes as a "sandwich" of the materials. Josephson effects, which are the result of weak superconductivity, were first predicted by B. Josephson [37]. This phenomenon is possible due to the proximity effect of superconductors. In a sandwich

junction, electrons tunnel between the superconductors separated by a potential barrier, establishing a proximity that is not so close as to completely alter the electron states on both superconductors, but rather close enough for their wave functions to overlap. Although, as stated, the characteristics of both superconductors can be the same, the phase of their wave functions is not related. As a result of this overlap, phase coherence along the junction is achieved, enabling the generation of a supercurrent between the SCs. The Josephson effect can create different phenomena, such as the presence of magnetic flux quanta orthogonal to the current propagation and high-frequency electromagnetic waves [38, 39], that can have practical use.

In its simplest form, a Josephson junction can be viewed as a two-level quantum system. Following Feynman [40], we consider Cooper pairs with $2e$ charge flowing through a junction creating a current subjected to a voltage V in a circuit. The energy levels $E_1 = eV$ and $E_2 = -eV$ are occupied by the pairs and the transition energy is $E_{12} = E_{21} = E_T$, for E_{12} as the energy transition from levels $1 \rightarrow 2$ and E_{21} for the opposite. The Schrödinger equation for this system is

$$i\hbar \frac{d\Psi_1}{dt} = E_1\Psi_1 + E_T\Psi_2, \quad (2.8)$$

$$i\hbar \frac{d\Psi_2}{dt} = E_2\Psi_2 + E_T\Psi_1, \quad (2.9)$$

where $\Psi_p \sim \sqrt{n_s}e^{i\theta_p}$, for θ_p , $p = 1, 2$, as the phase of the superconductors and $\sqrt{n_s}$ as the square root of the pairs density in the junction. Upon substituting Ψ_p , taking the difference between equations and separating real and imaginary parts we get for the charge density

$$\frac{dn_s}{dt} = \frac{2E_T n_s}{\hbar} \sin \phi, \quad \phi = \theta_2 - \theta_1. \quad (2.10)$$

Since the current through the junction is proportional to dn_s/dt , we understand that the current through a tunnel Josephson junction is proportional to $\sin \phi$,

$$j_s = j_c \sin \phi, \quad (2.11)$$

with j_c the maximum supercurrent through the junction. In other words, the current is modulated by the phase difference between the two superconductors. This simple model

helps us to understand the essential role that ϕ plays in the junction current. In the presence of disorder these currents exhibit mesoscopic fluctuations. Previous studies of mesoscopic fluctuations have been conducted for SNS (Superconductor-Normal Material-Superconductor) systems, where a normal metal is sandwiched between the superconducting leads [43]. In the following sections, we will calculate the current and its fluctuations for a system with topological insulators as a layer of the junction.

2.4 From BCS to BdG

To develop a more advanced study on the Josephson current, we need to use a more advanced mathematical model. The BCS Hamiltonian is a suitable starting point for such an analysis, as it directly deals with Cooper pairs. Referring to our previous discussion, on the evolution of superconductivity theory, where we introduced the Hamiltonian (2.7), we return to it

$$\hat{H} = \sum_{\mathbf{k}\sigma} \epsilon_{\mathbf{k}} c_{\mathbf{k}\sigma}^\dagger c_{-\mathbf{k}\sigma} - \frac{g}{V} \sum_{\mathbf{k}} c_{\mathbf{k}\uparrow}^\dagger c_{-\mathbf{k}\downarrow}^\dagger c_{-\mathbf{k}\downarrow} c_{\mathbf{k}\uparrow}. \quad (2.12)$$

We now develop a path integral formulation to construct a generating function by substituting the creation and annihilation operators in the Hamiltonian with equivalent coherent state Grassmann variable fields. These fields are denoted as $\bar{\chi}$ and χ and obey fermionic anti-commuting algebra, where $\bar{\chi}\chi = -\chi\bar{\chi}$ and $\chi^2 = 0$. The generating function we obtain is [44]:

$$Z = \int d(\bar{\chi}, \chi) e^{-S(\bar{\chi}, \chi)}, \quad (2.13)$$

where

$$S = \int_0^\beta d\tau \int d^d \mathbf{r} [\bar{\chi}_\sigma (\partial_\tau + \epsilon_{\mathbf{k}} - \mu) \chi_\sigma - g \bar{\chi}_{\mathbf{k}\uparrow} \bar{\chi}_{-\mathbf{k}\downarrow} \chi_{-\mathbf{k}\downarrow} \chi_{\mathbf{k}\uparrow}]. \quad (2.14)$$

Using a mean field theory, we understand that the fields couple via local attractive interaction to form pairs of the type $\Delta = \frac{g}{V} \langle \bar{\chi}_{\mathbf{k}\uparrow} \bar{\chi}_{-\mathbf{k}\downarrow} \rangle$ and $\bar{\Delta} = \frac{g}{V} \langle \chi_{-\mathbf{k}\downarrow} \chi_{\mathbf{k}\uparrow} \rangle$. To rewrite the interacting part of the Hamiltonian, the one mediated by g , we perform a Hubbard-Stratonovich [45, 46] transformation and get

$$Z = \int d(\bar{\Delta}, \Delta) e^{-\int_0^\beta d\tau \int d^d \mathbf{r} (\frac{1}{g} \Delta \bar{\Delta} + (\Delta \bar{\chi}_{\mathbf{k}\uparrow} \bar{\chi}_{-\mathbf{k}\downarrow} + \bar{\Delta} \chi_{-\mathbf{k}\downarrow} \chi_{\mathbf{k}\uparrow}))}. \quad (2.15)$$

The Hubbard-Stratonovich transformation can be viewed as the opposite of the trick of completing the square for a binomial product. The Δ and $\bar{\Delta}$ bosonic fields are intensive variables that represent the many-body macroscopic properties of the superconducting system. Due to their intensive nature, fluctuations are negligible in the thermodynamic limit. From the perspective of Ginzburg-Landau theory [28], these fields represent the order parameter of phase transitions and set the gap of the superconducting system. The action can be rewritten compactly using Nambu spinors, defined as:

$$\psi = \begin{pmatrix} \chi_{\mathbf{k}\uparrow}(\epsilon) \\ \bar{\chi}_{-\mathbf{k}\downarrow}(-\epsilon) \end{pmatrix}, \quad \bar{\psi} = \begin{pmatrix} \bar{\chi}_{\mathbf{k}\uparrow}(\epsilon) & \chi_{-\mathbf{k}\downarrow}(-\epsilon) \end{pmatrix}. \quad (2.16)$$

This enables us to rewrite the generating function as:

$$Z = \int d(\bar{\psi}, \psi) d(\bar{\Delta}, \Delta) e^{-\int_0^\beta d\tau \int d^d\mathbf{r} (\frac{1}{g}\Delta\bar{\Delta} + \psi G^{-1}\bar{\psi})} \quad (2.17)$$

where

$$G^{-1} = \partial_\tau - \begin{pmatrix} \epsilon_{\mathbf{k}} & \Delta \\ \bar{\Delta} & -\epsilon_{\mathbf{k}} \end{pmatrix} = \partial_\tau - H_{BdG}, \quad (2.18)$$

and H_{BdG} is the Hamiltonian of Bogoliubov - de Gennes or Gorkov. One can understand the negative energy term in the lower diagonal as one a hole created in the theory. This new Hamiltonian will be used in later sections to construct our model for STIS junctions. It can explicitly handle the electron-hole degrees of freedom required to account for the interface of Andreev reflections between the superconductors and surface states of TI's.

Chapter 3

Topological Insulators

The field of condensed matter physics has found a new application for the concept of topology, thanks to the discovery of topological insulators. Upon closer examination, it became clear that these insulators possess intriguing topological properties, including topologically protected conducting surface states. An important aspect of this behavior is the presence of a topological invariant, which remains unchanged during specific topological transformations, such as smooth deformations of parameters, adding disorder, etc. These invariants are crucial as they capture the global structure and properties of a system and are protected by the energy gap between valence and conduction band in band insulators and gap for excitations in superconductors. Any changes in the Hamiltonian that do not violate fundamental symmetries or close the gap cannot change topological properties. A well-known example of a topological invariant in condensed matter physics is the Chern number [47].

For topology in gapped systems that can be described by quadratic hamiltonians, a table can be defined to establish the relationships between groups of topological invariants based on the dimension and the discrete symmetry class associated with the model. These relations stem from Random Matrix Theory, which encompasses 10 symmetry classes. These symmetry classes are composed of combinations of time-reversal, particle-hole (charge conjugation), and chiral (sublattice) symmetries. Tables 3.1 and 3.2 can be used to represent and define these relationships. Next, we are going to explore some examples defined by the table, such as the Quantum Hall Effect, which is probably the most known example of a TI, and Kitaev's Majorana chain, earlier mentioned. We then introduce the 3D Spin Hall Effect, which is the one relevant for this work.

Symmetry Class	Time reversal symmetry	Particle hole symmetry	Chiral symmetry
A	×	×	×
AIII	×	×	✓
AI	✓, $T^2 = 1$	✓	×
BDI	✓, $T^2 = 1$	✓, $C^2 = 1$	✓
D	×	✓, $C^2 = 1$	×
DIII	✓, $T^2 = -1$	✓, $C^2 = 1$	✓
AII	✓, $T^2 = -1$	×	×
CII	✓, $T^2 = -1$	✓, $C^2 = -1$	✓
C	×	✓, $C^2 = -1$	×
CI	✓, $T^2 = 1$	✓, $C^2 = -1$	✓

Table 3.1: This is the table of discrete symmetry classes. Here, T stands for time-reversal symmetry operator, for $T = U_T K$, being U_T an unitary matrix $U_T H^* U_T^{-1} = H$, and K complex conjugation operator. C stands for particle-hole symmetry, for $C = U_C K$, being U_C an unitary matrix $U_C H^* U_C^{-1} = -H$. S stands for chiral symmetry, where $S c_i S^{-1} = (U_S)_{ij} c_j$. According to the relation $S = TC$ it is known that if at least of two of the symmetries (S, T, C) are present, all are.

Symmetry Class	$d = 0$	$d = 1$	$d = 2$	$d = 3$	$d = 4$	$d = 5$	$d = 6$	$d = 7$	$d = 8$
A	\mathbb{Z}	0	\mathbb{Z}	0	\mathbb{Z}	0	\mathbb{Z}	0	\mathbb{Z}
AIII	0	\mathbb{Z}	0	\mathbb{Z}	0	\mathbb{Z}	0	\mathbb{Z}	0
AI	\mathbb{Z}	0	0	0	$2\mathbb{Z}$	0	\mathbb{Z}_2	\mathbb{Z}_2	\mathbb{Z}
BDI	\mathbb{Z}_2	\mathbb{Z}	0	0	0	$2\mathbb{Z}$	0	\mathbb{Z}_2	\mathbb{Z}_2
D	\mathbb{Z}_2	\mathbb{Z}_2	\mathbb{Z}	0	0	0	$2\mathbb{Z}$	0	\mathbb{Z}_2
DIII	0	\mathbb{Z}_2	\mathbb{Z}_2	\mathbb{Z}	0	0	0	$2\mathbb{Z}$	0
AII	$2\mathbb{Z}$	0	\mathbb{Z}_2	\mathbb{Z}_2	\mathbb{Z}	0	0	0	$2\mathbb{Z}$
CII	0	$2\mathbb{Z}$	0	\mathbb{Z}_2	\mathbb{Z}_2	\mathbb{Z}	0	0	0
C	0	0	0	$2\mathbb{Z}$	0	\mathbb{Z}_2	\mathbb{Z}_2	0	0
CI	0	0	0	$2\mathbb{Z}$	0	\mathbb{Z}_2	\mathbb{Z}_2	\mathbb{Z}	0

Table 3.2: This table relates the discrete symmetry classes, as stated in the previous table, and the dimension of the system, from $0D$, point-like systems, to $3D$, bulk materials, and so on. This table is called "periodic" for it repeats after $8D$, which is the same as $0D$, as it can be seen, that is, the system is invariant over $d + 8$ dimensions. The factors of \mathbb{Z} and $2\mathbb{Z}$ represent topological materials that are characterized by an integer, the Chern or winding number, for odd or even integers, respectively. While \mathbb{Z}_2 represents the group of integers modulo 2, which means it can take only two values: 0 and 1. It indicates the presence or absence of surface states with protected properties, respectively.

Quantum Hall Effect - QHE - The concept of topological insulators can be traced back to the seminal works of Laughlin [48], Thouless [49], Haldane [50], and their collaborators in the context of the quantum Hall effect. In the classification table it fits a 2D model in class *A*. In a similar fashion to the classical Hall effect, this phenomenon occurs in a two-dimensional system under the influence of low temperatures and a strong magnetic field perpendicular to the 2D plane. In the quantum Hall effect, the current passing through the system is redirected towards the edges while the bulk behaves as an insulator. In the quantum version it presents a quantized transversal Hall resistance,

$$R_{QHE} = \frac{h}{e^2\nu}, \quad \nu \in \mathcal{N}, \quad (3.1)$$

where ν are Chern numbers characterizing this phenomenon. Figure 3.1 and Appendix B gives more details on the physics. There is also the possibility to create this quantized resistance without the use of an external magnetic field. This can be achieved through the breaking of time-reversal symmetry due to the sublattice hoppings of graphene for the Haldane model [50], such effect is similar to the application of a magnetic field and brings new possibilities in constructing similar models.

Majorana Fermions - The Kitaev chain, Figure 3.2, is an example that covers the 1D materials of class *D*, where the particle-hole symmetry comes from the superconducting states. This model is constructed to form edge states of Majorana fermions. As already mentioned in the Introduction this system considers a 1D linear chain of electrons with p-wave pairing. These electrons can be viewed as formed by two Majoranas. Assuming binding factor parameters in a superconducting system it can be shown that edge states of non-local Majorana states are possible, one Majorana on each edge of the chain. The Hamiltonian

$$H = -\mu c_n^\dagger c_n - t(c_{n+1}^\dagger c_n + c_n^\dagger c_{n+1}) + \Delta(c_n c_{n+1} + c_{n+1}^\dagger c_n^\dagger) \quad (3.2)$$

represents this model, here μ is the chemical potential, t a binding factor between Majoranas and Δ the superconducting pairing. Figure 3.2 shows an electron chain, where these electrons hosts two Majorana modes each. It can be established connection between adjacent Majoranas of two types, one for Majoranas belonging to the same electron, and Majoranas belonging to adjacent electrons, as it is shown in the two coloured examples

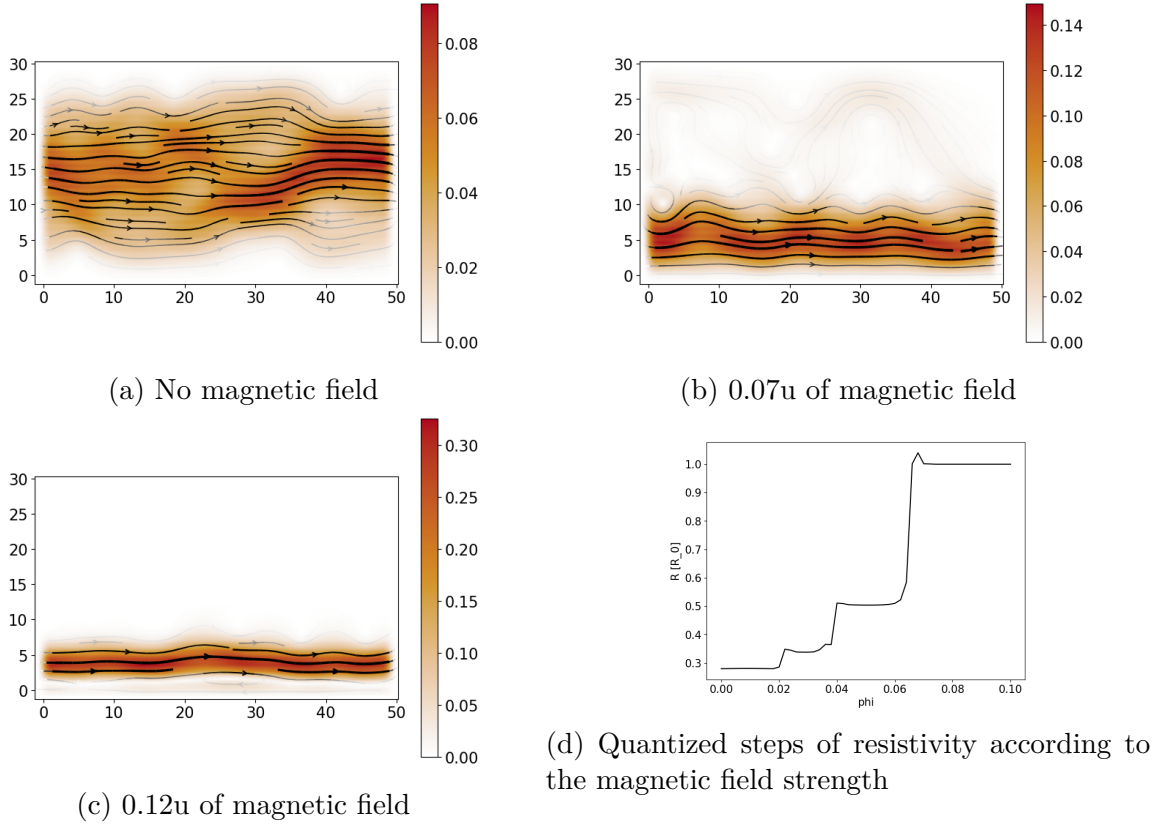


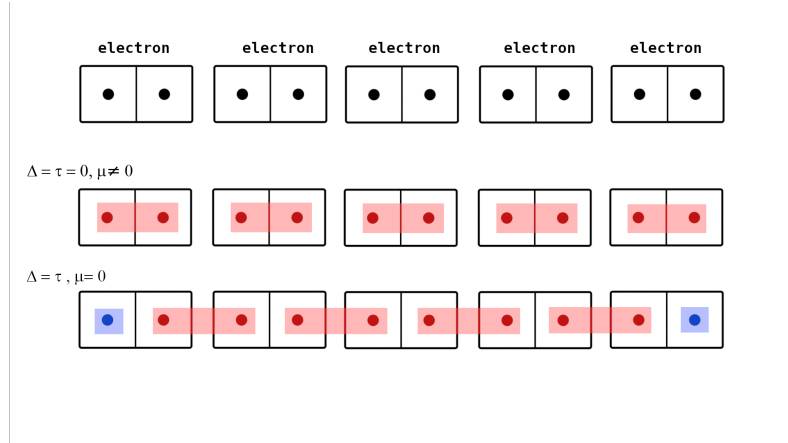
Figure 3.1: QHE: Here u stands for unity of magnetic field, since the code is not using realistic parameters to perform calculations. A top view of a 2D conducting surface, Figure (a), reveals an interesting phenomenon when a magnetic field is applied perpendicular to the current flow. In this scenario, the current concentrates along the edges of the surface leaving the bulk as an insulator. This occurrence can be attributed to the influence of the magnetic field, which exerts a Lorentz force on the electrons, causing them to follow circular orbits. As a result, a continuous current flow is not generated; instead, near the edges, the circular electron orbits can reflect and lead to skipping orbits. Consequently, current is observed along the edges of the surface. These localized states as known as Landau levels. Although the current keeps concentrating at the edge, for some values of magnetic flux, the current is spread again due to presence of disorder, as illustrated in Figure (b). As the magnetic field strength increases the electron orbits become smaller and more localized, due to the increasing spacing of Landau levels, Figure (c). In the absence of disorder, the quantized steps corresponding to Landau levels are well-defined. The presence of disorder introduces scattering, which adds some noise to the states, although the levels keep well defined, with perfectly quantized Hall plateaus, Figure (d). Graphics generated with an adapted model in Kwant [13], the code is available in Appendix B.

of Figure 3.2, where the red bars stand for these hoppings. This Hamiltonian comes from summing the two types of binding contributions, one for the pairing of Majoranas within each electron $H = (i/2)\mu\gamma_{2n-1}\gamma_{2n}$, summed over the pairing between Majoranas in adjacent electrons $H = it\gamma_{2n+1}\gamma_{2n}$, with the definitions of $\gamma_{2n-1}, \gamma_{2n}$ for odd and even Majoranas, respectively, following the chain order, then

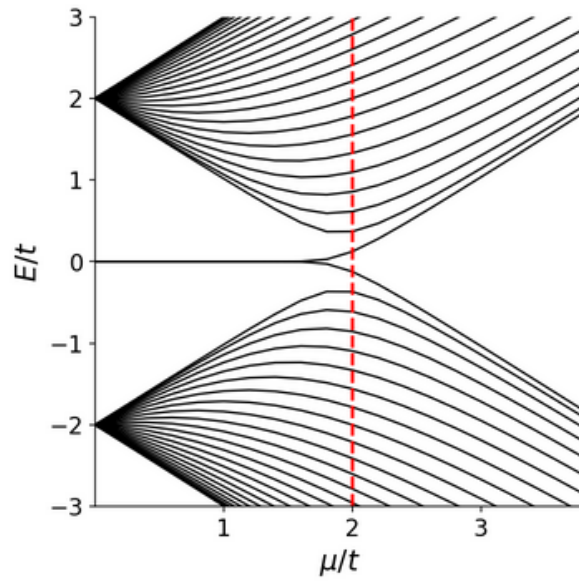
$$\gamma_{2n-1} = (c_n^\dagger + c_n), \quad \gamma_{2n} = -i(c_n^\dagger - c_n), \quad (3.3)$$

where c_n^\dagger, c_n are creation and annihilation electron operators. When $\Delta = t, \mu = 0$ we are in the regime of unpaired Majoranas at the edges, for the Majoranas are connected by adjacent electrons and the two Majoranas at the edges are isolated. $\Delta = t = 0, \mu \neq 0$ is the regime of isolated electrons, there is no superconductivity to bind the electrons together, so the Majoranas can only bind within each electron. Starting from these parameters choice and increasing them, it can be shown that the system keeps unpaired Majorana modes until energies within the range of $\mu = 2t$. These two edge states are separated by a superconducting gapped medium Δ . In a system that is particle-hole symmetric, the energy spectrum exhibits symmetry around zero energy. For $\mu = 0$, Majorana modes appear at the edges, which cannot be brought together due to the distance, or individually moved without violating the symmetry. They are dependent of each other, similar to removing a pole from a magnet, it is not possible to remove a single edge state.

Finally, we introduce the system of relevance for this work. This is the 3D Quantum Spin Hall system in Class AII. The works of Kane [51], Bernevig [52], Roy [53] and Moore [54] have extended the concept of the Hall effect to spin currents. The Kane-Méle model [51] specifically demonstrates this phenomenon in 2D graphene ribbons, where it is observed that the edges of the ribbon exhibit conducting behavior. This approach considers the hoppings between the two sublattices of graphene, which create a Dirac cone structure in the energy bands. It uses spin-orbit interaction to open a gap while keeping time-reversal symmetry. Spin-orbit interaction couples the spin of an electron to its momentum, as opposite to Haldane model, a system also built from graphene but that uses the sublattice hoppings. As a result, a gapped medium is formed in the bulk of the material, while the edges exhibit gapless states. It suggests that time-reversal symmetry protects these edge states. Subsequently, Fu, Kane, and Méle [55] introduced a three-dimensional model that generalizes the spin Hall effect, a 3D system in class AII. Zhang et al [56] extrapolated



(a)



(b)

Figure 3.2: a) Kitaev model, a chain of electrons, where each electron accommodates two Majorana modes that can interact to each other. This interaction occurs between Majoranas belonging to the same electron and Majoranas belonging to adjacent electrons, as depicted in the second and third lines. In these examples, the red bars represent the bidings. b) Band structure showing the persistence of edge zero modes of Majorana fermions.

the search of Dirac cones for Bi_2Se_3 , Bi_2Te_3 and Sb_2Te_3 crystals showing surface states consisting of a single Dirac cone, leading to "massless" electrons with linear momentum coupled to its spin.

As we detail in the next chapter, we are here interested in a Josephson junction of a 3D TI and s-wave superconductors. Following [57], we are going to consider the 3D TI Hamiltonian

$$H_0 = H_{bulk} + H_{surf.} + H_{coupl.}, \quad (3.4)$$

where H_{bulk} comprise the insulating bulk and $H_{surf.}$ the metallic surface states,

$$H_{bulk} = M\mathbb{I}_2 \otimes \tau_z + \hbar v_B \mathbf{k} \cdot \sigma \otimes \tau_x, \quad (3.5)$$

$$H_{surf.} = \hbar v_S \mathbf{k}_{\parallel} \cdot \sigma. \quad (3.6)$$

Here, $\mathbf{k}_{\parallel} = (k_x, k_y)$ and $\mathbf{k} = (\mathbf{k}_{\parallel}, k_z)$ are the surface and bulk momenta, respectively, and τ_i and σ_i are Pauli matrices for orbital and spin degrees of freedom with $i = x, y, z$. $H_{coupl.}$ connects the bulk and surface states, but for our calculation for the STIS the bulk will not be a relevant part, as for its coupling with $H_{surf.}$. The bulk Hamiltonian corresponds to the strong topological phase that generates a single Dirac cone on the surface. This model provides an effective low-energy description, e.g. for Bi_2Se_3 TI cited before. Usually, to guarantee an insulating bulk, H_{bulk} has a large band gap, as opposition to $H_{surf.}$, that is conducting. In this type of topological insulator there are narrow bulk band gaps, which can give rise to the presence of accidental impurities or vacancies. Consequently, these impurities tend to occupy the bulk conduction band, leading to fluctuations in the transport properties of the system due to interference effects. For our STIS Josephson Junction, to be developed in the next section, we will make use of this model (3.4), accounting only for the topological surface states described by $H_{surf.}$ coupled to superconductors placed on top of the 3D TI. A crucial part is to also account for the disorder on the surfaces, leading to sample-to-sample fluctuation in the Josephson current.

Chapter 4

STIS Junction

Building upon the previous model of a 3D topological insulator, our next step involves coupling it to s-wave superconductors. This configuration will serve as basis of our STIS Josephson junction. We aim to develop an effective theory from which we can calculate the average Josephson current flowing through the junction and sample-to-sample fluctuations in the currents due to disorder on the TI surfaces. Specifically, we assume that order parameters of the superconductors have the same absolute value but tunable phase difference, which drives the Josephson current. The presence of disorder on the TI surface, present in any experiment, leads to sample-to-sample fluctuations and we calculate the supercurrent $I(\phi)$ and fluctuations $varI(\phi_1, \phi_2)$ across different samples as functions of the phase differences between the superconductors.

The chapter unfolds as follows: Firstly, in Section 4.1 we define the STIS junction Hamiltonian and subsequently derive an effective Hamiltonian for our system. We construct a generating function for the Josephson current and its fluctuations in terms of an effective field theory in the following sections: In Section 4.2 we expand the dimensionality of the field theory to accommodate the introduction of the Replica trick. We then introduce the sample space in order to calculate sample-to-sample fluctuations. Upon developing on disorder averaging in Section 4.3, we proceed to calculate a saddle point equation of the effective action in Section 4.4 and after a gradient expansion in Section 4.5 we perform a refined version of the saddle point equation ("Usadel equation") in Sections 4.6 and 4.7. We then calculate the density of states in Section 4.8. We introduce a parametrization of the effective field theory in Section 4.9 capable of calculating both the average current and fluctuations in presence and absence of a finite magnetic field, in Sections 4.10 and

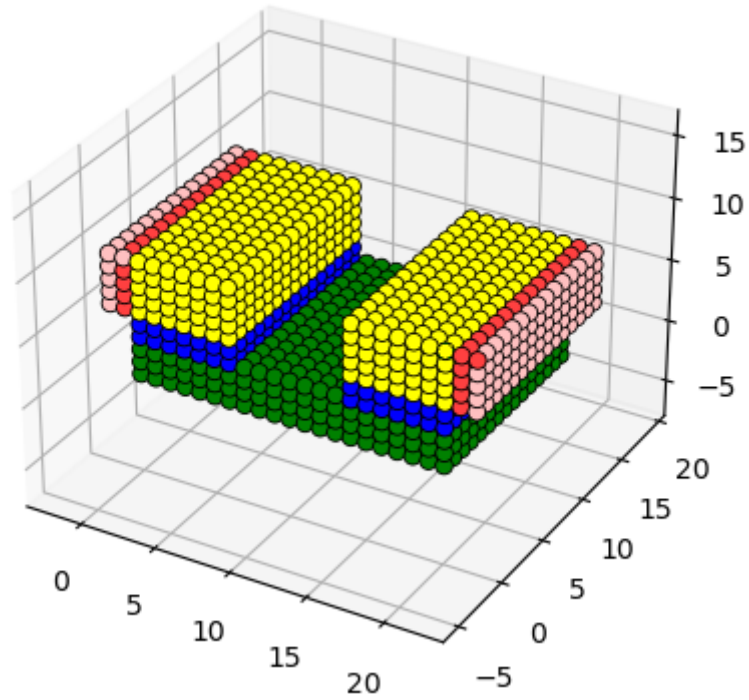


Figure 4.1: A model of the STIS junction, already illustrated in the Introduction. The green component is a TI thin film. Yellow bases represent the two superconductors. In blue we have a tunnelling interface, for computational reasons. The red part is a lead that connects to external electrical current. For our system, each color part addresses a Hamiltonian sector in (4.1). Integrating over the superconductor degrees of freedom we derive an effective theory for the TI-surface that accounts for the coupling to the superconductors. This figure is the plot of a model developed using Kwant [13], to perform simulations of Josephson currents on STIS.

4.11, respectively.

4.1 Building an Action

To model the Josephson junction the Hamiltonian of the TI junction is modified accordingly, consisting now of three elements: one for the superconductors, one for the topological insulator, and one for the coupling between them. For the next calculations we are assuming $\hbar = 1$ to simplify calculations. The Hamiltonian thus reads:

$$\hat{H}_{jun} = \hat{H}_{TI} + \hat{H}_{BdG_1} + \hat{H}_{BdG_2} + \hat{H}_{Tun}. \quad (4.1)$$

Here the Hamiltonian for the topological insulator reads: $\hat{H}_{TI} = \hat{H}_{surf} + \hat{H}_{dis}$, with:

$$\hat{H}_{surf} = v \begin{pmatrix} \mathbf{k} \cdot \boldsymbol{\sigma} & 0 \\ 0 & -\mathbf{k} \cdot \boldsymbol{\sigma} \end{pmatrix}, \quad (4.2)$$

as already introduced in the last chapter, where $\mathbf{k} = (k_x, k_y)^t$ is the momentum of the surface states, $\boldsymbol{\sigma}$ the Pauli matrices, v the velocity of the surface states, and

$$\hat{H}_{dis} = V(\mathbf{r})\mathbb{I}_2, \quad (4.3)$$

is a random disorder potential depending on the two dimensional coordinate \mathbf{r} . As usual, we assume a Gaussian distribution for the disorder potential with first and second moment,

$$\langle V(\mathbf{r}) \rangle = 0, \quad (4.4)$$

$$\langle V(\mathbf{r})V(\mathbf{r}') \rangle = \frac{1}{2\tau} \delta(\mathbf{r} - \mathbf{r}'), \quad (4.5)$$

respectively, where τ is the elastic scattering time.

To account for superconductivity at the boundaries, we introduce Nambu spinors. These spinors are selected in a manner that maintains the standard structure of the Bogoliubov-de Gennes Hamiltonian and Gorkov Green's functions, providing us with greater flexibility

in performing the next calculations. The Nambu spinors are defined as follows:

$$\Psi = \begin{pmatrix} \chi_{\mathbf{k}\uparrow}(\epsilon) \\ \chi_{\mathbf{k}\downarrow}(\epsilon) \\ -\bar{\chi}_{-\mathbf{k}\downarrow}(-\epsilon) \\ \bar{\chi}_{-\mathbf{k}\uparrow}(-\epsilon) \end{pmatrix}, \quad \bar{\Psi} = \left(\chi_{\mathbf{k}\uparrow}(\epsilon) \quad \chi_{\mathbf{k}\downarrow}(\epsilon) \quad -\bar{\chi}_{-\mathbf{k}\downarrow}(-\epsilon) \quad \bar{\chi}_{-\mathbf{k}\uparrow}(-\epsilon) \right), \quad (4.6)$$

with ϵ the Matsubara energies to be summed later, and $\psi, \bar{\psi}$ as the topological counterparts of the spinors. Also, note the relation

$$\Psi^t = \bar{\Psi} i\sigma_2^s \otimes i\sigma_2^{ph} \quad (4.7)$$

where 's' stands for spin (space) and 'ph' particle-hole (space). We can then write the surface Hamiltonian in Nambu space

$$\hat{H} = \sum_{\mathbf{k}} v \bar{\psi}(\mathbf{k}) \begin{pmatrix} \mathbf{k} \cdot \boldsymbol{\sigma} & 0 \\ 0 & -\mathbf{k} \cdot \boldsymbol{\sigma} \end{pmatrix} \psi(\mathbf{k}). \quad (4.8)$$

Superconductors are described by the BdG Hamiltonian

$$\hat{H}_{BdG} = \sum_{\mathbf{k}} \begin{pmatrix} \hat{H}_0 & \Delta_s \\ \bar{\Delta}_s & -\hat{H}_0^t \end{pmatrix} \otimes \mathbb{I}_2^s, \quad \hat{H}_0 = \mathbf{k}/2m, \quad (4.9)$$

where \mathbb{I}_2^s is the identity matrix in spin space, and $\Delta_s = \Delta e^{i\phi_s}$, $s = 1, 2$, indicating each superconductor, with ϕ_s as its associated phase difference. Regarding the tunneling Hamiltonian, we keep the following form:

$$\hat{H}_{Tun} = \sum_{s=1,2} \int dy W_s \bar{\Psi}(\mathbf{r}_s^-) \psi(\mathbf{r}_s^+) + h.c., \quad (4.10)$$

where we consider a junction of length L centered at the origin and superconductor leads that starts at $|x| \geq L/2$. $\mathbf{r}_s^\pm = (\text{sgn}(i) * L/2 \pm \delta, y)$ are coordinates to account for the tunneling interface, with s indicating superconductors 1 and 2 as the coordinates of the interfaces of the junction, δ as a small value of deviation from the boundary.

Considering that the superconductor leads are significantly larger than the TI film in between, we can neglect pair breaking in the superconductors due to an inverse proximity

effect. Additionally, depairing effects in the leads can be ignored for consideration of maintaining a finite current density through the junction. With this assumption, we can perform a Gaussian integration for the superconductor and tunneling Hamiltonians. To accomplish this, we need to account that $i\epsilon + \hat{H}_{BdG} = G_{BdG}^{-1}$, which defines the inverse BdG Green's function. Also, we introduce the Matsubara formalism, where $\epsilon_n = (2n + 2)\pi T$ are the fermionic Matsubara energies. This results in:

$$S = \sum_n \int d\mathbf{r} \bar{\psi}_n \left(-i\epsilon_n + \hat{H}_{TI}\sigma_3^{ph} + \hat{H}_\Gamma - \mu\sigma_3^{ph} \right) \psi_n \quad (4.11)$$

where

$$\hat{H}_\Gamma = \sum_{s=1,2} \int d\mathbf{r} W_s^\dagger G_{BdG_s}(\mathbf{r}, \mathbf{r}') W_s \quad (4.12)$$

$$= \sum_{s=1,2} \int d\mathbf{k} W_s^\dagger G_{BdG_s}(\mathbf{k}) W_s \quad (4.13)$$

$$= \sum_{s=1,2} \int d\epsilon \nu(\epsilon) W_s^\dagger G_{BdG_s}(\epsilon) W_s \quad (4.14)$$

$$\approx \sum_{s=1,2} \nu_0 \int d\epsilon W_s^\dagger G_{BdG_s}(\epsilon) W_s \quad (4.15)$$

$$= \sum_{s=1,2} \int d\epsilon \frac{\nu_0 |w|^2}{(i\epsilon_n)^2 - \epsilon^2 - \Delta^2} \begin{pmatrix} i\epsilon_n + \epsilon & \Delta \\ \Delta & i\epsilon_n - \epsilon \end{pmatrix} \quad (4.16)$$

$$= - \sum_{s=1,2} \frac{\nu_0 \pi |w|^2}{\sqrt{\epsilon_n^2 + \Delta^2}} \begin{pmatrix} i\epsilon_n & \Delta \\ \Delta & i\epsilon_n \end{pmatrix} \quad (4.17)$$

$$= - \sum_{s=1,2} \frac{E_t}{\sqrt{\epsilon_n^2 + \Delta^2}} \begin{pmatrix} i\epsilon_n & \Delta \\ \Delta & i\epsilon_n \end{pmatrix}. \quad (4.18)$$

The first step was a Fourier transformation. In the fourth line we approximated the density of states to be constant. The integration in the fifth line is resolved around a pole in $\sqrt{\epsilon_n^2 - \Delta^2}$.

4.2 Replica Trick and Sample space

We have constructed our Hamiltonian, which consists of a part for the topological insulator and another part for the effective coupling to the superconductor interfaces. The primary focus here is to calculate the average Josephson current and its fluctuations in our

STIS system. In a Josephson junction, a passage of current through it results in a phase difference ϕ between the two superconducting leads, represented by Δ_1 and Δ_2 . In our case, we consider two samples of STIS junctions. Therefore, for the current fluctuations, we expect them to depend on two distinct phases, ϕ_1 and ϕ_2 , each corresponding to the phase difference in the respective leads.

To calculate these current fluctuations, we can utilize the fact that the supercurrent in a Josephson junction is a thermodynamic current, obtained by differentiating a thermodynamic potential. Consequently, the average supercurrent can be expressed as follows:

$$I(\phi) = -2e \frac{d\langle F \rangle_V}{d\phi} \quad (4.19)$$

where $F = -T \ln Z$ is the free energy and $\langle \dots \rangle_V$ represents an average over disorder, considering the given free energy. The partition function is

$$Z = \int D[\bar{\psi}\psi] e^{-S(\bar{\psi}, \psi, V_{dis})}. \quad (4.20)$$

The disorder will be taken into account later. To account for the sample-to-sample fluctuations in the Josephson current, we introduce the correlator:

$$var I(\phi_1, \phi_2) = K(\phi_1, \phi_2) = \langle I(\phi_1) I(\phi_2) \rangle_c \quad (4.21)$$

where $\langle AB \rangle_c = \langle AB \rangle - \langle A \rangle \langle B \rangle$, and $\langle \dots \rangle$ is an average over the ensemble. This will give explicitly at the end

$$K(\phi_1, \phi_2) = 4e^2 \frac{d^2 \langle F(\phi_1) F(\phi_2) \rangle_c}{d\phi_1 d\phi_2}. \quad (4.22)$$

In order to proceed with this approach, we need to double the sample space to accommodate the states of the two systems. This leads to the following transformations:

$$\hat{H} \longrightarrow \hat{\mathcal{H}}(\phi_1, \phi_2) \equiv \text{diag} \left(\hat{H}(\phi_1), \hat{H}(\phi_2) \right) \quad (4.23)$$

$$\hat{\epsilon} \longrightarrow \hat{\epsilon} \equiv \epsilon \otimes \mathbb{I}_2. \quad (4.24)$$

We admit that the Mastubara energies ϵ_n forms a n-dimensional diagonal matrix, such that $(\hat{\epsilon})_n = \epsilon_n$. To address the disorder, we employ the Replica Trick as described in Edwards' work [58]. We create R replicas of the same system, using the same generating

function, and subsequently take the limit as R approaches 0. The generating function, or partition function, is raised to the power of R . This allows the disorder to contribute linearly in the exponent, making it easier to handle analytically. In summary, an average value of an observable calculated from the generating function Z with sources J gives:

$$F = -\beta \lim_{R \rightarrow 0} \frac{1}{R} (e^{R \ln Z} - 1) = -\beta \lim_{R \rightarrow 0} \frac{1}{R} Z^R. \quad (4.25)$$

Where it was introduced the idea of R equal replicas of Z in the limit where $R \rightarrow 0$. The replicated partition function can be seen as

$$Z^R = \int D[\bar{\psi}\psi] e^{-S(\bar{\psi}, \psi, V_{dis})} \quad (4.26)$$

$$S(\bar{\psi}, \psi, V_{dis}) = \sum_{r=1,2} \int d\mathbf{x} \bar{\psi}^r \left(-i\hat{\epsilon} + \hat{\mathcal{H}}(\phi_1, \phi_2) - \mu\sigma_3^{ph} \otimes \mathbb{I} \right) \psi^r. \quad (4.27)$$

In our case $\bar{\psi}, \psi$ are $4 \times (R_1 + R_2)$ dimensional fields, where the factor of 4 accounts for the particle-hole and spin degrees of freedom.

4.3 Disorder Average

By performing an average over disorder, assuming that $\langle V(\mathbf{r})V(\mathbf{r}') \rangle = \frac{1}{2\pi\nu_0\tau} \delta(\mathbf{r} - \mathbf{r}')$, we find that the only affected term is the one involving the disorder potential,

$$\langle e^{\int d\mathbf{r} \bar{\psi} V(\mathbf{r}) \sigma_3^{ph} \psi} \rangle_{dis} = e^{\frac{1}{4\pi\nu_0\tau} \int d\mathbf{r} \bar{\psi} \sigma_3^{ph} \psi \bar{\psi} \sigma_3^{ph} \psi}. \quad (4.28)$$

Considering the Grassmann field interaction, we can identify three types of scattering diagrams: Exchange, Cooper, and Direct channels. However, in our analysis, we will disregard the direct channel since it can be seen, in fluctuations calculations that it behaves like an effective chemical potential. The presence of the three channels can be explicitly observed by performing a Fourier transformation on the previously averaged action. The Fourier transformation yields exponential factors on \mathbf{k}_i , leading to a delta function, such that:

$$\sum_{\mathbf{k}_1 \mathbf{k}_2 \mathbf{k}_3 \mathbf{k}_4} \int d\mathbf{r} \bar{\psi}_{\mathbf{k}_1} \sigma_3^{ph} \psi_{\mathbf{k}_2} \bar{\psi}_{\mathbf{k}_3} \sigma_3^{ph} \psi_{\mathbf{k}_4} \delta_{\mathbf{k}_1 - \mathbf{k}_2 + \mathbf{k}_3 - \mathbf{k}_4}. \quad (4.29)$$

Specifically, there are three combinations of interactions at zero momentum sum:

$$\sum_{\mathbf{k}_1 \mathbf{k}_2 \mathbf{k}_3 \mathbf{k}_4} \int d\mathbf{r} \left(\bar{\psi}_{\mathbf{k}_1} \sigma_3^{ph} \psi_{\mathbf{k}_2} \bar{\psi}_{\mathbf{k}_2+\mathbf{q}} \sigma_3^{ph} \psi_{\mathbf{k}_1+\mathbf{q}} + \bar{\psi}_{\mathbf{k}_1} \sigma_3^{ph} \psi_{\mathbf{k}_2} \bar{\psi}_{-\mathbf{k}_1-\mathbf{q}} \sigma_3^{ph} \psi_{-\mathbf{k}_2-\mathbf{q}} + \right. \quad (4.30)$$

$$\left. + \bar{\psi}_{\mathbf{k}_1} \sigma_3^{ph} \psi_{\mathbf{k}_1+\mathbf{q}} \bar{\psi}_{\mathbf{k}_2+\mathbf{q}} \sigma_3^{ph} \psi_{\mathbf{k}_2} \right). \quad (4.31)$$

Respectively, the three terms are known as the Exchange, Cooper, and Direct channels. Now, utilizing the relation (4.7) and considering the symmetry of ψ and fermion anticommutativity, we can rewrite the expression as follows:

$$\bar{\psi}_{-\mathbf{k}_1-\mathbf{q}} \sigma_3^{ph} \psi_{-\mathbf{k}_2-\mathbf{q}} = -\psi_{-\mathbf{k}_2-\mathbf{q}}^t \sigma_3^{ph} \bar{\psi}_{-\mathbf{k}_1-\mathbf{q}}^t \quad (4.32)$$

$$= -\bar{\psi}_{\mathbf{k}_2+\mathbf{q}} (i\sigma_2^{ph}) \sigma_3^{ph} (i\sigma_2^{ph}) \psi_{\mathbf{k}_1+\mathbf{q}}^t \quad (4.33)$$

$$= \bar{\psi}_{\mathbf{k}_2+\mathbf{q}} \sigma_3^{ph} \psi_{\mathbf{k}_1+\mathbf{q}}. \quad (4.34)$$

From this observation, we can see that both the Exchange and Cooper channels are equivalent within this symmetry structure. Additionally, considering the complex conjugation, we can interpret this as two low momentum interactions involving $\sigma_3^{ph} \psi_{\mathbf{k}_1+\mathbf{q}} \bar{\psi}_{\mathbf{k}_1+\mathbf{q}}$ with momentum transfer $-\mathbf{q}$. Thus, we have:

$$\int d\mathbf{r} \bar{\psi} \sigma_3^{ph} \psi \bar{\psi} \sigma_3^{ph} \psi = -2 \int d\mathbf{r} \text{tr} \left(\sigma_3^{ph} \psi \bar{\psi} \sigma_3^{ph} \psi \bar{\psi} \right), \quad (4.35)$$

Where the trace arises from the summation over momenta, the factor of -2 accounts for the summation of both scattering channels and the anti-commutation, and the summation is limited to low momentum $-\mathbf{q}$. It is important to note that this expression represents only the disorder term of the total action.

To further investigate these disorder channels, we perform a Hubbard-Stratonovich field transformation. First, we multiply this expression by the fat unity $1 = \int DQ e^{-\frac{\pi\nu_0}{2r} \int d\mathbf{r} \text{tr}(Q^2)}$, where Q is a bosonic field and a normalization constant has been absorbed into DQ . Then, we transform $Q \rightarrow Q + i\sigma_3^{ph} \psi \bar{\psi} (\pi\nu_0)^{-1}$ using the property of invariance of the Gaussian integral under translations. This is a technique that helps us to decouple the quartic interaction into an auxiliary field Q . It is important to note that the first expression has

a hidden negative sign in its usual structure:

$$\begin{aligned}
e^{-\frac{1}{2\pi\nu_0\tau} \int d\mathbf{r} \operatorname{tr}(\sigma_3^{ph} \psi \bar{\psi} \sigma_3^{ph} \psi \bar{\psi})} &= e^{-\frac{1}{2\pi\nu_0\tau} \int d\mathbf{r} \operatorname{tr}(\sigma_3^{ph} \psi \bar{\psi} \sigma_3^{ph} \psi \bar{\psi})} \times \int DQ e^{-\frac{\pi\nu_0}{2\tau} \int d\mathbf{r} \operatorname{tr} Q^2} \\
&= e^{-\frac{1}{2\pi\nu_0\tau} \int d\mathbf{r} \operatorname{tr}(\sigma_3^{ph} \psi \bar{\psi} \sigma_3^{ph} \psi \bar{\psi})} \times \int DQ e^{-\frac{\pi\nu_0}{2\tau} \int d\mathbf{r} \operatorname{tr} \left(Q^2 + iQ \sigma_3^{ph} \frac{\psi \bar{\psi}}{\pi\nu_0} + i\sigma_3^{ph} \frac{\psi \bar{\psi}}{\pi\nu_0} Q - \sigma_3^{ph} \psi \bar{\psi} \sigma_3^{ph} \psi \bar{\psi} \right)} \\
&= \int DQ e^{-\left(\frac{\pi\nu_0}{8\tau} \operatorname{Tr} Q^2 - \frac{i}{2\tau} \bar{\psi} Q \sigma_3^{ph} \psi \right)}. \tag{4.36}
\end{aligned}$$

In this procedure, we utilized the property of the cyclic product in a trace and the fact that $\operatorname{tr}(Q\psi\bar{\psi}) = -\bar{\psi}Q\psi$ for the Grassmann variables. Now, our averaged generating function becomes:

$$\langle Z^R \rangle_V = \int DQ e^{-S(Q)}, \quad S(Q) = \frac{\pi\nu_0}{8\tau} \operatorname{Tr} Q^2 - \frac{1}{2} \operatorname{Tr} \ln(G_Q^{-1}), \tag{4.37}$$

where

$$G_Q^{-1} = \left(i\hat{\epsilon} - v\mathbf{k} \cdot \sigma \sigma_3^{ph} + \mu \sigma_3^{ph} \otimes \mathbb{I} - \hat{H}_\Gamma(\phi_1, \phi_2) \right) + \frac{i}{2\tau} Q \sigma_3^{ph}. \tag{4.38}$$

This matrix of the bosonic field Q , in this new formalism, exhibits the following symmetry relation:

$$\begin{aligned}
\operatorname{Tr} \left(Q \sigma_3^{ph} \psi \otimes \bar{\psi} \right) &= \operatorname{Tr} \left(Q \sigma_3^{ph} \psi \otimes \bar{\psi} \right)^t \\
&= - \left(\psi^t \otimes \bar{\psi}^t \sigma_3^{ph} Q^t \right) \\
&= - \left((i\sigma_2^s \otimes i\sigma_2^{ph}) \psi \otimes \bar{\psi} (i\sigma_2^s \otimes i\sigma_2^{ph}) \sigma_3^{ph} Q^t \right) \\
&= - \left((i\sigma_2^s \otimes i\sigma_2^{ph}) \sigma_3^{ph} Q^t (i\sigma_2^s \otimes i\sigma_2^{ph}) \psi \otimes \bar{\psi} \right) \\
&= \left((i\sigma_2^s \otimes i\sigma_2^{ph}) \sigma_3^{ph} Q^t \sigma_3^{ph} (i\sigma_2^s \otimes i\sigma_2^{ph}) \sigma_3^{ph} \psi \otimes \bar{\psi} \right) \\
&= - \left((\sigma_2^s \otimes \sigma_1^{ph}) Q^t (\sigma_2^s \otimes \sigma_1^{ph}) \sigma_3^{ph} \psi \otimes \bar{\psi} \right). \tag{4.39}
\end{aligned}$$

Then, by comparing with the left hand side, we find that $Q = -\sigma_2^s \sigma_1^{ph} Q^t \sigma_1^{ph} \sigma_2^s$. This result is obtained by utilizing the relation (4.7), the anti-commutation relations of Grassmann variables, and the cyclic properties of the trace.

4.4 Saddle Point Equation

Following this action, we now seek an extremal point of the action (4.37). By performing a variation of the action with respect to Q and requiring the linear contributions in δQ

to vanish, we obtain the following equation:

$$\begin{aligned}
Q_0 &= \frac{i}{\pi\nu_0} \sum_{\mathbf{k}} G_Q(\mathbf{k}) \\
&= \frac{i}{\pi\nu_0} \sum_{\mathbf{k}} \frac{1}{-v\mathbf{k}\cdot\sigma^s + \mu + \frac{i}{2\tau}Q} \\
&= \frac{i}{\pi\nu_0} \sum_{\mathbf{k}} \frac{v\mathbf{k}\cdot\sigma^s + \mu + \frac{i}{2\tau}Q_0}{-v^2\mathbf{k}^2 + \mu^2 - \frac{1}{4\tau^2} + \frac{i\mu}{2\tau}Q_0}.
\end{aligned} \tag{4.40}$$

Above, we multiplied and divided by a term to simplify the denominator and allow our saddle point equation to resemble a self-energy equation, akin to a Dyson equation. We assumed that $\{\Delta, E_t, \epsilon\} \ll \frac{1}{\tau}$, which represents the largest energy scale. By taking the integral above, we can expect that the elements of Q_0 will take values of ± 1 . The disorder average preserves causality of the Green's functions, so the signs of the diagonal elements of Q_0 should coincide with the imaginary part of the energy. With these considerations and the chosen form of the Nambu spinors, a simple solution for Q_0 can be given as:

$$Q_0 = \sigma_3^{ph} \otimes \mathbb{I}_2^s \otimes \mathbb{I}_2^f \otimes \mathbb{I}_R. \tag{4.41}$$

In the limit of small frequencies, the action exhibits a symmetry under transformations of the form $T = (i\sigma_2^{ph})T^t(i\sigma_2^{ph})^{-1}$, with $T = \exp(W/2)$, where W is a generator of rotations, as derived from equation (4.7). This symmetry implies the presence of long-range low-energy excitations, or soft modes, as discussed in reference [59]. These soft modes correspond to fluctuations around the saddle point solution. Here, T represents a real pseudo-unitary rotation matrix. Consequently, any configuration of Q of the form $Q = TQ_0T^{-1}$ is a solution to the saddle point equation, as it preserves this symmetry. Deviations from this form of Q would break the symmetry.

4.5 Gradient Expansion

From this equation, we expand and rewrite the Green's function as follows:

$$\begin{aligned}
Tr \ln(G_Q^{-1}) &= Tr \left(i\hat{\epsilon} - [v\mathbf{k} \cdot \sigma^s - \mu] \sigma_3^{ph} - \hat{H}_\Gamma(\phi_1, \phi_2) + \frac{i}{2\tau} T \sigma_3^{ph} T^{-1} \sigma_3^{ph} \right) \\
&= Tr(i\hat{\epsilon} \sigma_3^{ph} - v\mathbf{k} \cdot \sigma^s + \mu - \hat{H}_\Gamma(\phi_1, \phi_2) \sigma_3^{ph} + \frac{i}{2\tau} T \sigma_3^{ph} T^{-1}) \\
&= Tr \ln(G_Q^{-1}) = Tr(T^{-1} [i\hat{\epsilon} \sigma_3^{ph} - v\mathbf{k} \cdot \sigma^s + \mu - \hat{H}_\Gamma(\phi_1, \phi_2) \sigma_3^{ph}] T + \frac{i}{2\tau} \sigma_3^{ph}).
\end{aligned} \tag{4.42}$$

This expression should be understood as the most general representation that encompasses the significant physical transformations T satisfying the symmetry constraints. It accounts for all possible solutions in the vicinity of the saddle point. Next, we introduce a commutation relation to construct a more convenient expression:

$$\begin{aligned}
Tr \ln(G_Q^{-1}) &= Tr \ln(T^{-1} [i\hat{\epsilon} \sigma_3^{ph} + T[v\mathbf{k} \cdot \sigma^s, T^{-1}] - \hat{H}_\Gamma \sigma_3^{ph}] T - v\mathbf{k} \cdot \sigma^s + \mu + \frac{i}{2\tau} \sigma_3^{ph}) \\
&\approx Tr \ln(1 - G_0 \mathcal{O}_T),
\end{aligned} \tag{4.43}$$

where we dropped the ϕ dependence for simplicity and defined

$$G_0 = \left(-v\mathbf{k} \cdot \sigma^s + \mu + \frac{i}{2\tau} Q_0 \right)^{-1} = \frac{v\mathbf{k} \cdot \sigma^s + \mu + \frac{i}{2\tau} Q_0}{-v^2 \mathbf{k}^2 + (\mu + \frac{i}{2\tau} Q_0)^2} \tag{4.44}$$

and

$$\mathcal{O}_T = T^{-1} [-i\hat{\epsilon} \sigma_3^{ph} - T[v\mathbf{k} \cdot \sigma^s, T^{-1}] + \hat{H}_\Gamma \sigma_3^{ph}] T. \tag{4.45}$$

With this, we can introduce the effective action to be expanded, taking into account that the T transformation generates small variations around the saddle point.

$$\begin{aligned}
S_{eff} &= -\frac{1}{2} Tr \ln(G_Q^{-1}) \\
&= -\frac{1}{2} Tr \ln(G_0^{-1} - \mathcal{O}_T) \\
&= const - \frac{1}{2} Tr \ln(1 - G_0 \mathcal{O}_T) \\
&\approx \frac{1}{2} Tr(G_0 \mathcal{O}_T) + \frac{1}{4} Tr(G_0 \mathcal{O}_T G_0 \mathcal{O}_T).
\end{aligned} \tag{4.46}$$

After some calculations, explicitly developed in Appendix A, we have for our action

$$S = \frac{\pi\nu}{2} \int d\mathbf{r} \text{Tr} \left(\frac{D}{4} (\partial_{\mathbf{r}} - i[\mathbf{A}, \cdot])Q(\partial_{\mathbf{r}} - i[\mathbf{A}, \cdot])Q - \hat{\epsilon}Q\sigma_3^{ph} - i\hat{H}_{\Gamma}\sigma_3^{ph}Q \right). \quad (4.47)$$

4.6 Usadel Equation

From this action, we can expect three types of terms arising from the dynamical part of it. One term involves only derivatives, another term involves both derivatives and the vector potential, and the third term involves only the vector potential contribution. To gain a better understanding, we can perform a second saddle point analysis as before. We look for a stationary configuration in the presence of weak spatial and temporal gradients, that is, fluctuations around the saddle point. We expect then to transformate Q as $T^{-1}QT$, , where W is the matrix generator of rotations for $T = \exp(W/2)$. Expanding to first order in W we get that our transformation is $Q \mapsto Q' - \frac{1}{2}[W, Q']$. Substituting the new Q in the action (4.47) and imposing the linear W terms to vanish, we get:

$$D \left(\partial_{\mathbf{x}}Q' \partial_{\mathbf{x}}Q' - 4i\mathbf{A}Q\partial_{\mathbf{x}}Q' - 2\mathbf{A}Q' \mathbf{A}Q' \right) - 2[\hat{\epsilon}\sigma_3^{ph} + i\hat{H}_{\Gamma}\sigma_3^{ph}, Q'] = 0. \quad (4.48)$$

From this action, we can expect three types of terms arising from the dynamical part of it. One term involves only derivatives, another term involves both derivatives and the vector potential, and the third term involves only the vector potential contribution. To gain a better understanding, we can perform a second saddle point analysis as before. We look for a stationary configuration in the presence of weak spatial and temporal gradients, that is, fluctuations around the saddle point. We expect then to transformate Q as $T^{-1}QT$, , where W is the matrix generator of rotations for $T = \exp(W/2)$. Expanding to first order in W we get that our transformation is $Q \mapsto Q' - \frac{1}{2}[W, Q']$. Substituting the new Q in the action (4.47) and imposing the linear W terms to vanish, we get:

$$[D\mathbf{A}Q' \mathbf{A} - 2\hat{\epsilon}\sigma_3^{ph} - 2i\hat{H}_{\Gamma}\sigma_3^{ph}, Q'] = 0. \quad (4.49)$$

We assume for \mathbf{A} , with a particle-hole symmetry, $\mathbf{A} = \sigma_3^{ph} \frac{n_{\phi}}{\tau} \mathbf{e}_y = \sigma_3^{ph} E_{\phi} \mathbf{e}_y$, where $n_{\phi} = \frac{LB}{\phi_0} = \frac{\phi}{\phi_0}$ represents the number of flux quanta in an area LB , and ϕ_0 is the flux quantum.

This choice of \mathbf{A} results in a constant magnetic field in the z direction, given by $B = \nabla \times \mathbf{A}$:

$$\left[D \left(\frac{n_\phi}{\tau} \right)^2 \sigma_3^{ph} Q' \sigma_3^{ph} - 2\hat{\epsilon} \sigma_3^{ph} - 2i\hat{H}_\Gamma \sigma_3^{ph}, Q' \right] = 0, \quad (4.50)$$

which can be conveniently rewritten as

$$0 = \left[D \left(\frac{n_\phi}{\tau} \right)^2 Q_\perp - \hat{v}_i \sigma_i^{ph}, Q' \right] \quad (4.51)$$

$$\hat{v}_3 = \hat{\epsilon} \tau + \frac{2E_t \tau}{\sqrt{\hat{\epsilon}^2 + \Delta^2}} \hat{\epsilon}, \quad \hat{v}_2 = -\frac{2E_t \tau}{\sqrt{\hat{\epsilon}^2 + \Delta^2}} \Delta \cos(\hat{\phi}), \quad (4.52)$$

where $Q_\perp = \sigma_3^{ph} Q' \sigma_3^{ph} - Q$. Due to translational invariance parallel to the interfaces, we further restrict ourselves to matrices Q that are independent of the y coordinate. We make the ansatz $\hat{Q}' = \hat{m}_i \sigma_i^{ph}$ and substitute it into the Usadel equation. Using the relation $[\mathbf{a} \cdot \sigma, \mathbf{b} \cdot \sigma] = (\mathbf{a} \times \mathbf{b}) \cdot \sigma$, we can derive a geometric statement, from the Usadel equation just written,

$$\left(D \left(\frac{n_\phi}{\tau} \right) m_3 + \mathbf{v} \right) \times \mathbf{m} = 0. \quad (4.53)$$

The cases to be considered here are the limiting cases where there is no magnetic field and where it is strong. First, in the case where there is no magnetic field, we have the following Usadel equation:

$$0 = [\hat{v}_i \sigma_i^{ph}, Q']. \quad (4.54)$$

Such a structure has a solution for \mathbf{m} that is parallel to \mathbf{v}

$$\mathbf{m} = \mathbf{n} = \mathbf{v}/v, \quad v = \sqrt{v_2^2 + v_3^2}. \quad (4.55)$$

For a finite strong magnetic field, we return to equation (4.53) and perform the cross product to obtain a relation between the components of the vector \mathbf{m}

$$m_3(v_2 - D \left(\frac{n_\phi}{\tau} \right) m_2) = v_3 m_2. \quad (4.56)$$

For $m_2 \neq 0$ it can be stated that

$$\mathbf{m} = \begin{pmatrix} 0 \\ m_2 \\ \frac{v_3 m_2}{v_2 - D\left(\frac{n_\phi}{\tau}\right) m_2} \end{pmatrix}, \quad (4.57)$$

where, using the normalization relation $\mathbf{m}^2 = 1$ we can solve as a function of m_2 as variable, then

$$\begin{aligned} v_3^2 m_2^2 &= (m_2^2 - 1) \left(v_2 - D\left(\frac{n_\phi}{\tau}\right) m_2 \right)^2, \\ s^2 \beta^2 m_2^2 &= (s - m_2)^2 (m_2^2 - 1), \end{aligned} \quad (4.58)$$

where $s = v_2 / D\left(\frac{n_\phi}{\tau}\right)$ and $\beta = v_3 / v_2$. These redefinition help us to propose a power series solution for m_2 for strong magnetic fields that can be understood physically. For s as the series parameter

$$m_2(s) = \sum_{l=0}^{\infty} m_{2,l} s^l, \quad (4.59)$$

where the leading contribution of this series is

$$m_2(s) = \frac{s}{1 + |\beta|s}, \quad m_3(s) = m_3 = 1. \quad (4.60)$$

In constructing this solution, we treated the product $s\beta$ in equation (4.58) as an independent parameter. The strong magnetic field limit requires that s is small, as it is independent of the parameters in v_2 . However, when calculating the current fluctuations, we need to consider the solution over a wide range of frequency ϵ . The parameter β , on the other hand, depends on frequency according to the definitions of v_i in equation (4.52), which means that the product $s\beta$ is not necessarily small. Nevertheless, we have numerically confirmed that the above-mentioned solution provides an excellent approximation over a broad range of β values as long as $s < 0.5$.

4.7 Rotation of the Q-field

To calculate the current fluctuations, we need to go beyond the saddle point approximation and consider fluctuations around it. This can be achieved by introducing fluctuations around the saddle point solution. In order to incorporate these fluctuations, it is convenient to express the second saddle point solution as a rotation from the first one,

$$Q_\Delta = T_\Delta Q_0 T_\Delta^{-1}. \quad (4.61)$$

We need to introduce fluctuations on this Q_Δ field, then we use the rotation of the fluctuation transformation T , $\tilde{T} = T_\Delta T T_\Delta^{-1}$, such that

$$Q' = \tilde{T} Q_\Delta \tilde{T}^{-1} = T_\Delta Q T_\Delta^{-1}, \quad (4.62)$$

where $Q = T Q_0 T^{-1}$. Substituting this rotated Q' field into the action (4.47)

$$S = \frac{\pi\nu}{2} \int d\mathbf{r} \text{Tr} \left(\frac{D}{4} (\partial_{\mathbf{r}} - i[\mathbf{A}, \cdot]) T_\Delta Q T_\Delta^{-1} (\partial_{\mathbf{r}} - i[\mathbf{A}, \cdot]) T_\Delta Q T_\Delta^{-1} - v_i \sigma_i^{ph} \times T_\Delta Q T_\Delta^{-1} \right). \quad (4.63)$$

Then, with the cyclic invariance of the trace we eliminate T_Δ in the action and arrive at

$$S = \frac{\pi\nu}{2} \int d\mathbf{r} \text{Tr} \left(\frac{D}{4} (\partial_{\mathbf{r}} - i[\mathbf{A}, \cdot]) Q (\partial_{\mathbf{r}} - i[\mathbf{A}, \cdot]) Q - v_i \sigma_i^{ph'} Q \right), \quad (4.64)$$

where $\sigma_i^{ph'} = T_\Delta^{-1} \sigma_i^{ph} T_\Delta$, is a transformed Pauli matrix.

4.8 Density of States

With the solution of the Usadel equation at hand, we can now study the influence of the magnetic field on the proximity induced minigap in the TI film. To this end, we first recall that within the field theory approach the density of states (DoS) follows from

$$\frac{\nu(\epsilon)}{\nu} = \frac{1}{4} \text{Re} \left[\text{tr} \left(Q_0(\epsilon \rightarrow -i\epsilon_+) \sigma_3^{ph} \right) \right], \quad (4.65)$$

where Q_0 is the solution of the Usadel equation analytically continued from the discrete set of Matsubara frequencies to the axis of real frequencies, where $\epsilon_+ = \epsilon + i\eta$ includes

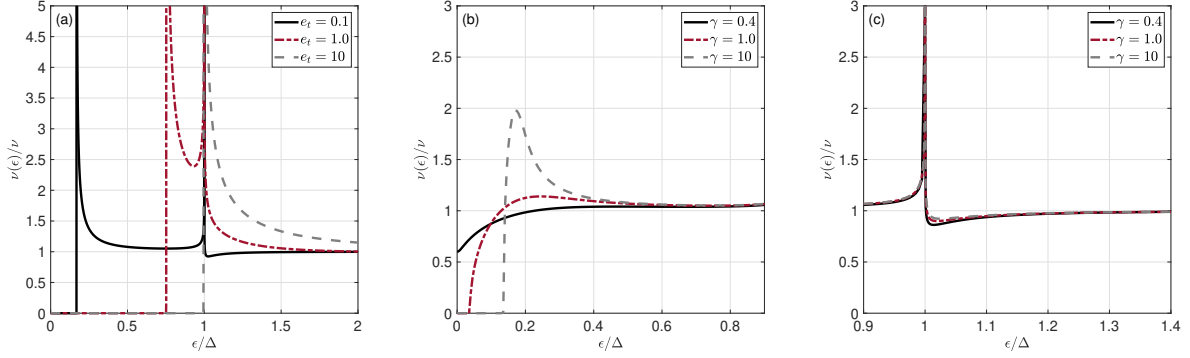


Figure 4.2: (a) Density of states $\nu(\epsilon)$ for the vanishing magnetic field normalized to the density of states $\nu = \nu(\mu)$ in the absence of superconducting leads for different values of $e_t = E_t/\Delta = 0.1, 1, 10$. Panels (b) and (c) show density of states of the microbridge at a finite magnetic field as a function of frequency ϵ for different values of $\gamma = E_t/E_\Phi = (0.1/0.01, 0.1/0.1, 0.1/0.25)$ and fixed phase $\phi = 0$, where $e_\Phi = E_\Phi/\Delta$.

a positive small imaginary part, and ν denotes the density of states at energy $\epsilon = \mu$ in absence of superconducting leads. Building then on the discussion of the previous section, the DoS reads

$$\nu(\epsilon) = \nu \text{Re} [m_3(-i\epsilon_+)], \quad (4.66)$$

with m_3 specified through Eqs. (4.57) and (4.58). We first consider the DoS in absence of a magnetic field, $B = 0$, as shown in Figure 4.2(a), and recall that the proximity induced minigap E_g is a function of the ratio E_t/Δ . For the weak coupling limit, $E_t \ll \Delta$, it displays the typical superconductor square-root singularity above the minigap $E_g = 2E_t \cos \phi$, $\nu(\epsilon) \sim \theta(\epsilon - E_g)(|\epsilon - E_g|)^{1/2}$, and a weaker singularity $\nu(\epsilon) \sim 1/(|\epsilon - \Delta|)^{1/4}$ around the superconducting gap. In the opposite strong-coupling limit, $\Delta \ll E_t$, there is only a single singularity above the superconducting gap with $E_g \sim \Delta$. In the intermediate case $E_t = \Delta$ we observe two singularities, as for $E_t/\Delta \ll 1$, but now the minigap becomes large $E_g \lesssim \Delta$, as for the case $E_t \gg \Delta$.

Turning on finite magnetic fields, we focus on the limit $E_t/\Delta \ll 1$. In this limit, we can explore the sensitivity of the minigap E_g to the magnetic field while its pair-breaking effect on the superconducting leads is still negligible. Figure 4.2(b) shows the DoS for $E_t \ll \Delta$ and various values of E_Φ . Increasing the magnetic field from $B = 0$, the minigap continuously reduces and closes once $E_\Phi \gtrsim E_g$. At the same time, the square root singularity at E_g is smoothed out and turns into a monotonic function which displays

behavior qualitatively similar to that found in the Abrikosov-Gor'kov theory of gapless superconductivity [60]. Once the gap closes, the DoS quickly evolves into the nearly constant function $\nu(\epsilon)$. As expected, the singularity at $\epsilon \sim \Delta$ is hardly affected by small magnetic fields $E_\Phi \ll \Delta$, see the right panel of Fig 4.2(c). We observe, however, a small dip above the singularity $\epsilon \gtrsim \Delta$ that develops and becomes more pronounced for smaller values of γ . It should be stressed that the sub- and above the gap features in the DoS are extremely sensitive to the boundary action used in the saddle point analysis of Usadel equation. For instance, in the model of transparent interfaces, that can be captured by the full circuit-theory action [61], the DoS in the sub-gap region may display secondary gaps [62, 63, 64], while a singularity at Δ may be turned into a vanishing DoS and an unusual structure of the crossover to higher energies arises [65, 66].

Notice that above results were derived using the analytical solution of Equation (4.58). The latter is a rather cumbersome expression and therefore not stated here. Although the mean field solution obtained via power series provides a good approximation for the full-fledged solution, in both limiting cases, strong and weak magnetic field, it fails to fully capture the structure of the minigap. In the weak magnetic field limit, $E_\Phi < E_t$, it overestimates the size of the minigap and there is a singularity in the region $\epsilon < \Delta$. In the opposite limit, $E_\Phi > E_t$, there exists a threshold value E_Φ^* beyond which the minigap closes. The approximated mean field solution fails to reproduce this behavior and always results in a gapless density of states. It is also worth stating that the mean-field analysis of DoS presented in this section misses the sub-gap tails [67, 68, 69, 70, 71, 72] and zero-bias peaks. The latter include disorder-induced class D peak [73] and Majorana peak [74]. These fine-structure features of the DoS appear at the level of nonperturbative analysis of Q -matrix manifold and become resolved at the energy scales of level spacing. This parameter regime is beyond the domain of our assumptions that $1/\nu \ll \{E_t, E_\Phi, \Delta\} \ll \{E_{Th}, 1/\tau\}$, with E_{Th} the Thouless energy, to be more detailed later. The results of this section are amenable to scanning-tunneling probes in hybrid S-TI proximity circuits and hetero-structures, see e.g. Refs. [75, 76, 77, 78, 79].

4.9 Introducing fluctuations around the saddle point

Now we aim to calculate the Gaussian fluctuations of our field Q . This can be done by expanding Q in terms of its generators as $Q = e^W Q_0 = \left(\mathbb{I} + W + \frac{W^2}{2}\right) Q_0$. Since we are interested only in terms of second order in W , we can neglect higher order terms. It is important to consider the particle-hole structure of the action and take into account the relation $[W, \sigma_3^{ph}]_+ = 0$. Furthermore, note that W will have a diagonal of zeros. Therefore, our action takes the following form:

$$S = \frac{\pi\nu}{2} \int d\mathbf{x} \text{Tr} \left(\frac{D}{4} (\partial_y - i[\sigma_3^{ph} E_\phi, \cdot]) \left(\mathbb{I} + W + \frac{W^2}{2} \right) Q_0 (\partial_y - i[\sigma_3^{ph} E_\phi, \cdot]) \times \right. \\ \left. \times \left(\mathbb{I} + W + \frac{W^2}{2} \right) Q_0 - v_i \sigma_i^{ph'} \left(\mathbb{I} + \frac{W^2}{2} \right) Q_0 \right). \quad (4.67)$$

From this lengthy equation, we need to extract the zeroth and second order terms of W . The zeroth order term is obtained as follows:

$$S_0 = \frac{\pi\nu A_s}{2} \text{Tr} \left(2De^2 E_\phi^2 m_2^2 - v_i m_i \right), \quad (4.68)$$

where we excluded all terms that give zero trace contribution, performed the trace over particle-hole space, resulting in a factor of two multiplying the equation, and carried out the integral over space, yielding an area A_s . The Q_0 factor was replaced by the ansatz for the Usadel equation solution, $Q_0 = m_i \sigma_i^{ph}$. Additionally, we used the cyclic permutation property of the trace. The next term is more complex to solve, but the same rules apply. In total, we will have four contributions.

$$S = \frac{\pi\nu}{2} \int d\mathbf{x} \text{Tr} \left((D[(\partial_y W)Q_0 + ieE_\phi[m_3, W]_+]^2 \right. \\ \left. + 2De^2 E_\phi^2 [(m_2 \sigma_1^{ph} W)^2 + m^2 W^2] - 2m_i v_i W^2 \right). \quad (4.69)$$

The first term in the square brackets arises from the multiplication of two first-order factors, while the second term comes from the squared W terms, and the last term comes from the last factor in the S action. We can derive this by utilizing the fact that $\partial_y Q_0 = 0$, $[W, Q_0]_+$, and the properties already employed for the S_0 action. Thus, we obtain an action that is convenient for studying sample-to-sample fluctuations. Now, let us examine the form of W to understand the modes acting on it. First, we have $Q_0 =$

$\sigma_3^{ph} \otimes \Lambda$, where Λ is a diagonal matrix in Matsubara space with elements $\Lambda_n = \text{sgn}(\epsilon_n)$, as other spatial domains have been traced out. Taking into account the energy scale contributions, we will focus on Diffuson (d) and Cooperon (c) modes. This distinction arises from considering the constraints between Q_0 and W , as well as the additional constraint $[W_d, \Lambda]_+ = 0$, $[W_d, \Lambda] = 0$. Hence, we can rewrite W as $W = W_d + W_c$, where

$$W = \begin{pmatrix} P_d & 0 \\ 0 & P_d^t \end{pmatrix}_{ph} + \begin{pmatrix} 0 & P_c \\ -P_c^* & 0 \end{pmatrix}_{ph}, \quad P_d^\dagger = -P_d, \quad P_c^t = P_c. \quad (4.70)$$

By combining all the constraints, we can determine the form of P_d and P_c , which are Matsubara matrices, as well as the values that Λ takes for each ϵ . The resulting expressions are given by:

$$P_d = \begin{pmatrix} 0 & d \\ d^\dagger & 0 \end{pmatrix}, \quad P_c = \begin{pmatrix} c & 0 \\ 0 & c^\dagger \end{pmatrix}. \quad (4.71)$$

W_d and W_c are diagonal and off-diagonal in particle-hole space, respectively, for the indices. Similarly, P_d and P_c are off-diagonal and diagonal in the Matsubara space. With these definitions, we can rewrite our action in a more convenient form as follows:

$$\begin{aligned} S &= L \int dy \frac{\pi\nu}{4} \text{Tr}[D(Q_0 \partial_y W - ieE_\phi[m_3, W]_+)^2 - 2v_i m_i W^2] + \\ &+ \frac{\pi\nu}{2} D e^2 E_\phi^2 \text{Tr}[(m_2 \sigma_1^{ph} W)^2 + m_2^2 W^2] \\ &= L \int dy - \frac{\pi\nu}{4} \text{Tr}[D(\partial_y W)^2 + 2(v_i m_i + D e^2 E_\phi^2 (m_3^2 - m_2^2)) W^2] \\ &- \frac{\pi\nu D}{2} e^2 E_\phi^2 \text{Tr}[m_3 W m_3 W - (m_2 \sigma_1^{ph} W m_2 \sigma_1^{ph} W)] \\ &- \frac{i\pi\nu D}{2} e E_\phi \text{Tr}[Q_0 \partial_y W [\sigma_3^{ph}, W]_+], \end{aligned} \quad (4.72)$$

where L is the length along the x direction of the junction integrated. Now, we apply $W = W_d + W_c$ with their respective internal structures to separate our action into two

different modes, corresponding to Diffusons and Cooperons:

$$\begin{aligned}
S_d = & L \int dy \pi\nu \text{Tr} [D\partial_y d^\dagger \partial_y d + d^\dagger [\hat{v}_i m_i, d]_+] + \pi\nu D e^2 \mathbf{A}_\phi^2 \text{Tr} [d^\dagger [m_3^2 - m_2^2, d]_+] \\
& + \pi\nu D e^2 \mathbf{A}_\phi^2 \text{Tr} [2m_3 d^\dagger m_3 d + m_2 P_D^t m_2 P_D] - \pi\nu i D e \mathbf{A}_\phi \text{Tr} \left(\partial_y d^\dagger [m_3, d]_+ - \partial_y d [m_3, d^\dagger]_+ \right),
\end{aligned} \tag{4.73}$$

$$\begin{aligned}
S_c = & L \int dy \frac{\pi\nu}{2} \text{Tr} [D\partial_y c_i^\dagger \partial_y c_i + c_i^\dagger [\hat{v}_i n_i^E, c_i]_+] + \frac{\pi\nu}{2} D e^2 \mathbf{A}_\phi^2 \text{Tr} [c_i^\dagger [m_3^2 - m_2^2, c_i]_+] \\
& + \frac{\pi\nu D}{2} e^2 \mathbf{A}_\phi^2 \text{Tr} [2m_3 c_1^\dagger m_3 c_1 + 2m_3 c_2^\dagger m_3 c_2 + m_2 c_1^\dagger m_2 c_1 + m_2 c_2^\dagger m_2 c_2 + m_2 c_1 m_2 c_1 + \\
& m_2 c_2 m_2 c_2] - \frac{\pi\nu i D}{2} e \mathbf{A}_\phi \text{Tr} \left(-\partial_y c_1 [m_3, c_1^\dagger]_+ + \partial_y c_2 [m_3, c_2^\dagger]_+ \right. \\
& \left. + \partial_y c_1^\dagger [m_3, c_1]_+ - \partial_y c_2^\dagger [m_3, c_2]_+ \right).
\end{aligned} \tag{4.74}$$

According to the physical process, the d -modes ϵ_1 and ϵ_2 have opposite signs, while for the Cooperon c -modes, the signs are the same. In the Matsubara space, where the parametrization is given by $\Lambda_n = \text{sgn}(\epsilon_n)$, we can write:

$$P_d(\epsilon_1, \epsilon_2) = d_{\epsilon_1, \epsilon_2} \theta_{\epsilon_1} \theta_{-\epsilon_2} - d_{\epsilon_1, \epsilon_2}^\dagger \theta_{-\epsilon_1} \theta_{\epsilon_2}, \quad P_c(\epsilon_1, \epsilon_2) = c_{\epsilon_1, \epsilon_2} \theta_{\epsilon_1} \theta_{\epsilon_2} + c_{-\epsilon_1, -\epsilon_2}^t \theta_{-\epsilon_1} \theta_{-\epsilon_2}, \tag{4.75}$$

the sign coming from the complex conjugation in momentum representation of the functions. Following this construction, the right-hand side should be seen with matrix indices a and b for ϵ_1 and ϵ_2 , respectively, in the Matsubara space,

$$\begin{aligned}
S_d = & \pi\nu L \left\{ D \left| \left[\partial_y - \frac{ie\mathbf{E}_\phi}{2} (m_3^a(\epsilon_1) + m_3^b(\epsilon_2)) \right] d_\alpha \right|^2 + \left| \left[\hat{v}_i^a(\epsilon_1) m_i^a(\epsilon_1) + \hat{v}_i^b(\epsilon_2) m_i^b(\epsilon_2) \right] d_\alpha \right|^2 \right. \\
& + \frac{e^2 \mathbf{E}_\phi^2}{4} \left| m_3^a(\epsilon_1) + m_3^b(\epsilon_2) \right|^2 |d_\alpha|^2 + \\
& \left. - e^2 \mathbf{E}_\phi^2 \left[m_2^a(\epsilon_1)^2 + m_2^b(\epsilon_2)^2 \right] |d_\alpha|^2 - 2e^2 \mathbf{E}_\phi^2 \left[m_2^a(\epsilon_1) m_2^b(\epsilon_2) \right] \text{Re} [d_\alpha^* d_{\bar{\alpha}}] \right\},
\end{aligned} \tag{4.76}$$

$$\begin{aligned}
S_c = & \pi\nu L \left\{ D \left| \left[\partial_y - \frac{ie\mathbf{E}_\phi}{2} (m_3^a(\epsilon_1) + m_3^b(\epsilon_2)) \right] c_\alpha \right|^2 + \left| \left[\hat{v}_i^a(\epsilon_1) m_i^a(\epsilon_1) + \hat{v}_i^b(\epsilon_2) m_i^b(\epsilon_2) \right] c_\alpha \right|^2 \right. \\
& + \frac{e^2 \mathbf{E}_\phi^2}{4} \left| m_3^a(\epsilon_1) + m_3^b(\epsilon_2) \right|^2 |c_\alpha|^2 + \\
& \left. - e^2 \mathbf{E}_\phi^2 \left[(m_2^a(\epsilon_1))^2 + (m_2^b(\epsilon_2))^2 \right] |c_\alpha|^2 + 2e^2 \mathbf{E}_\phi^2 \left[m_2^a(\epsilon_1) m_2^b(\epsilon_2) \right] \text{Re} [c_\alpha c_\alpha^t] \right\},
\end{aligned} \tag{4.77}$$

where $\alpha = \epsilon_1, \epsilon_2, ab, mn$ and $\bar{\alpha} = -\epsilon_1, -\epsilon_2, ab, mn$. Here m, n are Replica indices.

4.9.1 Eigenvalues

To calculate the eigenvalues of the matrix action, we can focus on solving it for either S_c or S_d since they have the same mathematical structure. In order to simplify the calculations, we can choose a momentum parameterization that removes the magnetic flux dependence of the integrand. By doing so, the imaginary term inside the modulus will vanish, and only the ∂_y term will remain as the momentum dependence after a Fourier transformation. That is,

$$\begin{aligned}
S_d = \pi\nu L \int dq \left\{ D|qd_\alpha|^2 + [\hat{v}_i^a(\epsilon_1)m_i^a(\epsilon_1) + \hat{v}_i^b(\epsilon_2)m_i^b(\epsilon_2)]|d_\alpha|^2 \right. \\
+ \frac{e^2\mathbf{E}_\phi^2}{4}[m_3^a(\epsilon_1) + m_3^b(\epsilon_2)]^2|d_\alpha|^2 + \\
\left. - e^2\mathbf{E}_\phi^2[m_2^a(\epsilon_1)^2 + m_2^b(\epsilon_2)^2]|d_\alpha|^2 - 2e^2\mathbf{E}_\phi^2[m_2^a(\epsilon_1)m_2^b(\epsilon_2)]\text{Re}[d_\alpha^*d_{\bar{\alpha}}] \right\}. \quad (4.78)
\end{aligned}$$

To develop the matrix structure and solve the nontrivial term in the last line for the eigenvalue calculation, we introduce a transformation $d_\alpha = d'_\alpha + id''_\alpha$, where d'_α and d''_α are real-valued fields. This transformation allows us to separate the action into two sectors, which can be summarized as follows:

$$\begin{aligned}
\frac{S_c}{\pi\nu L} = d'_\alpha(q)\mathcal{O}_{\epsilon_1\epsilon_2}^{ab}d'_\alpha(-q) + d'_\alpha(q)N_{\epsilon_1\epsilon_2}^{ab}d''_\alpha(-q) \\
+ d''_\alpha(q)\mathcal{O}_{\epsilon_1\epsilon_2}^{ab}d''_\alpha(-q) - d''_\alpha(q)N_{\epsilon_1\epsilon_2}^{ab}d''_\alpha(-q), \quad (4.79)
\end{aligned}$$

where we have defined

$$\begin{aligned}
\mathcal{O}_{\epsilon_1\epsilon_2}^{ab} = Dq^2 + [\hat{v}_i^a(\epsilon_1)m_i^a(\epsilon_1) + \hat{v}_i^b(\epsilon_2)m_i^b(\epsilon_2)] + \frac{e^2\mathbf{E}_\phi^2}{4}[m_3^a(\epsilon_1) + m_3^b(\epsilon_2)]^2 + \\
- e^2\mathbf{E}_\phi^2[m_2^a(\epsilon_1)^2 + m_2^b(\epsilon_2)^2], \quad (4.80)
\end{aligned}$$

$$N_{\epsilon_1\epsilon_2}^{ab} = -2e^2\mathbf{E}_\phi^2[m_2^a(\epsilon_1)m_2^b(\epsilon_2)]. \quad (4.81)$$

This is a matrix structure for the vectors d_α , where the indices are given by $\epsilon_{1,2}$ and ab components. The diagonal terms correspond to the case when $\epsilon_1 = \epsilon_2$ and $a = b$. In this

case, the eigenvalues can be expressed as $\mathcal{O}_{\epsilon_1\epsilon_1}^{aa} \pm N_{\epsilon_1\epsilon_1}^{aa}$. The remaining terms

$$\frac{S_c}{\pi\nu L} = \chi_q M_{\epsilon_1\epsilon_2,ab}^C \chi_{-q}, \quad (4.82)$$

where

$$\mathcal{M}_{\epsilon_1\epsilon_2,ab} = \begin{pmatrix} \mathcal{O}_{\epsilon_1\epsilon_2,ab}^C & N_{\epsilon_1\epsilon_2,ab} & 0 & 0 \\ N_{\epsilon_1\epsilon_2,ab} & \mathcal{O}_{\epsilon_1\epsilon_2,ab}^C & 0 & 0 \\ 0 & 0 & \mathcal{O}_{\epsilon_1\epsilon_2,ab}^C & -N_{\epsilon_1\epsilon_2,ab} \\ 0 & 0 & -N_{\epsilon_1\epsilon_2,ab} & \mathcal{O}_{\epsilon_1\epsilon_2,ab}^C \end{pmatrix}, \quad (4.83)$$

$$\begin{aligned} \chi_q &= \begin{pmatrix} c' & (c')^t & c'' & (c'')^t \end{pmatrix}_q \\ &= \begin{pmatrix} c'_{\epsilon_1\epsilon_2,ab} & c'_{\epsilon_2\epsilon_1,ba} & c''_{\epsilon_1\epsilon_2,ab} & c''_{\epsilon_2\epsilon_1,ba} \end{pmatrix}_q, \end{aligned} \quad (4.84)$$

$$\chi_{-q} = \begin{pmatrix} c' \\ (c')^t \\ c'' \\ (c'')^t \end{pmatrix}_{-q} = \begin{pmatrix} c'_{\epsilon_1\epsilon_2,ab} \\ c'_{\epsilon_2\epsilon_1,ba} \\ c''_{\epsilon_1\epsilon_2,ab} \\ c''_{\epsilon_2\epsilon_1,ba} \end{pmatrix}_{-q}, \quad (4.85)$$

where the transposition occurs only in the subspaces of this matrix structure. The eigenvalues for the matrix $\mathcal{M}_{\epsilon_1\epsilon_2,ab}$ are given by

$$\lambda_{\epsilon_1\epsilon_2,ab} = \mathcal{O}_{\epsilon_1\epsilon_2,ab}^C \pm N_{\epsilon_1\epsilon_2,ab}, \quad (4.86)$$

where each of them is doubly degenerate for each of the blocks accounted. With this result in mind and with the help of definitions (4.19) and (4.22) we rewrite our variation $K(\phi_1, \phi_2)$ as

$$K(\phi_1, \phi_2) = (2eT)^2 \sum_{\pm} \sum_q \sum_{\epsilon_1 > 0, \epsilon_2} \left(\frac{d^2 \lambda_{\epsilon_1, \epsilon_2}^s}{d\phi_1 d\phi_2} \frac{1}{\lambda_{\epsilon_1, \epsilon_2}^s} - \frac{d\lambda_{\epsilon_1, \epsilon_2}^s}{d\phi_1} \frac{d\lambda_{\epsilon_1, \epsilon_2}^s}{d\phi_2} \frac{1}{(\lambda_{\epsilon_1, \epsilon_2}^s)^2} \right) \quad (4.87)$$

where frequencies ϵ_2 positive and negative account for the Cooperon and Diffuson contribution, respectively. This is a useful expression to use later to calculate the fluctuations

on the supercurrent.

4.10 Average current and sample-to-sample fluctuations at zero magnetic field

We now consider the average Josephson current and its fluctuations at zero magnetic field in the setup shown in Figure (1.4), following the results published in [83]. In this setup, the largest energy scale is given by $E_{\text{Th}} = D/L^2$, the Thouless energy. It represents the characteristic energy scale for diffusive motion in confined disordered systems. We further distinguish between two cases: the quantum dot geometry with a confined transverse direction, where $E_{\text{Th}}^\perp = D/W^2 \gg \{\Delta, E_t\}$, where E_{Th} is the Thouless energy related to the transverse direction, and the quasi-one-dimensional geometry with an extended transverse direction, where $E_{\text{Th}}^\perp \ll \{\Delta, E_t\}$.

4.10.1 Average current

From Equation (4.19), we can derive a new expression for the supercurrent near the saddle point. In this derivation, we use the action given by Equation (4.68), which does not include the fluctuation factors that need to be taken into account when performing the fluctuation calculation. The new expression for the supercurrent is obtained as follows:

$$I(\phi) = 2eT \frac{d}{d\phi} S_0 \quad (4.88)$$

$$= e\pi TV\nu A_s \frac{d}{d\phi} \sum_{\epsilon} \left(2De^2 E_{\phi}^2 m_2^2 - v_i m_i \right). \quad (4.89)$$

The solution of the saddle point equation in the absence of a magnetic field is given by $Q_{\Delta} = \hat{n}_i \sigma_i^{\text{ph}}$. By setting $E_{\Phi} = 0$ and $m_i = n_i$ in Equation (4.89), we can find the average current $I(\phi)$. In this case, the mean field vector $\hat{\mathbf{m}}$ is parallel to \mathbf{v} , resulting in the following expression for the average current:

$$I(\phi) = \frac{GE_t}{2e} J(\phi), \quad J(\phi) = 4\pi \sin(\phi) T \sum_{\epsilon > 0} \frac{\Delta^2}{\omega(\Delta, \epsilon) v(\epsilon, \phi)}. \quad (4.90)$$

In the above expression, we have introduced the notation $v(\epsilon, \phi) = |\mathbf{v}|$ to indicate the dependence of the scalar on the phase difference ϕ and the fermionic Matsubara frequency

ϵ . Additionally, we defined $\omega(\Delta, \epsilon) = \Delta^2 + \epsilon^2$. The relation $E_t = \delta G/2e^2$ connects the dwell energy with the normal-state conductance of the junction, where δ represents the mean level spacing. Equation (4.90) is valid for arbitrary ratios $e_t \equiv E_t/\Delta$. It is worth noting that the average Josephson current does not depend on the width of the junction. Equation (4.90) is consistent with previously reported results [80, 81, 82].

Next, we will explore the parameter dependence of the average current in the limiting cases of long and short dwell times, $E_t \ll \Delta$ and $E_t \gg \Delta$, respectively. In these cases, simple analytical solutions can be obtained. Subsequently, we will discuss arbitrary dwell times based on a fully numerical evaluation of Equation (4.90).

Long dwell time: $E_t \ll \Delta$

In the limit $E_t \ll \Delta$, we can make the approximation $v_3 \approx \epsilon$, as given by (4.52). The scale for the average current is then determined by $GE_t/2e$, and J becomes a function of the dimensionless variables $t = T/\Delta$ and $e_t = E_t/\Delta$ only.

In this approximation, and at low temperatures where $T \ll \Delta$, the dimensionless $J(\phi)$ takes on the following asymptotic form [84, 82]:

$$J(\phi) = 2 \sin(\phi) \ln \left[\frac{1}{\max(t, e_t \cos(\phi/2))} \right]. \quad (4.91)$$

Short dwell time: $E_t \gg \Delta$

In the short dwell time limit and at zero temperature, the dimensionless function $J(\phi)$ is proportional to the complete elliptic integral of the first kind, denoted as \mathbf{K} , as reported in previous studies [84, 82],

$$J(\phi) = \frac{1}{e_t} \sin(\phi) \mathbf{K} \left(\sin^2 \frac{\phi}{2} \right) = \frac{1}{e_t} \sin(\phi) \int_0^\infty dy \frac{1}{\sqrt{\cos^2(\phi/2) + \sinh^2 y}}. \quad (4.92)$$

It is worth noting that the scale of the average current is determined by the order parameter Δ . This can be observed by comparing the expressions for the average current in Eqs. (4.90) and (4.92).

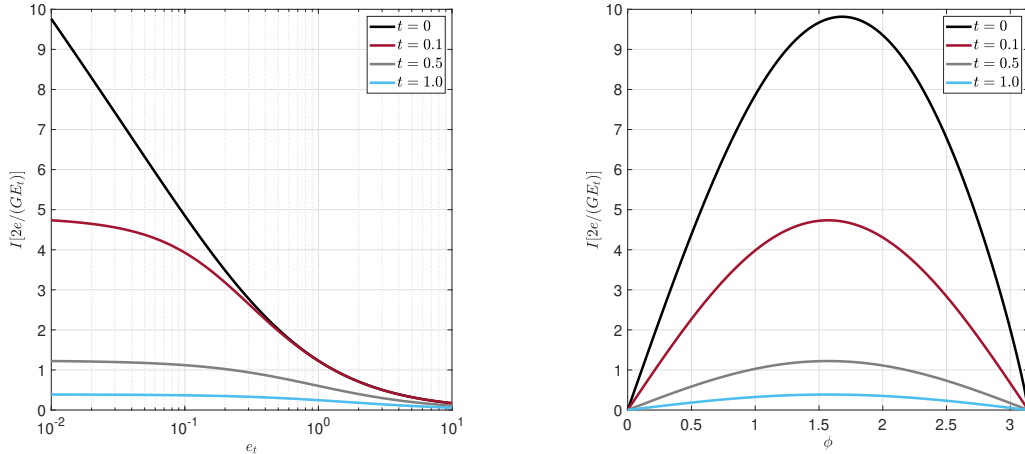


Figure 4.3: The average current $I(\phi)$ at zero magnetic field as a function of the dwell energy $e_t = E_t/\Delta$ for various values of $t = T/\Delta$ and $\phi = \pi/2$ on the left hand side, and as a function of ϕ for various t and $e_t = 0.01$, on the right hand side.

Arbitrary dwell time

For the general case of arbitrary dwell times, we use (4.90) to perform numerical calculations and analyze the dependence of the average current I on t and e_t . The results of these calculations are shown in Figure 4.3.

As expected from (4.91), the average current I monotonically increases as the temperature decreases, and the weak low-temperature singularity is cutoff for finite e_t . Similarly, I increases with decreasing e_t , but the growth is limited for finite T . The dependence of I on the phase difference ϕ is illustrated in Figure 4.3 for a fixed e_t . At the lowest temperatures, the average current reaches its maximum around $\phi = \pi/2$. At $\phi = 0$ and $\phi = \pi$, the average current vanishes. Overall, the ϕ -dependence of the average current I is dominated by the prefactor $\sin(\phi)$ in (4.90).

It is worth noting that the average Josephson current does not depend on the width of the junction. However, this is not the case for the sample-to-sample fluctuations, which we will discuss next.

4.10.2 Sample-to-sample fluctuations

The calculation of the current fluctuations requires knowing the eigenvalues $\lambda_{\epsilon_1, \epsilon_2}^{\pm}$ of the fluctuation determinant, as given in (4.86). In the case of a vanishing magnetic field, the eigenvalues for both Diffusons and Cooperons become identical and can be expressed as

follows:

$$\lambda_{\epsilon_1, \epsilon_2} = Dq^2 + v(1) + v(2), \quad (4.93)$$

where $(i) = (\epsilon_i, \phi_i)$ is a convenient multi-index notation. At zero magnetic field, using (4.87), we obtain the general formula for the current fluctuations,

$$\text{var}I(\phi) = (4eT)^2 \sum_{\epsilon_1, \epsilon_2 > 0} \sum_q \frac{\partial_{\phi_1} v(1) \partial_{\phi_2} v(2)}{[Dq^2 + v(1) + v(2)]^2}. \quad (4.94)$$

Compared to the results reported in Refs. [84, 43], the variance in (4.94) is four times smaller. This is due to the strong spin-orbit coupling in the topological insulator surface, which suppresses fluctuations in the spin triplet channel, while the singlet mode remains effective. We will discuss the current fluctuations in two limits, the quantum dot geometry, for which $E_{\text{Th}}^\perp \gg E_t$, and the quasi-one-dimensional limit $E_{\text{Th}}^\perp \ll E_t$. Quantum dots are structures that confine electrons in all three spatial dimensions. The confinement leads to discrete energy levels, similar to an atom. When quantum dots are so small in two of its dimensions it leads to a strong confinement in one direction only. The Thouless energy can indicate the extent of confinement in the system, a larger E_{Th} indicates a strong confinement, then indicating the geometry in which the model is subjected.

Quantum dot limit, $E_{\text{Th}}^\perp \gg E_t$:—In the quantum dot geometry, spatial fluctuations of the Diffuson modes in the transverse direction can be neglected and the current fluctuations are given by [84]

$$\begin{aligned} \text{var}I_0(\phi) &= e^2 E_t^2 \mathcal{K}_0(\phi), \\ \mathcal{K}_0(\phi) &= \sin^2(\phi) T^2 \sum_{\epsilon_1, \epsilon_2 > 0} \frac{16E_t^2 \Delta^4}{\omega(\Delta, \epsilon_1) \omega(\Delta, \epsilon_2) v(1) v(2) [v(1) + v(2)]^2}, \end{aligned} \quad (4.95)$$

where the sub-index in the sample-to-sample fluctuations denotes the effective dimensionality of the system. In Figure 4.4, the variance $\text{var}I_0$ is displayed as a function of the ratio E_t/Δ .

Quasi-one-dimensional limit, $E_{\text{Th}}^\perp \ll E_t$:— In the quasi-one-dimensional geometry spatial fluctuations of the Diffuson modes in the transverse direction have to be taken into

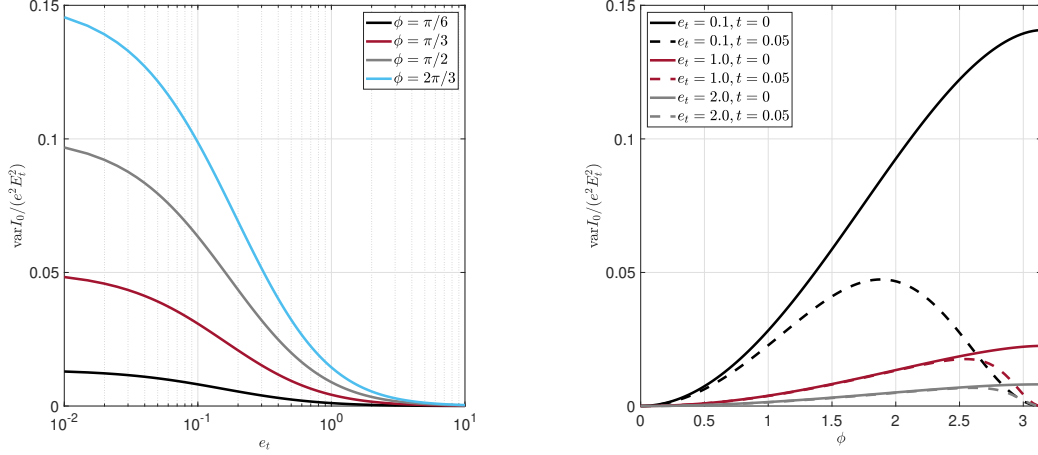


Figure 4.4: On the right hand side, the variance of the Josephson current as a function of the phase difference ϕ in the quantum dot geometry. Solid lines represent the zero temperature limit, whereas dashed lines denote the finite temperature limit. On the left hand side, we display \mathcal{K}_0 as a function of $e_t = E_t/\Delta$ for various fixed phases, $\phi = \pi/6, \pi/3, \pi/2, 2\pi/3$.

account. Employing the same equation (4.87) as in the previous limit and performing the sum over momenta q , we obtain the following expression for the variance of the Josephson current

$$\begin{aligned} \text{var} I_1(\phi) &= e^2 E_t^2 \sqrt{\frac{E_t}{E_{\text{Th}}^\perp}} \mathcal{K}_1(\phi), \\ \mathcal{K}_1(\phi) &= 4 \sin^2(\phi) T^2 \sum_{\epsilon_1, \epsilon_2 > 0} \frac{\Delta^4 E_t^{3/2}}{\omega(\Delta, \epsilon_1) \omega(\Delta, \epsilon_2) v(1) v(2) [v(1) + v(2)]^{3/2}}. \end{aligned} \quad (4.96)$$

The plot for the current fluctuations $\text{var} I_1(\phi)$ is shown in Figure 4.5. Next, we move on to discuss the current fluctuations specifically in the limit of long and short dwell times.

Long dwell time: $E_t \ll \Delta$

Quantum dot limit, $E_{\text{Th}}^\perp \gg E_t$:—In the long dwell time limit and at zero temperature, the scale for the variance of the current is set by E_t^2 , and we obtain an analytical expression

$$\begin{aligned} \text{var} I_0(\phi) &= e^2 E_t^2 \mathcal{K}_0(\phi), \\ \mathcal{K}_0(\phi) &= \frac{\sin^2(\phi)}{\pi^2} \iint_0^\infty \frac{dx_1 dx_2}{\sqrt{X_1(\phi) X_2(\phi)} \left(\sqrt{X_1(\phi)} + \sqrt{X_2(\phi)} \right)^2}, \end{aligned} \quad (4.97)$$

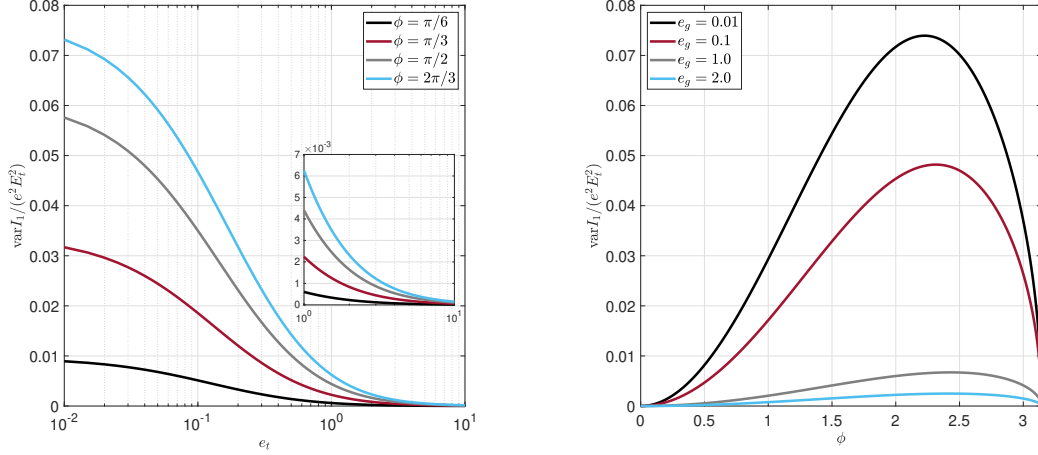


Figure 4.5: On the right hand side, the variance of the Josephson current as a function of the phase difference ϕ in the quasi-one-dimensional geometry. On the left hand side, we display \mathcal{K}_1 as a function of $e_t = E_t/\Delta$ for various fixed phases, $\phi = \pi/6, \pi/3, \phi/2, 2\pi/3$.

where $X_i(\phi) = \cos^2(\phi/2) + x_i^2$ and $x_i = \epsilon_i/\Delta$. Investigating the behavior of the function \mathcal{K}_0 , we observe that its dependence on the phase difference ϕ can be described by a simple power-law in $\cos \phi/2$, $\mathcal{K}_0 \approx \sin^2(\phi)[\cos(\phi/2)]^{-2}$. At $\phi = \pi$, we expect that both the average current and the current fluctuations vanish. However, it is clear that \mathcal{K}_0 does not reproduce this behavior as the phase ϕ approaches π . Such failure has to do with the violation of the criterion of validity for our Gaussian approximation, whose existence hinges on the small parameter $\lambda/\delta \gg 1$, λ being an eigenvalue of the Gaussian action and δ the mean level spacing. In this approximation, the mass of the system is proportional to $\cos(\phi/2)$ and as a consequence when the phase becomes close to π the criterion of validity for our approximation is no longer satisfied. A more detailed analysis of the action reveals the correct result in this limit [43]. As already suggested in [84], the vanishing of the average current and the current fluctuations for $\phi \rightarrow \pi$ is restored at finite temperatures even in the Gaussian approximation, as can be seen in Figure 4.4.

Quasi-one-dimensional limit, $E_{\text{Th}}^\perp \ll E_t$:—Focusing on the zero-temperature limit, we transform summations over Matsubara frequencies into integrations again, and express the latter in terms of dimensionless quantities to find

$$\begin{aligned} \text{var} I_1(\phi) &= e^2 E_t^2 \sqrt{\frac{E_t}{E_{\text{Th}}^\perp}} \mathcal{K}_1(\phi), \\ \mathcal{K}_1(\phi) &= \frac{\sqrt{2} \sin^2(\phi)}{4\pi^2} \iint_0^\infty \frac{dx_1 dx_2}{\sqrt{X_1(\phi) X_2(\phi)} \left(\sqrt{X_1(\phi)} + \sqrt{X_2(\phi)} \right)^{\frac{3}{2}}}. \end{aligned} \quad (4.98)$$

The scale of the fluctuations is now set not only by the squared dwell energy but also by the parameter $\sqrt{E_t/E_{\text{Th}}^\perp}$. The result of the integrations in x_1 and x_2 can be approximated by a power law in $\cos \phi/2$ and, as a consequence, the phase dependence of $\mathcal{K}_1(\phi)$ is governed by the function $\sin^2(\phi)[\cos(\phi/2)]^{-3/2}$, which monotonically vanishes as ϕ approaches π . The presence of a momentum structure in the Gaussian action leads to this significant difference in comparison to the quantum dot geometry, for which finite temperatures had to be invoked in order to reproduce this behavior in the Gaussian approximation.

Short dwell time: $E_t \gg \Delta$

Quantum dot limit, $E_{\text{Th}}^\perp \gg E_t$:—At zero temperature, the current fluctuations read as [85]

$$\text{var}I_0(\phi) = e^2 E_t^2 \mathcal{K}_0(\phi), \quad \mathcal{K}_0(\phi) = \frac{\Delta^2}{E_t^2} \mathcal{K}_0^S(\phi), \quad (4.99)$$

$$\mathcal{K}_0^S(\phi) = \frac{\sin^2(\phi)}{4\pi^2} \iint_0^\infty \frac{\sqrt{X_1(0)}\sqrt{X_2(0)}dx_1dx_2}{\sqrt{X_1(\phi)}\sqrt{X_2(\phi)} [\sqrt{X_2(0)}\sqrt{X_1(\phi)} + \sqrt{X_1(0)}\sqrt{X_2(\phi)}]^2}. \quad (4.100)$$

A quick inspection of this expression reveals that in this regime the scale is now set by Δ^2 . In this limit, when ϕ approaches π the product between $\sin^2(\phi)$ and the dimensionless function \mathcal{K}_0^S yields a non-zero result, which clearly violates the condition $\text{var}I_0(\pi) = 0$. As already found in the long dwell time limit, finite temperatures restore the correct behavior in our formalism, see Figure 4.4.

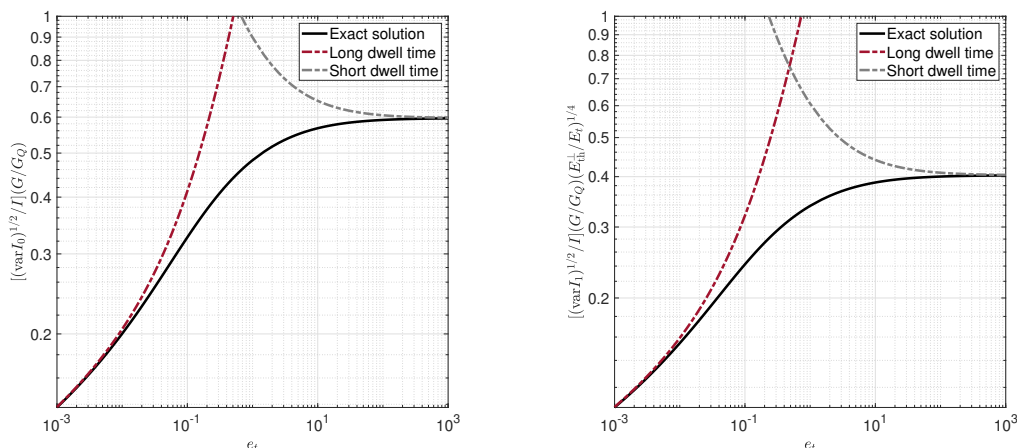


Figure 4.6: The ratio between the current fluctuations and the average current as a function of e_t in the absence of a magnetic field and at zero temperature. On the left hand side, we show this ratio for the quantum dot geometry, on the right hand side for the quasi-one-dimensional case.

Quasi-one-dimensional limit, $E_{\text{Th}}^{\perp} \ll E_t$:—Considering the zero temperature limit, the current fluctuations yield

$$\text{var} I_1(\phi) = e^2 E_t^2 \sqrt{\frac{E_t}{E_{\text{th}}^{\perp}}} \mathcal{K}_1(\phi), \quad \mathcal{K}_1(\phi) = \frac{\Delta^2}{E_t^2} \mathcal{K}_1^S(\phi), \quad (4.101)$$

$$\mathcal{K}_1^S(\phi) = \frac{\sqrt{2} \sin^2(\phi)}{16\pi^2} \iint_0^{\infty} \frac{[X_1(0)]^{1/4} [X_2(0)]^{1/4} dx_1 dx_2}{\sqrt{X_1(\phi)} \sqrt{X_2(\phi)} \left(\sqrt{X_2(0)} \sqrt{X_1(\phi)} + \sqrt{X_1(0)} \sqrt{X_2(\phi)} \right)^{3/2}}. \quad (4.102)$$

In analogy to the long dwell-time limit, in a quasi-one-dimensional geometry the scale is set by Δ^2 , and also by the parameter $\sqrt{E_t/E_{\text{Th}}^{\perp}}$. In addition to that, as in the previous cases, we find that the quasi-one-dimensional geometry restores the correct result for the fluctuations at $\phi = \pi$, $\text{var} I_1(\pi) = 0$, see details in Figure 4.5.

Arbitrary dwell time

We can now compare the magnitudes of fluctuations and the average current for the quantum dot and the quasi-one-dimensional geometry. For the quantum dot geometry, we find

$$\frac{[\text{var} I_0(\phi)]^{1/2}}{I(\phi)} = \frac{G_Q [4\pi^2 \mathcal{K}_0(\phi)]^{1/2}}{G J(\phi)}. \quad (4.103)$$

In the quasi-one-dimensional geometry, we obtain the following expression

$$\frac{[\text{var} I_1(\phi)]^{1/2}}{I(\phi)} = \frac{G_Q}{G} \left(\frac{E_t}{E_{\text{Th}}^{\perp}} \right)^{1/4} \frac{[4\pi^2 \mathcal{K}_1(\phi)]^{1/2}}{J(\phi)}. \quad (4.104)$$

With the help of Eqs. (4.91), (4.92), (4.97), (4.98), (4.99) and (4.101), we can estimate that the ratios in Eqs. (4.103) and (4.104) are of the order of G_Q/G , where $G_Q = e^2/\pi$ is the conductance quantum. Furthermore, as a result of the hierarchy of energy scales, $\delta \ll E_t \ll \Delta \ll E_{\text{th}}$, for a quasi-one-dimensional system, the ratio is proportional to the parameter $E_t/E_{\text{Th}}^{\perp}$. As we observe in Figure 4.6, for both geometries the approximate analytical results obtained in this section are in good agreement with numerical results. In the long dwell-time limit, the fluctuation-to-average current ratio behaves as $1/\log(1/e_t)$ and in the short dwell-time limit the dwell energy dependence is completely absent, hence the ratio tends to a constant value. Next we discuss how these findings are changed in presence of a magnetic field.

4.11 Average current and sample-to-sample fluctuations at finite magnetic field

As previously discussed, we continue to explore the weak coupling regime $E_t \ll \Delta$ where the mini-gap is set by the dwell energy E_t . The magnetic field then allows to tune the population of sub-gap states, with mini-gap closure at $E_\Phi \sim E_t$, while pair-breaking effects on the superconducting leads can be neglected. We focus on the sensitivity of the average Josephson current and its fluctuations to the mini-gap closure at strong magnetic fields, where an analytical solution of the mean field equation is available. These analytical calculations are complemented by calculations building on the numerical solution of the mean field equation and allowing to describe the crossover into the weak magnetic field regime. Starting out from the general expression for the current phase relation

$$I(\phi) = -\pi\nu eTV \sum_{\epsilon} \left[\partial_{\phi} \left(2v_i m_i - E_{\Phi} m_2^2 \right) \right], \quad (4.105)$$

we find the average current in the strong magnetic field limit,

$$I_{\Phi}(\phi) = \left(\frac{GE_t}{e} \right) \operatorname{Re} \left[\sum_{\epsilon > 0} \frac{2\pi t \sin \phi}{(e_{\Phi} + |\epsilon|)(1 + i\epsilon)} \right]. \quad (4.106)$$

The summation is then readily done using the identity

$$\sum_{n=0}^{\infty} \frac{1}{(n+a)(n+b)} = \frac{\psi(a) - \psi(b)}{a-b}, \quad (4.107)$$

resulting in

$$I_{\Phi}(\phi) = \left(\frac{GE_t}{e} \right) \operatorname{Re} \left[\frac{(1 + ie_{\Phi})\psi\left(\frac{1}{2} - \frac{i}{2\pi t}\right) - (1 + ie_{\Phi})\psi\left(\frac{1}{2} + \frac{e_{\Phi}}{2\pi t}\right)}{1 + e_{\Phi}^2} \right] \sin \phi, \quad (4.108)$$

where ψ is the polygamma function.

4.11.1 Average current

From the mean field solution $Q_\Delta = \hat{m}_i \hat{\sigma}_i$, with \hat{m}_i in the limit $E_\Phi \gg E_t$, and (4.19) we find the average Josephson current at strong magnetic fields

$$I_\Phi(\phi) = \frac{GE_t}{2e} J_\Phi, \quad J_\Phi = 4\pi \sin(\phi) T \sum_{\epsilon > 0} \frac{\Delta^2}{(\epsilon + E_\Phi)\Delta^2 + \epsilon(\epsilon^2 + 2E_t\sqrt{\Delta^2 + \epsilon^2} + \epsilon E_\Phi)}. \quad (4.109)$$

Using that $E_t \ll \Delta$, we can neglect terms involving the dwell energy in J_Φ , and perform the summation arriving at an expression for the average Josephson current in terms of polygamma functions. The result is shown in Figure 4.7.

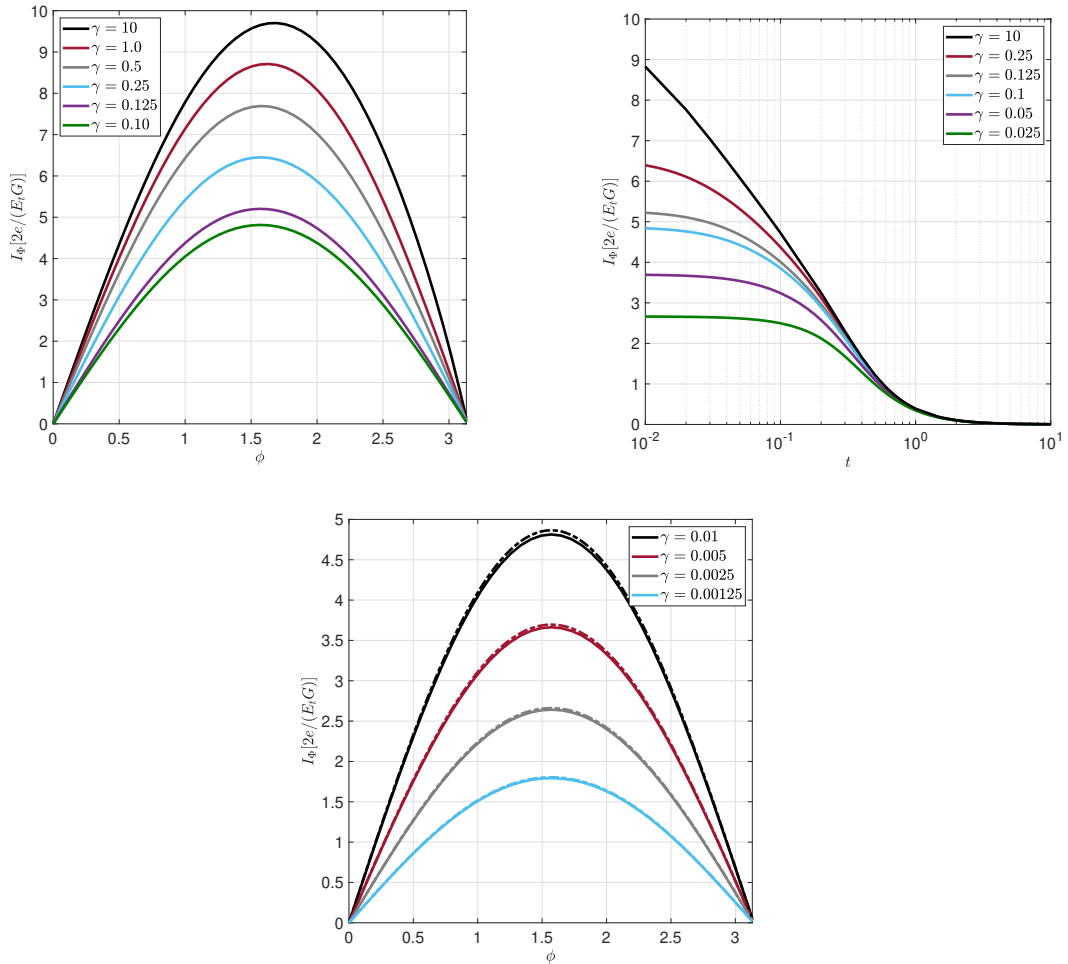


Figure 4.7: Left panel: J_Φ at zero temperature as a function of ϕ and for various values of $\gamma = E_t/E_\Phi$. Right panel: J_Φ as a function of temperature $t = T/\Delta$ for various values of γ , cf. (4.109). Here the dwell energy is chosen as $e_t = E_t/\Delta = 1/100$ and the phase difference as $\phi = \pi/2$. Bottom panel: The average current at zero temperature for various values of $\gamma = E_t/E_\Phi$, where we fixed $e_t = E_t/\Delta = 1/1000$. The solid lines represent the exact numerical solution and dash-dotted lines the analytical approximation.

The scale for the current is set by $GE_t/(2e)$, similar to the zero magnetic field case $B = 0$. In contrast to the latter, the phase dependence of J_Φ in the strong magnetic field limit is, however, fully governed by the sine function, (4.109). Technically, corrections to the mean field solution (4.60) are suppressed in $E_t/E_\Phi \ll 1$ giving only insignificant contributions, and deviations from a sinusoidal behavior are therefore strongly suppressed. As evident from (4.109), increasing the external magnetic field monotonically suppresses the average Josephson current. At low temperatures $T \ll \Delta$, the dimensionless function J_Φ shares the logarithmic asymptotic form of the zero magnetic field expression

$$J_\Phi = 2 \sin(\phi) \ln \left[\frac{1}{\max(t, e_\Phi)} \right], \quad (4.110)$$

where now $E_\Phi \gg E_t$ replaces the dwell energy E_t found at $B = 0$.

From the numerical solution of the mean field equation, we can calculate the average current for arbitrary ratios of E_t/E_Φ . The result is shown in Figure 4.7. The average current as a function of the phase (left panel) shows a dominant sinusoidal behavior for all ratios E_t/E_Φ , attaining its maximum at $\pi/2$ in the strong magnetic field limit, which is slightly shifted to larger values with increasing ratio E_t/E_Φ . The phase-dependence of the current does not show any signs of Fraunhofer patterns, in agreement with the discussions in [86], [87] and [88]. The average current as a function of temperature is shown in the right panel of Figure 4.7. Since the weak logarithmic divergence of (4.110) is cut off by the larger of T and E_Φ , the average current at low temperatures $T \ll \Delta$ decreases with increasing magnetic field, and all curves for different values E_t/E_Φ then collapse into a single curve at high temperatures $T \gg \Delta$.

Finally, we compare in bottom panel of Figure 4.7 the average current from the analytical mean field solution at strong magnetic fields to the exact current obtained from the numerical solution of the mean field equation, here at zero temperature and $e_t = E_t/\Delta = 1/1000$. As expected, the analytical solution describes the average current very well for these small values $E_t/E_\Phi \leq 0.01$.

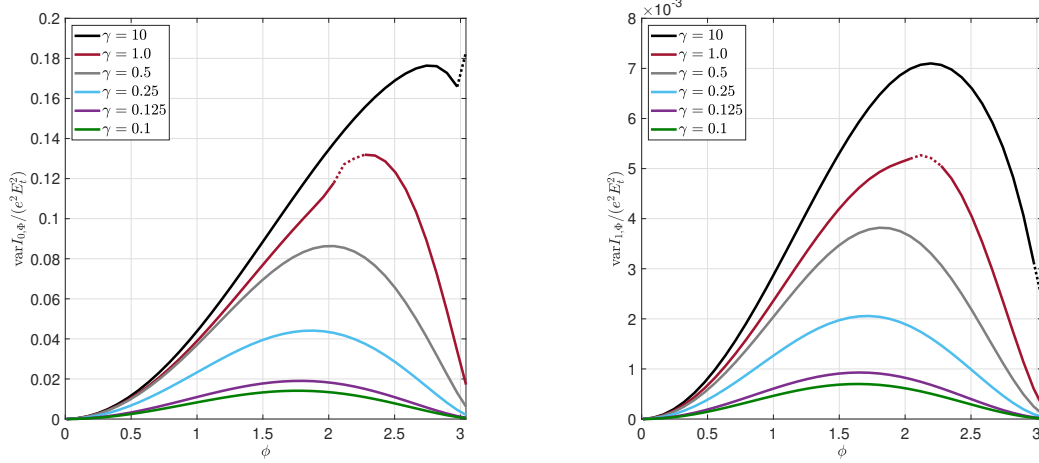


Figure 4.8: Left panel: $\mathcal{K}_{0,\Phi}$ (quantum dot) as a function of phase angle ϕ for various values of $\gamma = E_t/E_\Phi$. Right panel: $\mathcal{K}_{1,\Phi}$ (quasi-one-dimensional geometry) as a function of phase difference ϕ for various values of $\gamma = E_t/E_\Phi$. The dashed lines indicate the parameter region for which the semiclassical approximation becomes uncontrolled. In all figures we fixed $e_t = E_t/\Delta = 1/100$ and varied E_Φ .

4.11.2 Sample-to-sample fluctuations

To prepare the calculation of current fluctuations, we first notice that eigenvalues of Diffuson and Cooperon modes (X=D,C) at strong magnetic fields become

$$\lambda_{\epsilon_1, -\epsilon_2}^{X,\pm} = Dq^2 + \epsilon_1 + \epsilon_2 + M_X^\pm(\epsilon_1, \epsilon_2), \quad (4.111)$$

with Diffuson masses M_D^s

$$M_D^\pm(\epsilon_1, \epsilon_2) = 2E_t^2 \Delta^2 \cos^2\left(\frac{\phi}{2}\right) \times \left[\sum_{i=1}^2 \frac{1}{(E_\Phi + \epsilon_i) \sqrt{\omega(\Delta, \epsilon_i)}} \mp \frac{2E_\Phi}{\sqrt{(E_\Phi + \epsilon_1)(E_\Phi + \epsilon_2) \omega(\Delta, \epsilon_1) \omega(\Delta, \epsilon_2)}} \right], \quad (4.112)$$

and Cooperon masses $M_C^\pm = M_D^\pm + E_\Phi/2$. Notice that the magnetic field lifts previous degeneracies at $B = 0$, and all four modes ($D/C, \pm$) now contribute differently to the current fluctuations. Then, starting out from the general expression for current fluctuations

(4.87)

$$\text{var}I_{\Phi}(\phi) = (2eT)^2 \sum_{s=\pm} [F_2^s(\phi) - F_1^s(\phi)], \quad (4.113)$$

we employ that in the limit of strong magnetic fields the functions F_1^s and F_2^s are given by

$$F_1^s(\phi) = \sum_{X=D,C} \sum_{\epsilon_1, \epsilon_2 > 0} \sum_q \frac{\partial_1[M_X^s(\epsilon_1, \epsilon_2)] \partial_2[M_X^s(\epsilon_1, \epsilon_2)]}{[Dq^2 + \epsilon_1 + \epsilon_2 + M_X^s(\epsilon_1, \epsilon_2)]^2}, \quad (4.114)$$

$$F_2^s(\phi) = \sum_{X=D,C} \sum_{\epsilon_1, \epsilon_2 > 0} \sum_q \frac{\partial_{12}^2 M_X^s(\epsilon_1, \epsilon_2)}{Dq^2 + \epsilon_1 + \epsilon_2 + M_X^s(\epsilon_1, \epsilon_2)}. \quad (4.115)$$

We next explore these general expression for the two geometries of interest, that is, the quantum dot and quasi-one-dimensional structure, defined by $E_{\text{Th}}^{\perp} \gg E_t$ and $E_{\text{Th}}^{\perp} \ll E_t$, respectively.

Quantum dot limit: $E_{\text{Th}}^{\perp} \gg E_t$

Current fluctuations for the quantum dot geometry in the zero temperature limit can be simplified to

$$\text{var}I_{0,\Phi}(\phi) = e^2 E_t^2 \mathcal{K}_{0,\Phi}(\phi), \quad \mathcal{K}_{0,\Phi}(\phi) = \left(\frac{E_t}{E_{\Phi}}\right)^2 \mathcal{F}_{0,\Phi}(\phi), \quad (4.116)$$

$$\mathcal{F}_{0,\Phi}(\phi) = \frac{\sin^2(\phi)}{\pi^2} \sum_{X=C/D} \sum_{s=\pm 1} [f_{0,1}^{X,s}(\phi, \gamma) + f_{0,2}^{X,s}(\phi, \gamma)], \quad (4.117)$$

with functions $f_{0,1}$ and $f_{0,2}$ defined as

$$f_{0,1}^{X,1}(\phi, \gamma) + f_{0,1}^{X,-1}(\phi, \gamma) = 2 \iint_0^{\infty} dx dx' \frac{\omega(1, e_{\Phi} x) \omega(1, e_{\Phi} x')}{\Omega_X^+(x, x') \Omega_X^-(x, x')}, \quad (4.118)$$

$$f_{0,2}^{X,s}(\phi, \gamma) = \iint_0^{\infty} dx dx' \frac{\eta_X^s(x, x')}{[\Omega_X^s(x, x')]^2}. \quad (4.119)$$

To write the equations in a compact manner, we used $\omega(\Delta, \epsilon) = \Delta^2 + \epsilon^2$ and introduced

$$\begin{aligned}\eta_X^s(x_1, x_2) &= \prod_{i \neq j, i, j=1}^2 \left[\omega(1, e_\Phi x_i) - sb_X(x_i)(1+x_j) \sqrt{\omega(1, e_\Phi x_i) \omega(1, e_\Phi x_j)} \right] \\ \Omega_X^s(x_1, x_2) &= (a_X + x_1 + x_2) \prod_{i=1}^2 (1+x_i) \omega(1, e_\Phi x_i) + 2\gamma^2 \cos^2\left(\frac{\phi}{2}\right) \times \\ &\quad \times \left[\sum_{i=1}^2 (1+x_i) \omega(1, e_\Phi x_i) - 2s \sqrt{\omega(1, e_\Phi x_1) \omega(1, e_\Phi x_2)} \right].\end{aligned}$$

Here, the numerical constant a_X is 0 for Diffusons and 1/2 for Cooperons, and $b_D(\epsilon) = 1$ for Diffusons, respectively, $b_C(\epsilon) = (1/2)[1 + \epsilon/(1 + \epsilon)]$ for Cooperons.

While fluctuations in the absence of magnetic fields are set by the (squared) dwell energy, they are suppressed by the additional factor $(E_t/E_\Phi)^2$ in the strong magnetic field limit. The left panel of Figure 4.8 shows the current fluctuations $\text{var}I_{\Phi,0}$ as a function of ϕ for different values $\gamma = E_t/E_\Phi$. The increase of fluctuations with γ is clearly visible and we also observe a shift of the maximum from close to π at weak magnetic fields to smaller values as the magnetic field increases. We caution again that the semiclassical approximation loses its validity once the action takes values $\mathcal{O}(1)$. The corresponding regions are close to the maximum value of fluctuations and indicated by the dashed lines. For $E_t/E_\Phi \gtrsim 1$, the action becomes large enough to justify the semiclassical approximation for all values of ϕ .

In the left panel of Figure 4.9, we compare the analytical solution based on the analytical mean field solution at large magnetic fields to the fluctuations calculated using the exact numerical solution of the mean field equation. Again we find very good agreement for all values $\gamma < 0.01$.

Finally, we show in the left panel of Figure 4.10 the ratio between the square root of current fluctuations and average current for the quantum dot geometry in the strong magnetic field regime,

$$\frac{\sqrt{\text{var}I_{0,\Phi}(\phi)}}{I_\Phi(\phi)} = \left(\frac{G_Q}{G}\right) \left(\frac{E_t}{E_\Phi}\right) \frac{\sqrt{4\pi^2 \mathcal{F}_{0,\Phi}(\phi)}}{J_\Phi}. \quad (4.120)$$

As previously noted, large magnetic fields suppresses the relative size of fluctuations by an additional factor E_t/E_Φ compared to the zero magnetic field limit $B = 0$.

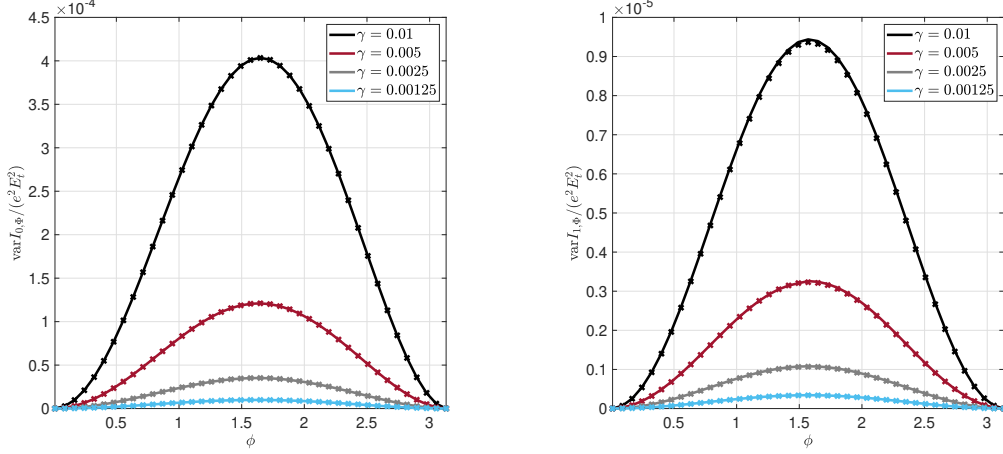


Figure 4.9: Current fluctuations in the strong magnetic field limit as a function of phase for various values $\gamma = E_t/E_\Phi$ (we here fixed $e_t = E_t/\Delta = 1/1000$ and varied E_Φ). Solid lines and markers denote the analytical result employing the approximate solution of the mean field equation and the result building on the numerical solution of the mean field equation, respectively. Left panel: quantum dot geometry. Right panel: quasi-one-dimensional geometry.

Quasi-one-dimensional limit: $E_{\text{Th}}^\perp \ll E_t$

For the quasi-one-dimensional geometry current fluctuations at zero temperature read

$$\text{var} I_{1,\Phi}(\phi) = e^2 E_t^2 \sqrt{\frac{E_t}{E_{\text{Th}}^\perp}} \mathcal{K}_{1,\Phi}(\phi), \quad \mathcal{K}_{1,\Phi}(\phi) = \sqrt{\frac{E_t^3}{E_\Phi^3}} \mathcal{F}_{1,\Phi}(\phi), \quad (4.121)$$

$$\mathcal{F}_{1,\Phi}(\phi) = \frac{\sin^2(\phi)}{\pi^2} \sum_{s=\pm} \sum_{X=C,D} (f_{1,1}^{X,s} + f_{1,2}^{X,s}). \quad (4.122)$$

Here, the functions $f_{1,i}^{X,s}$ depend on the ratio $\gamma = E_t/E_\Phi$ and are defined as

$$\sum_{s=\pm} f_{1,1}^{X,s}(\gamma) = \iint_0^\infty dx dx' \frac{1}{\sqrt{(1+x)(1+x')} \Omega_X^+(x,x') \Omega_X^-(x,x')} \times \frac{1}{\left[\sqrt{\Omega_X^+(x,x')} + \sqrt{\Omega_X^-(x,x')} \right]}, \quad (4.123)$$

$$f_{1,2}^{X,s}(\gamma) = \frac{1}{4} \iint_0^\infty dx dx' \frac{\eta_X^s(x,x')}{\sqrt{(1+x)(1+x')} [\Omega_X^s(x,x')]^3}. \quad (4.124)$$

As compared to the zero magnetic field limit, fluctuations at strong magnetic fields in the quasi-one-dimensional geometry are suppressed by an additional factor $(E_t/E_\Phi)^{3/2}$. In terms of this small parameter, the one-dimensional integration over momenta leads to a mildly weaker suppression of fluctuations compared to the quantum dot geometry.

The relative scale of current fluctuations for the the quasi-one-dimensional geometry then reads

$$\frac{\sqrt{\text{var}I_{1,\Phi}(\phi)}}{I_{\Phi}(\phi)} = \left(\frac{G_Q}{G}\right) \left(\frac{E_t}{E_{\Phi}}\right)^{3/4} \left(\frac{E_t}{E_{\text{th}}^1}\right)^{1/4} \frac{\sqrt{4\pi^2\mathcal{F}_{1,\Phi}(\phi)}}{J_{\Phi}}, \quad (4.125)$$

with an additional suppression $(E_t/E_{\Phi})^{3/4}$ compared to the corresponding zero magnetic field expression. The right panels of Figs. 4.8, 4.9, and 4.10 compare the corresponding results for the quantum dot and quasi-one-dimensional geometries. Specifically, we observe in Figure 4.10 that in both geometries the relative size of current fluctuations monotonically increases as a function of E_t/E_{Φ} in a nearly power-law fashion.

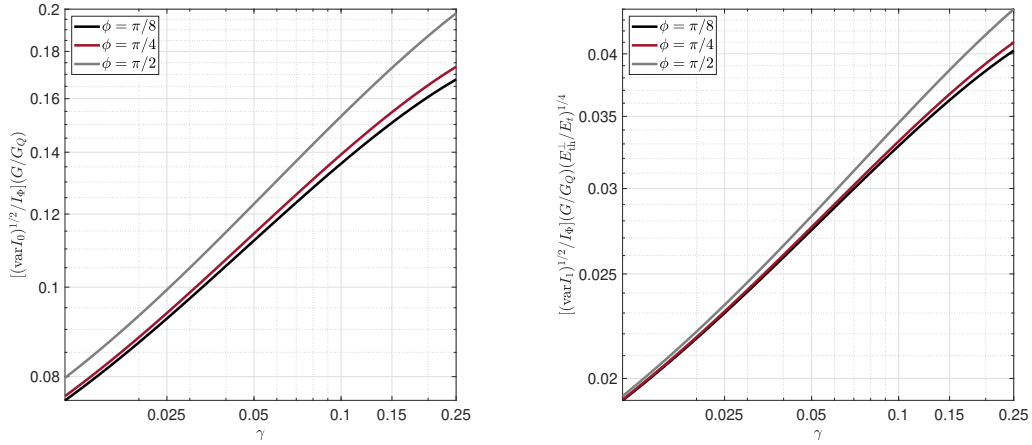


Figure 4.10: Relative size of current fluctuations $\sqrt{\text{var}I_{\Phi}}/I_{\Phi}$ in the strong magnetic field limit as a function of $\gamma = E_t/E_{\Phi}$ and various values of ϕ . Left panel: quantum dot geometry. Right panel: quasi-one-dimensional geometry.

Chapter 5

Summary

	$E_t \ll \Delta, E_\Phi = 0$	$E_t \gg \Delta, E_\Phi = 0$	$E_t \lesssim E_\Phi \ll \Delta$
$\frac{e}{G} I(\phi)$	$E_t \ln\left(\frac{\Delta}{E_t}\right) \sin \phi$	$\frac{1}{2} \Delta \mathbf{K}\left(\sin^2 \frac{\phi}{2}\right) \sin \phi$	$E_t \ln\left(\frac{\Delta}{E_\Phi}\right) \sin(\phi)$
$\frac{1}{e^2} \text{var} I_0(\phi)$	$E_t^2 \mathcal{K}_0(\phi)$	$\Delta^2 \mathcal{K}_0(\phi)$	$E_t^2 \frac{E_t^2}{E_\Phi^2} \mathcal{F}_{0,\Phi}(\phi)$
$\frac{1}{e^2} \text{var} I_1(\phi)$	$E_t^2 \sqrt{\frac{E_t}{E_{Th}^\perp}} \mathcal{K}_1(\phi)$	$\Delta^2 \sqrt{\frac{E_t}{E_{Th}^\perp}} \mathcal{K}_1^S(\phi)$	$E_t^2 \sqrt{\frac{E_t}{E_{Th}^\perp}} \sqrt{\frac{E_t^3}{E_\Phi^3}} \mathcal{F}_{1,\Phi}(\phi)$

Table 5.1: Table with results obtained previously for current and fluctuations for the two geometries considered and different dwell time and magnetic field regimes.

With the assistance of Table 5.1, we can observe that the average supercurrent exhibits a phase dependence that conforms to the Ambegaokar-Baratoff relation [90]. In the case of zero magnetic field and long dwell time ($E_t \ll \Delta$), the sinusoidal behavior is kept due to the logarithmic dependence, with energy scaling proportional to the dwell energy [82]. Conversely, for short dwell time ($E_t \gg \Delta$), there is only a slight deviation from the sinusoidal function, scaling with the superconducting gap [82, 81]. In the scenario of strong magnetic field, it behaves similarly to the long dwell time case but with the energy scale depending on E_Φ .

Following Table 5.1, it is possible to concisely summarize the energy dependence of both the supercurrent and fluctuations in each geometry domain. In the quantum-dot geometry at zero magnetic field, we define our current and fluctuations in two categories: long and short dwell times. These encompass the penetration and time scale of superconducting tunneling states along the non-superconducting region and can be probed for universality of fluctuations. For long dwell time, we observe a quadratic dependence on the dwell energy [84], in line with the average current. Meanwhile, for short time, the quadratic dependence is on the superconducting gap [43, 84, 85], also following the average supercur-

rent. In the presence of a strong magnetic field, the fluctuations still exhibit a quadratic dependence on the dwell energy but with a suppression factor due to the magnetic field. Moving to the quasi-one dimensional system and zero magnetic field, the results for long and short dwell times resemble those in the quantum-dot case, but now with an additional suppression factor arising from momenta integration, approximately of the order of a square root of the ratio E_t/E_{Th}^\perp . This results in smaller fluctuations when compared to the quantum-dot case. Upon the introduction of a strong magnetic field, the fluctuation is marginally smaller than the quantum-dot dependence on the magnetic field.

As a final remark the universality can be analysed by the ratio $varI/I^2$ for each of the cases (each column). We see that only for short dwell time in quantum-dot case we have solely the phase dependence. For the short dwell time there is a logarithmic suppression factor present. While for the quasi one-dimensional system there is always the ratio E_t/E_{Th}^\perp present. For the strong magnetic field cases there is a dependency of several (if not all), the energy scales present in our work. Next we should study if there is the necessity of introducing bulk states due to disorder presence. This necessity should be stated according to experimental appointment on the relevance of such states. For now we characterized the surface disordered states as expected according to energy regimes and external magnetic fields.

Chapter 6

Perspectives

Perspectives for the current approach - In recent research [89], significant progress has been made in comprehending the quantum fingerprint inherent in universal phenomena, notably conductance fluctuations (UCF). The study of universal conductance fluctuations offers insights into the microscopic properties of material composition, such as impurity configurations. Interpreting these fluctuations can prove challenging, as they seem to emerge as a stochastic function of variables.

An approach utilizing image recognition and classification through Neural Networks algorithms holds promise as an effective tool to shed light on the analysis of quantum fingerprints. This approach has the potential to provide valuable insights into the intricate patterns of conductance fluctuations, helping to extract meaningful information from what appears to be a random variation. A better understanding is possible with Figure 6.1.

The computation undertaken in this study, which encompasses the determination of both average supercurrent and the fluctuations in current across different samples, presents a significant challenge. It involves the application of advanced techniques within mean field theory and intricate calculations pertaining to matrix algebra. This very technique was previously established for Josephson junctions in normal metals, serving as a preliminary model for this method. The outcomes were derived from the findings presented in [43].

In experimental contexts, the observation of sample-to-sample fluctuations in supercurrents poses difficulties. Instead, it is more feasible to examine fluctuations within a specific sample while manipulating the chemical potential. Josephson junctions that incorporate surface states of a topological insulator (TI) in contact with superconducting elements

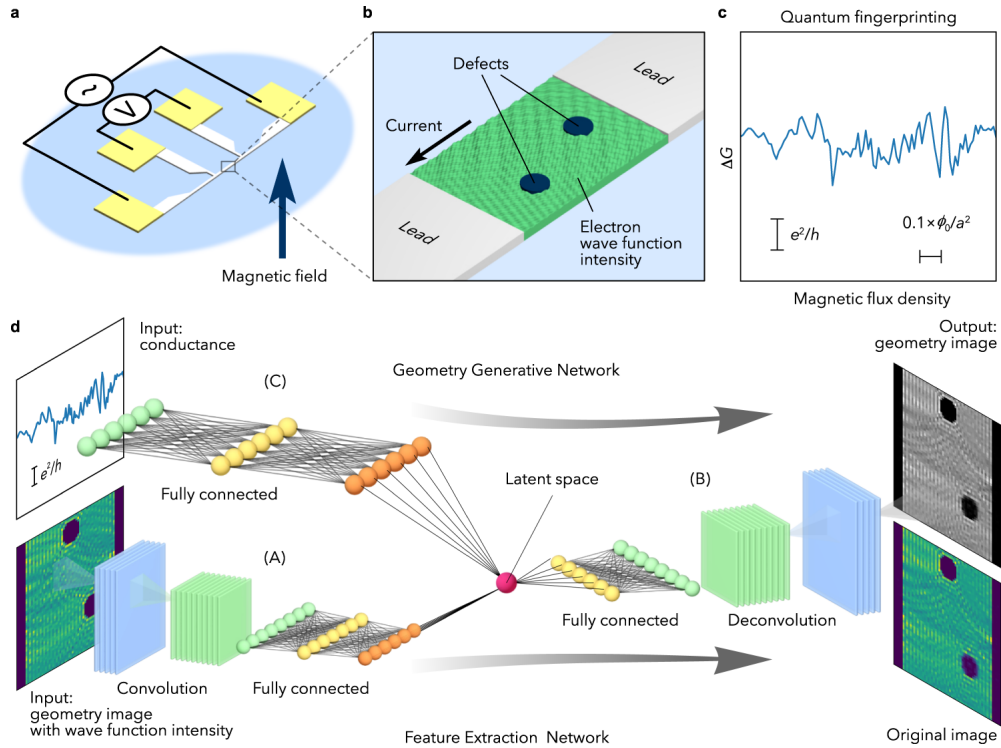


Figure 6.1: An image extracted from [89] illustrates the recognition process. The neural network is supplied with UCF data, generated using Kwant [13], for a metal connected to leads and exposed to an orthogonal magnetic field to the current propagation. Additionally, an image depicting the density of states of this metal, including randomly inserted defects in the lattice, is also provided as input. Utilizing a convolutional neural network, the study managed to reproduce defect information on density of states as output solely from UCF data. This advancement introduces the potential of a novel tool for exploring material structures, akin to how diffraction techniques have been employed over the past decades.

enable the manipulation of μ through gate voltage control. In such systems, one anticipates that when the chemical potential is adjusted over the scale of the Thouless energy, the critical current at low temperatures will universally fluctuate by a magnitude approximately equal to $e\Delta/h$. Remarkably, this fluctuation remains independent of the specific properties of the junction itself.

A python package for simulations - Kwant stands as a Python tool designed to compute tight-binding models for condensed matter systems, which are articulated as graphs within a lattice framework. This platform offers the capability to simulate transport phenomena utilizing any Hamiltonian that has been defined.

Kwant still encounters challenges when it comes to calculating Josephson currents. This is primarily due to difficulties in accurately computing Andreev bound states at the edges of junctions. In the near future, a proposed course of action involves the calculation of Josephson currents within a $2D$ STIS model. Then, examining the fluctuations across different samples and subsequently comparing these results with the analytical results from this work. Furthermore, it would be interesting to extend these findings to a bulk - surface model to facilitate a more realistic comparison to real systems, since the bulk can interfere with edge states, even though is insulating [57].

There is a experimental promise to create Majorana fermion at STIS. At present, the potential to create Majorana fermions in Kwant within this model remains uncertain. However, it is noteworthy that Kwant has already demonstrated its capability to replicate Majorana models, exemplified by the Kitaev Chain [17] and Haldane's model [50].

Neural networks approach - With these results, it will be possible to adapt the neural network proposed by Daimon et al. to assign microscopic meaning to universal super-current fluctuations and reproduce them. Another potential avenue is to transition from a neural network that relies on image recognition for a $2D$ density of states to one that utilizes the graph structure of Kwant itself.

Recently, a technique called Dynamic Graph Convolutional Neural Network (DGCNN) was developed [91], which could leverage the atom graph structure of a lattice in Kwant. This could be combined with the corresponding Hamiltonian values as input for the convolutional operation in DGCNN. This approach provides semantic values linked to the

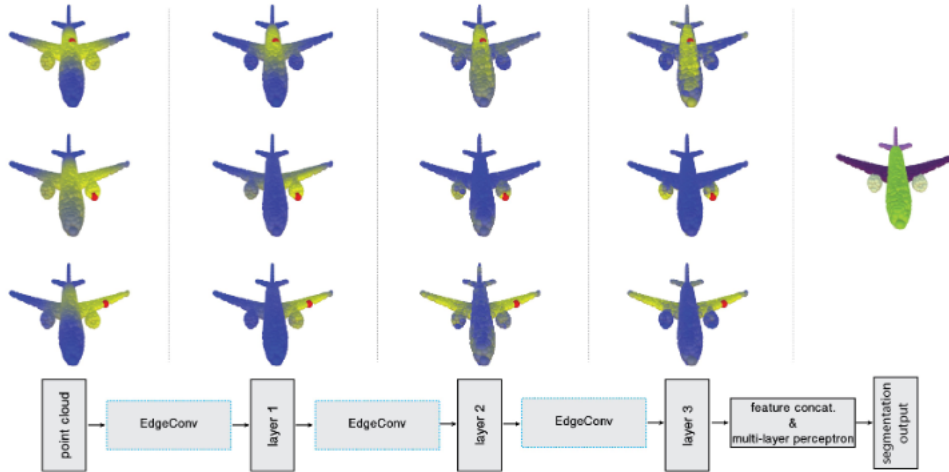


Figure 6.2: An image extracted from [91] serves as an example of how a DGCNN can gain comprehension using probes (in red) to discern the body, turbines, and wings of a airplane in a 3D point cloud context. The process involves assessing the distance between the red dots and all other points within the object. At each stage, the network associate distances semantically between the points, that is, the points belonging to the wing are nearer from each other than any point of the body, or the turbines. As a point in the left turbine is nearer to any point in the right turbine than any point the left wing, which it is attached. In a lattice there are several characteristics that could bring a semantic difference.

lattice points based on associated characteristics, such as kinetic and potential energies, hoppings, symmetries, atomic energy levels, etc. This collection of features can be trained to help the network comprehend the role and characteristics of each sector of the lattice, as illustrated in Figure 6.2.

In the realm of particle physics, an attempt has been made [92] to tag particle jets from calorimeters in particle detectors. This tagging approach could potentially serve as input alongside universal fluctuations, as demonstrated in [89], to improve lattice prediction for universal fluctuations.

Bibliography

- [1] N.G. Van Kampen, *Stochastic Processes in Physics and Chemistry*, North-Holland Publishing Company Amsterdam, New York, Oxford. (1981)
- [2] Kadanoff, L. P., et al., *Static Phenomena Near Critical Points: Theory and Experiment*, [Rev. Mod. Phys. 39, 395](#)
- [3] B. L. Altshuler, P. A. Lee and R. A. Webb, *Mesoscopic Phenomena in Solids*, [1st Edition - July 26, 1991](#)
- [4] C. P. Umbach, S. Washburn, R. B. Laibowitz, and R. A. Webb, *Magnetoresistance of small, quasi-one-dimensional, normal-metal rings and lines*, [Phys. Rev. B 30, 4048\(R\)](#)
- [5] B. L. Al'tshuler, *Fluctuations in the extrinsic conductivity of disordered conductors*, [JETP Lett. 41, 648 \(1985\)](#) [[Pis'ma Zh. Eksp. Teor. Fiz. 41, 530 \(1985\)](#)].
- [6] P. A. Lee and A. Douglas Stone, *Universal Conductance Fluctuations in Metals*, [Phys. Rev. Lett. 55, 1622 \(1985\)](#).
- [7] P. A. Lee, A. Douglas Stone, and H. Fukuyama, *Universal conductance fluctuations in metals: Effects of finite temperature, interactions, and magnetic field*, [Phys. Rev. B 35, 1039 \(1987\)](#).
- [8] C. W. J. Beenakker, *Random-matrix theory of quantum transport*, [Rev. Mod. Phys. 69, 731 \(1997\)](#).
- [9] B. L. Al'tshuler, *Fluctuations in the extrinsic conductivity of disordered conductors*, [Pis'ma Zh. Eksp. Teor. Fiz. 41, No. 12, 530533 \(25 June 1985\)](#)
- [10] M. L. Mehta, *Random Matrices*, ([Elsevier Ltd. 2004, 3rd edition](#)).

- [11] I. L. Aleiner, Ya. M. Blanter, *Inelastic Scattering Time for Conductance Fluctuations*, [Phys. Rev. B **65**, 115317 \(2002\)](#).
- [12] L.A.Bunimovich , *On the ergodic properties of nowhere dispersing billiards*, [Communications in Mathematical Physics volume 65, pages 295312 \(1979\)](#)
- [13] C. W. Groth, M. Wimmer, A. R. Akhmerov and X. Waintal, *Kwant: a software package for quantum transport*, [New Journal of Physics, Volume 16, June 2014](#)
- [14] Y. Aharonov and D. Bohm, *Significance of Electromagnetic Potentials in the Quantum Theory*, [Phys. Rev. **115**, 485 1 August 1959](#)
- [15] Y. Aharonov and D. Bohm, *Aharonov Bohm oscillation in a multi-domain ferromagnetic Fe19Ni81 ring*, [Physica E Vol. 18, Issues 13, May 2003, Pg 237-238](#)
- [16] R. Ramos, et al, *Aharonov Bohm oscillation in a multi-domain ferromagnetic Fe19Ni81 ring*, [Appl. Phys. Lett. **117**, 242402 \(2020\)](#)
- [17] A. Yu Kitaev, *6. QUANTUM COMPUTING Unpaired Majorana fermions in quantum wires*, [2001 Phys.-Usp. **44** 131](#)
- [18] C.W.J. Beenakker, *Search for Majorana Fermions in Superconductors*, [Annual Review of Condensed Matter Physics, Vol. 4:113-136 \(Volume publication date April 2013\)](#)
- [19] F. Tafuri, *Fundamentals and Frontiers of the Josephson Effect* , [Springer Series in Materials Science, ISBN978-3-030-20724-3](#)
- [20] Dmitry I. Pikulin et al, *Protocol to identify a topological superconducting phase in a three-terminal device*, [arXiv:2103.12217](#)
- [21] S. Daimon, et al, *Deciphering quantum fingerprints in electric conductance*, [Nat Commun **13**, 3160 \(2022\)](#)
- [22] J. Wilks, *The Properties of Liquid and Solid Helium*, [Oxford: Clarendon Press, ISBN 0-19-851245-7, 1967](#)
- [23] M. K. Wu, et al, *Superconductivity at 93 K in a new mixed-phase Y-Ba-Cu-O compound system at ambient pressure*, [Phys. Rev. Lett. **58**, 908 Published 2 March 1987](#)

- [24] W. Meissner, R. Ochsenfeld, *Ein neuer Effekt bei Eintritt der Supraleitfähigkeit* (A new effect when superconductivity occurs), [Naturwissenschaften](#) volume 21, pages 787788 (1933)
- [25] Yurong Lu, Ze Jing, Huadong Yong, Youhe Zhou *Flux avalanche in a superconducting film with non-uniform critical current density*, [Proc. R. Soc. A](#) 472: 20160469.
- [26] F. London, H. London, *The Electromagnetic Equations of the Supraconductor*, [Proceedings of the Royal Society A: Mathematical, Physical and Engineering Sciences](#). 149 (866): 71.
- [27] E. A. Lynton, *Superconductivity*, London, Methuen; New York, Wiley, 1962
- [28] V.L. Ginzburg, L.D. Landau, *On the theory of superconductivity*, [Zh. Eksp. Teor. Fiz.](#) 20, 1064 (1950)
- [29] A. Abrikosov, V. L. Ginzburg, A. J. Leggett, *The importance of order*, [Nobel Lecture](#), December 8, 2003
- [30] J. Bardeen, L. N. Cooper, and J. R. Schrieffer, *Theory of Superconductivity*, [Phys. Rev.](#) 108, 1175 1 December 1957
- [31] L. N. Cooper, *Bound Electron Pairs in a Degenerate Fermi Gas*, [Phys. Rev.](#) 104, 1189 15 November 1956
- [32] J. Bardeen, L. N. Cooper, and J. R. Schrieffer, *The Nobel Prize in Physics 1972* , Award ceremony speech. [NobelPrize.org](#). Nobel Prize Outreach AB 2023. Sun. 30 Apr 2023.
- [33] B. Simons, A. Altland, *Theories of Mesoscopic Physics*,
- [34] V. V. Schmidt, *The Physics of Superconductors*, [Springer Berlin, Heidelberg](#), ISBN978-3-540-61243-8, 1997
- [35] M. T. Levinsen, *Electromagnetic properties of the Dayem bridge*, [Revue de Physique Appliquée](#), 1974, 9 (1), pp.135-144
- [36] K.K. Likharev, *Superconducting weak links*, [Rev. Mod. Phys.](#) 51, 101 (1979)

- [37] B. D. Josephson, *Possible new effects in superconductive tunnelling*, Volume 1, Issue 7, 1 July 1962, Pages 251-253
- [38] I.K.Yanson, V.M. Svistunov, I.M. Dmitrenko, *Possible new effects in superconductive tunnelling*, *Zh. Eksp. Teor. Fiz.* 48, 976 (1965) [English transl.: *Sov. Phys. JETP* 21, 650 (1965)]
- [39] S. Shapiro, *Josephson Currents in Superconducting Tunneling: The Effect of Microwaves and Other Observations*, *Phys. Rev. Lett.* 11, 80 15 July 1963
- [40] R.P. Feynman, R.B. Leighton, M. Sands, *The Schrödinger Equation in a Classical Context: A Seminar on Superconductivity*, *The Feynman Lectures on Physics 3: Quantum Mechanics*
- [41] B. L. Al'tshuler, B. Z. Spivak *Mesoscopic fluctuations in a superconductor-normal metal-superconductor junction*, *Zh. Eksp. Teor. Fiz.* 92,609-615 (February 1987)
- [42] S. G. den Hartog, C. M. A. Kapteyn, B. J. van Wees, et al *Sample-Specific Conductance Fluctuations Modulated by the Superconducting Phase*, *Phys. Rev. Lett.* 76, 4592 Published 10 June 1996
- [43] T. Micklitz, *Interface dependence of the Josephson-current fluctuations in short mesoscopic superconductor/normal-conductor/superconductor junctions*, *Phys. Rev. B* 75, 144509
- [44] A. Altland, Ben D. Simons, *Condensed Matter Field Theory*, Cambridge University Press, 2010
- [45] J. Hubbard, *Calculation of Partition Functions*, *Phys. Rev. Letters.* 3 (2): 77
- [46] R.L. Stratonovich, / *On a Method of Calculating Quantum Distribution Functions*, *Soviet Physics Doklady*, Vol. 2, p.416
- [47] S. Chern, *Characteristic classes of Hermitian Manifolds*, *Annals of Mathematics Second Series*, Vol. 47, No. 1 (Jan., 1946), pp. 85-121 (37 pages)
- [48] R. B. Laughlin, *Quantized Hall conductivity in two-dimensions*, *Phys. Rev. B*, vol. 23, no. 10, p. 5632, 1981.

- [49] D. J. Thouless, M. Kohmoto, M. P. Nightingale, and M. Den Nijs, *Quantized Hall conductance in a two-dimensional periodic potential*, [Phys. Rev. Lett.](#), vol. 49, no. 6, p. 405, 1982.
- [50] F. D. M. Haldane, *Model for a quantum Hall effect without Landau levels condensed matter realization of the parity anomaly*, [Phys. rev. lett.](#), vol. 61, no. 18, p. 2015, 1988.
- [51] C. L. Kane, E. J. Mélé, *Z₂ topological order and the quantum spin Hall effect*, [Phys. Rev. Lett.](#), vol. 95, p. 146802, 2005.
- [52] B. A. Bernevig, T. L. Hughes, S.-C. Zhang, *Quantum Spin Hall Effect and Topological Phase Transition in HgTe Quantum Wells*, [Science](#), vol. 314, no. 5806, p. 1757, 2006.
- [53] R. Roy, *Z₂ classification of quantum spin Hall systems; an approach using time-reversal invariance*, [Phys.Rev.B](#), vol. 79, p. 195321, 2009.
- [54] J. E. Moore, L. Balents, *Topological invariants of time-reversal-invariant band structures*, [Phys.Rev.B](#), vol. 75, p. 121306(R), 2007.
- [55] L. Fu, C. L. Kane, E. J. Mélé, *Topological insulators in three dimensions*, [Phys. Rev. Lett.](#), vol. 98, p. 106803, 2007
- [56] H. Zhang, C. X. Liu, X. L. Qi, et al *Topological insulators in Bi₂Se₃, Bi₂Te₃ and Sb₂Te₃ with a single Dirac cone on the surface*, [Nature Phys](#) 5, 438442 (2009)
- [57] H. Velkov, G. N. Bremm, T. Micklitz, G. Schwiete, *Transport in topological insulators with bulk-surface coupling: Interference corrections and conductance fluctuations*, [Phys. Rev. B](#) 98, 165408
- [58] S. F. Edwards, P. W. Anderson , *Theory of spin glasses*, 1975 [J. Phys. F: Met. Phys.](#) 5 965
- [59] A. Altland, *Condensed Matter Field Theory*, [Cambridge University Press](#), August 2010
- [60] A. A. Abrikosov, L. P. Gor'kov [Zh. Eksp. Teor. Fiz.](#) 39, 1781 (1960) [[Sov. Phys. JETP](#) 12, 1243 (1961)]

- [61] Y. V. Nazarov, *Novel circuit theory of Andreev reflection* [Volume 25, Issues 56, May 1999, Pages 1221-1231](#)
- [62] J. Reutlinger, L. Glazman, Yu. V. Nazarov, and W. Belzig, “*Smile*” *Gap in the Density of States of a Cavity between Superconductors* [Phys. Rev. Lett. 112, 067001](#)
- [63] J. Reutlinger, L. Glazman, Yu. V. Nazarov, and W. Belzig, *Secondary “smile”-gap in the density of states of a diffusive Josephson junction for a wide range of contact types* [Phys. Rev. B 90, 014521](#)
- [64] Colin M. Whisler, Maxim G. Vavilov, A. Levchenko *Josephson currents in chaotic quantum dots* [Phys. Rev. B 97, 224515](#)
- [65] A. Levchenko, *Crossover in the local density of states of mesoscopic superconductor/normal-metal/superconductor junctions* [Phys. Rev. B 77, 180503\(R\)](#)
- [66] A. A. Mazanik, Ya. V. Fominov, *Peculiarities of the density of states in SN bilayers* [Annals of Physics Volume 449, February 2023, 169199](#)
- [67] K. M. Frahm, P. W. Brouwer, J. A. Melsen, and C. W. J. Beenakker, *Effect of the Coupling to a Superconductor on the Level Statistics of a Metal Grain in a Magnetic Field* [Phys. Rev. Lett. 76, 2981](#)
- [68] J. S. Meyer and B. D. Simons, *Gap fluctuations in inhomogeneous superconductors* [Phys. Rev. B 64, 134516](#)
- [69] A. Lamacraft and B. D. Simons, *Tail States in a Superconductor with Magnetic Impurities* [Phys. Rev. Lett. 85, 4783](#)
- [70] I. S. Beloborodov, B. N. Narozhny, and I. L. Aleiner, *Effect of Time Reversal Symmetry Breaking on the Density of States in Small Superconducting Grains* [Phys. Rev. Lett. 85, 816](#)
- [71] P. M. Ostrovsky, M. A. Skvortsov, and M. V. Feigel’man, *Density of States below the Thouless Gap in a Mesoscopic SNS Junction* [Phys. Rev. Lett. 87, 027002](#)
- [72] M. V. Feigel’man and M. A. Skvortsov, *Universal Broadening of the Bardeen-Cooper-Schrieffer Coherence Peak of Disordered Superconducting Films* [Phys. Rev. Lett. 109, 147002](#)

- [73] D. Bagrets, A. Altland, *Class D Spectral Peak in Majorana Quantum Wires* [Phys. Rev. Lett. 109, 227005](#)
- [74] P. A. Ioselevich, P. M. Ostrovsky, and M. V. Feigel'man, *Majorana state on the surface of a disordered three-dimensional topological insulator* [Phys. Rev. B 86, 035441](#)
- [75] Jin-Peng Xu, Canhua Liu, Mei-Xiao Wang, et al, *Artificial Topological Superconductor by the Proximity Effect* [Phys. Rev. Lett. 112, 217001](#)
- [76] Ian M. Dayton, Nicholas Sedlmayr, Victor Ramirez, et al, *Scanning tunneling microscopy of superconducting topological surface states in Bi_2Se_3* [Phys. Rev. B 93, 220506\(R\)](#)
- [77] Nicholas Sedlmayr, E. W. Goodwin, Michael Gottschalk, et al, *Dirac surface states in superconductors: a dual topological proximity effect* [arXiv:1805.12330](#)
- [78] Bryan Rachmilowitz, He Zhao, Hong Li, et al, *Proximity-induced superconductivity in a topological crystalline insulator* [Phys. Rev. B 100, 241402\(R\)](#)
- [79] Hao Yang, Yao-Yi Li, Teng-Teng Liu, et al *Multiple In-Gap States Induced by Topological Surface States in the Superconducting Topological Crystalline Insulator Heterostructure $\text{Sn}_{1-x}\text{Pb}_x\text{Te-Pb}$* [Phys. Rev. Lett. 125, 136802](#)
- [80] L. G. Aslamazov, A. I. Larkin, and Yu. N. Ovchinnikov *Josephson effect in superconductors separated by a normal metal*, [Zh. Eksp. Teor. Fiz. 55, 323-335 \(July, 1968\)](#)
- [81] M. Yu. Kuprianov and V. F. Lukichev, *Influence of boundary transparency on the critical current of "dirty" SS'S structures*, [Zh. Eksp. Teor. Fiz. 94,139-149 \(June 1988\)](#)
- [82] P.W. Brouwer, C.W.J. Beenakker, *Anomalous temperature dependence of the supercurrent through a chaotic Josephson junction*, [Chaos, Solitons and Fractals Volume 8, Issues 78, JulyAugust 1997, Pages 1249-1260](#)
- [83] M. Marinho, G. Vieira, T. Micklitz, G. Schwiete, A. Levchenko, *Mesoscopic fluctuations in superconductor-topological insulator Josephson junctions* , [Annals of Physics, Volume 447, Part 2, December 2022, 168978 Annals of Physics](#)
- [84] M. Houzet, M.A. Skvortsov, *Mesoscopic fluctuations of the supercurrent in diffusive Josephson junctions*, [Phys. Rev. B 77 \(2008\) 057002](#)

- [85] C.W.J. Beenakker, *Random-matrix theory of mesoscopic fluctuations in conductors and superconductors*, [Phys. Rev. B 47, 15763](#)
- [86] J. C. Hammer, J. C. Cuevas, F. S. Bergeret, W. Belzig *Density of states and supercurrent in diffusive SNS junctions: Roles of nonideal interfaces and spin-flip scattering*, [Phys. Rev. B 76, 064514](#) Published 14 August 2007
- [87] F. S. Bergeret, J. C. Cuevas, *The Vortex State and Josephson Critical Current of a Diffusive SNS Junction*, [Journal of Low Temperature Physics](#) volume 153, pages 304324 (2008)
- [88] A. Barone, G. Paterno, *Quantum Interference in Josephson Junctions*, [Physics and Applications of the Josephson Effect](#), Wiley, New York, 1982.
- [89] Shunsuke Daimon, Kakeru Tsunekawa, Shinji Kawakami, et al *Deciphering quantum fingerprints in electric conductance*, [Nature Communications 13, 3160](#) (2022).
- [90] Vinay Ambegaokar, Alexis Baratoff *Tunneling Between Superconductors*, [Phys. Rev. Lett. 10, 486](#) Published 1 June 1963; [Erratum Phys. Rev. Lett. 11, 104](#) (1963)
- [91] Yue Wang, Yongbin Sun, Ziwei Liu, et al *Dynamic Graph CNN for Learning on Point Clouds*, [ACM Transactions on Graphics](#) Volume 38 Issue 5 Article No.: 146 pp 112
- [92] Huilin Qu, Loukas Gouskos *Jet tagging via particle clouds*, [Phys. Rev. D 101, 056019](#)

Appendix A

Gradient Expansion

A.1 First order term

From the last expression, we can observe that there are two types of contributions: one of first order and another of second order in the propagated perturbation \mathcal{O}_T . Let's start by evaluating the first term, which is of the following form:

$$Tr(G_0 A) = \sum_{\mathbf{p}} Tr(G_0(\mathbf{p}) A) = -i\pi\nu_0 \int d\mathbf{x} \text{tr} \left(\sigma_3^{ph} A(x) \right), \quad (\text{A.1})$$

for a function A of the position inside the junction. We used the result of the saddle point equation (4.40) and (4.41) to solve G_0 . Then A is substituted as \mathcal{O}_T

$$A = T^{-1} \left[-i\hat{\epsilon}\sigma_3^{ph} - T[v\mathbf{k}\cdot\sigma^s, T^{-1}] + \hat{H}_\Gamma \sigma_3^{ph} \right] T. \quad (\text{A.2})$$

First, for the terms with σ_3^{ph}

$$Tr(G_0 A) = -i\pi\nu_0 \int d\mathbf{x} \text{tr} \left[Q \left(-i\hat{\epsilon} + \hat{H}_\Gamma \right) \sigma_3^{ph} \right] \quad (\text{A.3})$$

where we used that $Q = T\sigma_3^{ph}T^{-1}$ and trace properties. The commutator can be understood in a more complex way, using the fact that T is also an operator.

$$\begin{aligned} & -T^{-1}T[v\mathbf{k}\cdot\sigma^s, T^{-1}]T\psi = -v[\mathbf{k}\cdot\sigma^s, T^{-1}]T\psi \\ & = -iv \left[(\sigma\partial_X T^{-1})T\psi + (\sigma T^{-1}\partial_X T)\psi + \sigma\mathbf{k}\psi - T^{-1}(\sigma\partial_X T)\psi - T^{-1}\sigma T\mathbf{k}\psi \right] \\ & = ivT^{-1}(\sigma\partial_X T)\psi - v(\sigma - T^{-1}\sigma T)\mathbf{k}\psi. \end{aligned} \quad (\text{A.4})$$

We now consider the commutator (A.4) and focus on the case of a singlet, where the matrices T do not have internal structure in spin space. This implies that the second term, which corresponds to a mass-like term in the final propagator, is null, as the commutator $[v\mathbf{k}\cdot\sigma^s, T^{-1}]$ vanishes. Only spin singlet matrices correspond to soft modes, while spin triplet modes have masses on the order of $\sim \eta/\tau$, which is a much larger energy scale for our model. The final result is simple: we do not obtain contributions from the mass-like term, since it directly arises from the vanished factor in the commutator. Therefore, for the action S_1 , we have

$$S_1 = -\frac{i\pi\nu_0}{2} \int d\mathbf{x} \operatorname{tr} \left[Q \left(-i\hat{\epsilon} + \hat{H}_\Gamma \right) \sigma_3^{ph} \right]. \quad (\text{A.5})$$

and for S_2 , the second-order term simplifies because when $\mathbf{k} \neq 0$, the trace over the spin matrices contributes as zero.

A.2 Second order term

From a clever separation of (4.44) we shall use the Green's function ansatz.

$$G_0 = \frac{1}{2} \sum_{i=1}^2 \sum_{j=+,-} g_j^i (1 + jQ_0) \sigma_i^s, \quad (\text{A.6})$$

with

$$g_+^i = \frac{\mu + \frac{i}{2\tau} + vk_i}{\left(\mu + \frac{i}{2\tau}\right)^2 - v^2\mathbf{k}^2} = (g_-^i)^*, \quad (\text{A.7})$$

$$g_-^i = \frac{\mu - \frac{i}{2\tau} + vk_i}{\left(\mu - \frac{i}{2\tau}\right)^2 - v^2\mathbf{k}^2} = (g_+^i)^*. \quad (\text{A.8})$$

This can be understood as a separation of the saddle point equation from the result (4.41), which states ± 1 values for the saddle point. The condition $\frac{1}{2}(1 + Q_0)$ represents this separation, and the sign is determined by the previous definitions of g_j^i for the denominator, which also involves Q_0 . This can be interpreted as a separation of the Green's functions for the Advanced and Retarded modes of propagation, corresponding to particles and holes. In (4.44), we can see that the imaginary factor acts as a self-energy for this propagator,

with an energy scale of $\frac{1}{2\tau}$.

$$\begin{aligned}
S_2 &= \frac{1}{4} \text{Tr}(G_0 \mathcal{O}_T G_0 \mathcal{O}_T) \\
&= -\frac{v^2}{16} \sum_{i,k=1}^2 \sum_{j,l=1}^2 \text{Tr} \left(g_0^i \sigma_i^s A_j \sigma_j^s g_0^k \sigma_k^s A_l \sigma_l^s \right) \\
&= -\frac{v^2}{16} \sum_{i,k=1}^2 \sum_{j,l=1}^2 \text{tr} \left(\sigma_i^s \sigma_j^s \sigma_k^s \sigma_l^s \right) \text{Tr} \left(g_0^i A_j g_0^k A_l \right) \\
&= -\frac{v^2}{16} \sum_{i,k=1}^2 \sum_{j,l=1}^2 \text{tr} \left(\sigma_i^s \sigma_j^s \sigma_k^s \sigma_l^s \right) \text{Tr} \left((g_+^i + g_-^i) A_j (g_+^k + g_-^k) A_l \right) \\
&= -\frac{v^2}{16} \int d\mathbf{k} \text{Tr} \left((g_+^i + g_-^i) A_i \right)^2 \\
&= -\frac{v^2}{16} \int d\mathbf{k} \text{Tr} \left([g_+^i A_i]^2 + [g_-^i A_i]^2 + 2g_+^i A_i g_-^i A_i \right) \\
&= -\frac{\mu\nu\tau}{8} \int d\mathbf{x} \text{tr} \left(A_i^2 - Q_0 A_i Q_0 A_i \right) \\
&= -\frac{\mu\nu D}{8} \int d\mathbf{x} \text{tr} \left(\partial Q_0 \partial Q_0 \right), \quad Q = T Q_0 T^{-1}, \quad D = \tau_{\text{tr}} v^2 / 2
\end{aligned} \tag{A.9}$$

The factor of $\frac{1}{16}$ in the first term is justified by the action and the factors of $\frac{1}{2}$ arise from the definition of G_0 . The factor of v^2 comes from \mathcal{O}_T as well as the presence of the spin Pauli matrices σ^s . The indices j and l correspond to the spatial derivative indices x and y , while i and k are indices associated with the g^i Green's functions. The notation $A_i = T \partial_i T^{-1}$ is introduced to simplify the expression. The last simplification step involved using $\partial_i Q = (\partial_i T) Q_0 T^{-1} + T Q_0 (\partial_i T^{-1})$ and performing trace permutations. For the integrals in the square brackets and the third term, respectively, the following relations were used:

$$\int d\xi \frac{\xi}{(\xi \pm ia)^2} = 0, \quad \int d\xi \frac{\xi}{\xi^2 \pm i/a^2} = \pi a. \tag{A.10}$$

To introduce an external magnetic field into the model, we can achieve gauge invariance by considering a gauge transformation. By examining equation (4.6), we see that the transformation $\chi \mapsto e^{i\phi} \chi$ induces a corresponding transformation for the enlarged field Ψ , given by $\Psi \mapsto e^{i\Phi} \Psi$, where $\Phi(\mathbf{k})$ is a diagonal matrix defined as $\Phi(\mathbf{k}) = \text{diag}(\phi(\mathbf{k}), \phi(\mathbf{k}), -\phi(-\mathbf{k}), -\phi(-\mathbf{k}))$. Since Q has a dyadic form $Q \approx \Psi \bar{\Psi}$, it should transform as $Q \mapsto e^{i\Phi} Q e^{i\Phi}$.

In order to understand the effect of this transformation on the action, we need to incorporate it and examine its consequences. Since we have the transformation for Q , which is written as $Q = TQ_0T^{-1}$ before the expansion in T , it is interesting to consider this factorization of Q in the action and analyze the implications. This will allow us to investigate how this transformation aids in introducing the external magnetic field into the system. Considering the second order term, upon performing the gauge transformation, we would get that

$$\partial_i(e^{i\Phi}Qe^{i\Phi})\partial_i(e^{i\Phi}Qe^{i\Phi}) = (\partial_iQ + i[\partial_i\Phi, Q]) \quad (\text{A.11})$$

This additional term breaks the gauge invariance. In order to correct it we can add a vector potential as $\partial_i \mapsto \partial_i - i[\mathbf{A}, \dots]$, knowing that $\mathbf{A} \mapsto \mathbf{A} + \partial_i\Phi$. The first order derivative vanishes due to the fact that needs a structure in spin space. Since for ϵ the transformation gets a $\partial_tQ - [\partial_t\Phi, Q]$ when transforming ϵ to $i\partial_t$ shall transform, in the action $\epsilon \mapsto \epsilon + i[V, \dots]$, knowing that $V \mapsto V + \partial_t\Phi$. Now our new action is

$$S = \frac{\pi\nu}{2} \int d\mathbf{x} \text{Tr} \left(\frac{D}{4}(\partial_{\mathbf{x}} - i[\mathbf{A}, \cdot])Q(\partial_{\mathbf{x}} - i[\mathbf{A}, \cdot])Q - \hat{\epsilon}Q\sigma_3^{ph} - i\hat{H}_\Gamma\sigma_3^{ph}Q \right). \quad (\text{A.12})$$

Appendix B

Quantum Hall Effect Code

This code is an adaptation from the Notebook "kwant-tutorial-2016/3.2.Quantum-Hall-effect-and-disorder.ipynb" available on Git Hub

```
import kwant
from kwant.digest import uniform
import numpy as np
from cmath import exp
from types import SimpleNamespace
from ipywidgets import interact



---



lat = kwant.lattice.square(a=1, norbs=1)

t = 1
W = 30
L = 50

def onsite(site, params):
    return params.U0 * (uniform(repr(site), repr(params.salt)) - 0.5) + 4

def hopping(site_i, site_j, params):
    xi, yi = site_i.pos
```

```

    xj, yj = site_j.pos
    return -exp(-0.5j * params.phi * (xi - xj) * (yi + yj))

sys = kwant.Builder()
sys[(lat(x, y) for x in range(L) for y in range(W))] = onsite
sys[lat.neighbors()] = hopping

lead = kwant.Builder(kwant.TranslationalSymmetry([-1, 0]))
lead[(lat(0, y) for y in range(W))] = 4 * t
# no disorder in lead!
lead[lat.neighbors()] = hopping

sys.attach_lead(lead)
sys.attach_lead(lead.reversed())

sys = sys.finalized()

_____

kwant.plot(sys);

_____

U0 = 0.3
salt = 13
energy = 0.2

def plot_wf(phi=0):
    params = SimpleNamespace(phi=phi, U0=U0, salt=salt)
    wfs = kwant.wave_function(sys, energy=energy, args=[params])
    scattering_wf = wfs(0)
    # all scattering wave functions from lead 0
    kwant.plotter.map(sys, np.sum(abs(scattering_wf)**2, axis=0));

```

```

J_0 = kwant.operator.Current(sys)
kwant.plotter.current(sys, J_0(scattering_wf[0], args=[params]));

interact(plot_wf, phi=(0, 0.15, 0.002))

_____

energy = 0.2
U0 = 0.3
salt = 5

phis = np.linspace(0, 0.1, 51)

Gs = []
for phi in phis:
    params = SimpleNamespace(phi=phi, U0=U0, salt=salt)
    smat = kwant.smatrix(sys, energy=energy, args=[params])
    Gs.append(1/smat.transmission(1, 0))

plt.plot(phis, Gs);
plt.ylabel("R [R_0]")
plt.xlabel("phi")

```